

Electronic Supplementary Information

for

Bridging the interfacial gap in mixed-matrix membranes by nature-inspired design: Precise molecular sieving with polymer-grafted metal-organic frameworks

Levente Cseri,^a Rifan Hardian,^b Shizuka Anan,^c Hakkim Vovusha,^d Udo Schwingenschlögl,^d Peter M. Budd,^e Kazuki Sada,^{c,f} Kenta Kokado,^{g,h} Gyorgy Szekely^{a,b*}

^aDepartment of Chemical Engineering and Analytical Science, University of Manchester, The Mill, Sackville Street, Manchester, M1 3BB, United Kingdom

^bAdvanced Membranes & Porous Materials Center, Physical Science Engineering Division (PSE), King Abdullah University of Science and Technology (KAUST), Thuwal 23955-6900, Saudi Arabia, E-mail: gyorgy.szekely@kaust.edu.sa, Phone: +966128082769

^cDepartment of Chemical Sciences and Engineering, Graduate School of Chemical Sciences and Engineering, Hokkaido University, Kita 10, Nishi 8, Kita-ku, Sapporo, 060-0810, Japan

^dPhysical Science and Engineering Division (PSE), King Abdullah University of Science and Technology (KAUST), Thuwal, 23955-6900, Saudi Arabia

^eDepartment of Chemistry, University of Manchester, Oxford Road, Manchester, M13 9PL, United Kingdom

^fFaculty of Science, Hokkaido University, Kita 10, Nishi 8, Kita-ku, Sapporo, 060-0810, Japan

^gResearch Institute for Electronic Science, Hokkaido University, Kita 20, Nishi 10, Kita-ku, Sapporo, 001-0020, Japan

^hJST, PRESTO, Honcho 4-1-8, Kawaguchi, Saitama 332-0012, Japan.

Table of contents

| | |
|--|-----|
| 1. Graphical hypothesis and summary | S3 |
| 2. Materials..... | S5 |
| 3. Syntheses..... | S6 |
| 2-Amino-[1,1'-biphenyl]-4,4'-dicarboxylic acid (bpdc-NH ₂) | S6 |
| 2'-Amino-[1,1':4',1''-terphenyl]-4,4''-dicarboxylic acid (tpdc-NH ₂)..... | S6 |
| <i>N</i> -Hydroxysuccinimide ester terminated poly(<i>N</i> -isopropylacrylamide) (PNIPAM-NHS)..... | S6 |
| UiO-66-NH ₂ and UiO-67-NH ₂ | S7 |
| UiO-68-NH ₂ | S7 |
| UiO-66-PNIPAM, UiO-67-PNIPAM, and UiO-68-PNIPAM | S7 |
| 4. NMR spectroscopy | S8 |
| 5. Mass spectrometry..... | S19 |
| 6. Fourier-transform infrared spectroscopy..... | S21 |
| 7. Size exclusion chromatography..... | S25 |
| 8. Elemental analysis | S26 |
| 9. Dynamic light scattering for particle size analysis..... | S27 |
| 10. MOF-PNIPAM coverage calculations..... | S28 |
| 11. X-ray powder diffraction | S30 |
| 12. Nitrogen adsorption measurements | S31 |
| 13. Scanning electron microscopy..... | S32 |
| 14. Thermal analysis..... | S42 |
| 15. Polymer solubility | S45 |
| 16. Membrane fabrication | S46 |
| 17. Atomic force microscopy..... | S47 |
| 18. Water contact angle measurements..... | S48 |
| 19. Computational methods..... | S49 |
| 20. Theoretical model of nanofiltration | S55 |
| 21. Estimating pore size for the nanofiltration model | S63 |
| 22. Organic solvent nanofiltration experiments and results..... | S65 |
| 23. Literature overview | S78 |
| 24. References..... | S81 |

1. Graphical hypothesis and summary

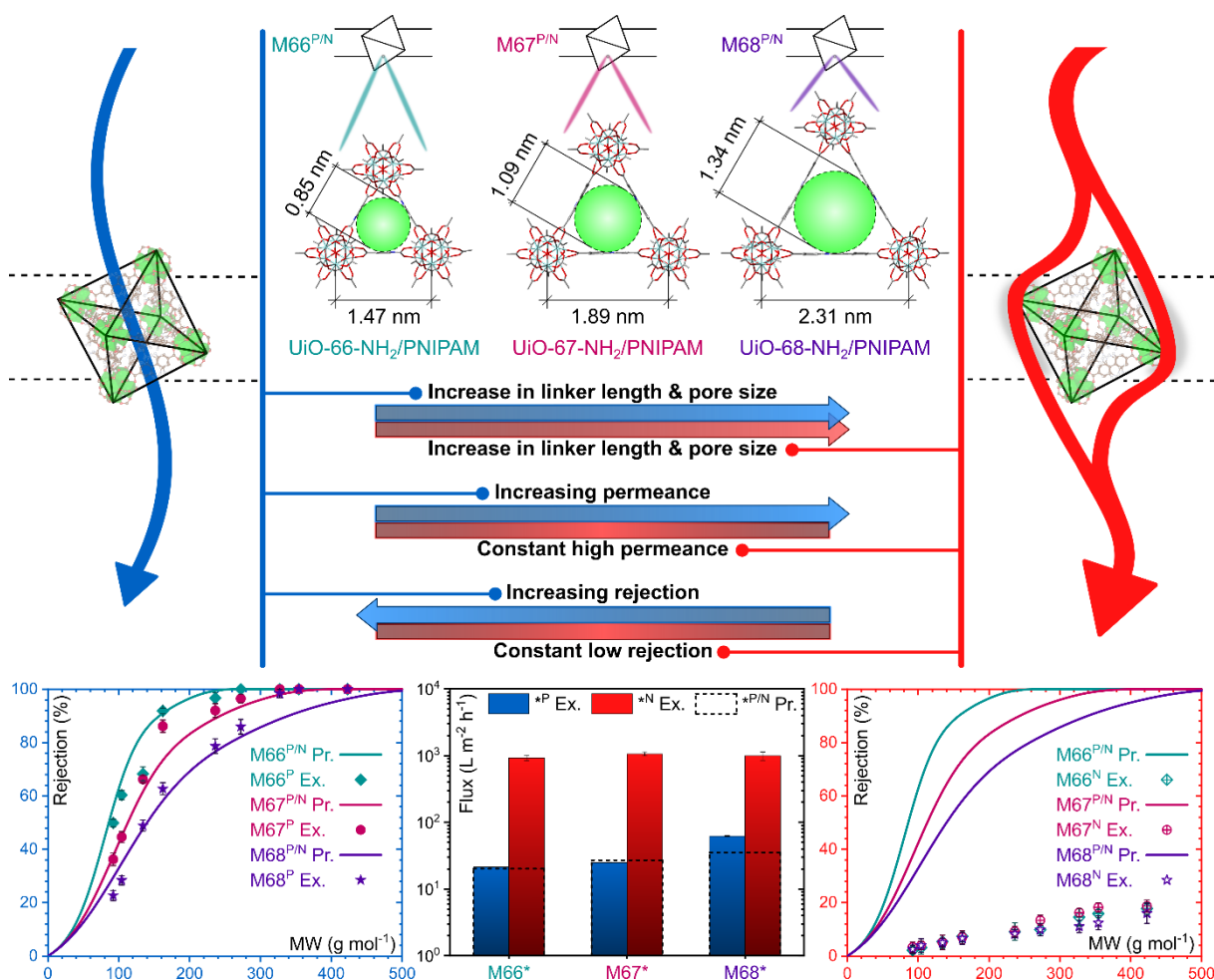


Fig. S1. Graphical hypothesis and summary of this study. A series of mixed-matrix membranes (MMMs) were fabricated using an identical procedure with fillers of similar particle size and chemical composition. However, the metal–organic framework (MOF) fillers differed in pore size owing to the different linker lengths. Because the only substantial difference between the membranes was the filler internal pore size, different trends in organic solvent nanofiltration (OSN) performance among them were expected if permeation occurred through the internal pores (blue) or around the filler particles (red). When MOF particles were grafted with a PNIPAM polymer, the OSN performance matched the predictions (Pr.) of the pore flow model. In contrast, without PNIPAM grafting, interfacial gaps were present between MOFs and the polymer matrix and the OSN performance was in line with the assumption of the permeation around the filler. (Filtration experiments were performed in crossflow mode at 30 bar and 20°C.)

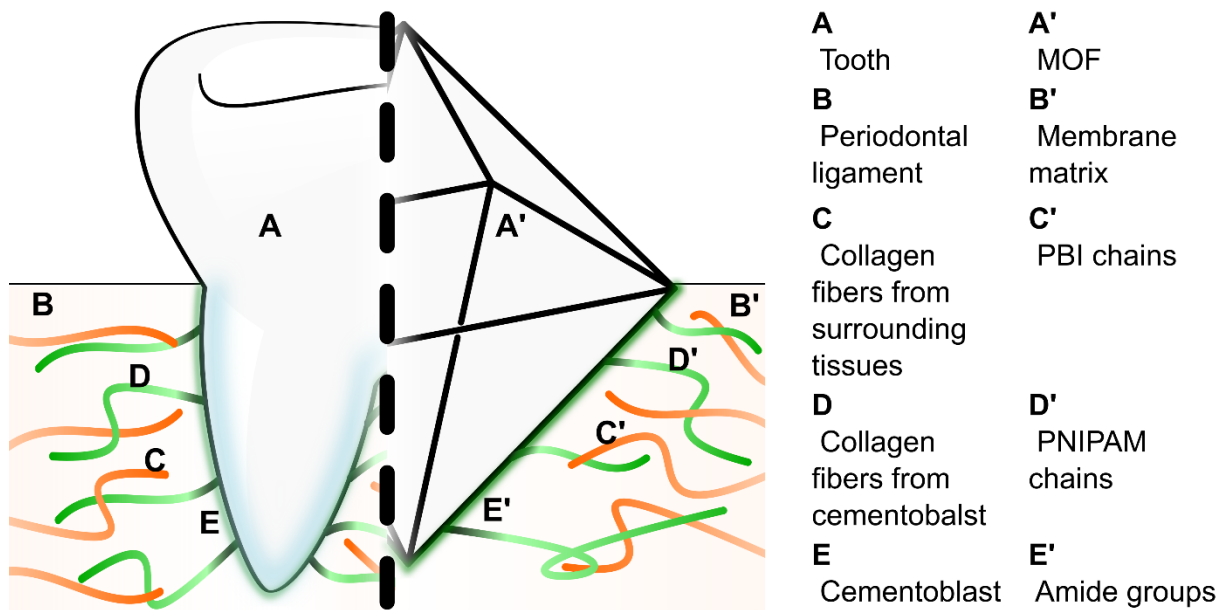


Fig. S2. Illustration of the nature-inspired design of the composite membranes. The calcified cementum in the tooth (A) is connected to the surrounding tissues by collagen fibers (D) originating from the cementoblast layer (E) on its surface. These fibers are intermingled in the periodontal ligament (B) with other the collagen fibers (C) stemming from to the surrounding tissues to ensure excellent adhesion between the different materials. Analogously, the external surface of metal–organic framework (MOF) nanoparticles (A') was grafted with poly(*N*-isopropylacrylamide) (PNIPAM) chains (D') through covalent amide bonds (E') to exploit their entanglement with the polybenzimidazole (PBI) chains (C') of the membrane matrix (B') for better interfacial adhesion. (The figure is not drawn to scale.)

2. Materials

2,5-Dibromoaniline (95%), 4-(4,4,5,5-tetramethyl-1,3,2-dioxaborolan-2-yl)benzoic acid (97%), and palladium (0) tetrakis(triphenylphosphine) [$\text{Pd}(\text{PPh}_3)_4$, 98%] were purchased from Fluorochem.

2,2'-Azobisisobutyronitrile (Wako Special Grade, >98.0%), abs. 1,4-dioxane (Wako for Organic Synthesis, >99.5%), benzoic acid (Wako 1st Grade, >99.5%), and ZrCl_4 (>95.0%) were purchased from Fujifilm Wako Pure Chemical Co.

N-Isopropylacrylamide (Wako Special Grade, >98.0%) was purchased from Fujifilm Wako Pure Chemical Co. and recrystallized from hexane ($1 \text{ g}\cdot\text{mL}^{-1}$) before use.

4-Cyano-4-(phenylcarbonothioylthio)pentanoic acid *N*-succinimidyl ester was purchased from Sigma Aldrich. 2-Aminoterephthalic acid (tpa- NH_2) was purchased from Tokyo Chemical Industry Co., Ltd.

Poly[2,20-(*m*-phenylene)-5,50-bisbenzimidazole] (PBI) S26 solution (26 wt% in DMAc) was purchased from PBI Performance Products (Charlotte, NC, USA).

Type II deionized (DI) water was used in all synthetic steps.

3. Syntheses

2-Amino-[1,1'-biphenyl]-4,4'-dicarboxylic acid (bpdc-NH₂)

The organic linker, 2-amino-[1,1'-biphenyl]-4,4'-dicarboxylic acid (bpdc-NH₂), was obtained in a single synthetic step. 3-Amino-4-bromobenzoic acid (8.64 g, 40 mmol), 4-(4,4,5,5-Tetramethyl-1,3,2-dioxaborolan-2-yl)benzoic acid (9.92 g, 40 mmol), Pd(PPh₃)₄ (2.31 g, 2 mmol), and K₂CO₃ (25.5 g, 120 mmol) were dissolved in a mixture of 1,4-dioxane (160 mL) and water (40 mL) in a round-bottom flask under argon atmosphere. The reaction was refluxed at 100°C for 12 h at which point HPLC analysis showed the total consumption of the starting materials. The reaction mixture was extracted using 300 mL of EtOAc and 200 mL of DI water. The organic phase was further extracted using 200 mL of a 0.1-M NaOH solution. The combined aqueous phases were washed with 300 mL of EtOAc. The aqueous phase was transferred to a conical flask. The pH was set to 3–4 via the slow addition of 1-M HCl (260 mL) under continuous stirring. The precipitation was filtered, washed with copious amounts of DI water, and dried under vacuum, yielding a beige solid product (9.21 g, 90%), which was used for the synthesis of UiO-67-NH₂ without further purification. ¹H NMR (400 MHz, DMSO-d₆) δ 12.54 (s, 2H), 8.02 (d, *J* = 8.1 Hz, 2H), 7.58 (d, *J* = 8.0 Hz, 2H), 7.42 (d, *J* = 1.8 Hz, 1H), 7.21 (dd, *J* = 7.9, 1.7 Hz, 1H), 7.11 (d, *J* = 7.9 Hz, 1H), 5.18 (s, 2H); ¹³C NMR (101 MHz, DMSO-d₆) δ 168.0, 167.6, 145.8, 143.8, 131.4, 130.7, 130.3, 129.9, 129.2, 128.9, 117.9, 116.7; HR-MS:(ESI⁻) calculated for C₁₄H₁₀NO₄ 256.0615 [M-H]⁻, found 256.0610, Df. = -2.07 ppm.

2'-Amino-[1,1':4',1''-terphenyl]-4,4''-dicarboxylic acid (tpdc-NH₂)

The organic linker, 2'-amino-[1,1':4',1''-terphenyl]-4,4''-dicarboxylic acid (tpdc-NH₂), was obtained in a single synthetic step. 2,5-Dibromoaniline (10.0 g, 40 mmol), 4-(4,4,5,5-Tetramethyl-1,3,2-dioxaborolan-2-yl)benzoic acid (27.3 g, 110 mmol), Pd(PPh₃)₄ (4.62 g, 4 mmol), and K₂CO₃ (50.9 g, 240 mmol) were dissolved in a mixture of 1,4-dioxane (240 mL) and water (60 mL) in a round-bottom flask under argon atmosphere. The reaction was refluxed at 100°C for 48 h at which point HPLC analysis showed the total consumption of the starting materials. The reaction mixture was extracted using 300 mL of EtOAc and 300 mL of DI water. The organic phase was extracted using 300 mL of a 0.1-M NaOH solution. The combined aqueous phases were washed with 300 mL of EtOAc. The aqueous phase was transferred to a conical flask. The pH was set to 3–4 via the dropwise addition of cc HCl (45 mL) under continuous stirring. The beige precipitation was filtered, washed with copious amounts of DI water, and dried under vacuum. The crude product was recrystallized from 150 mL of DMF, which yielded the product as gray solid (8.48 g, 64%). ¹H NMR (400 MHz, DMSO-d₆) δ 12.88 (s, 2H), 8.03 (d, *J* = 8.4 Hz, 4H), 7.74 (d, *J* = 8.4 Hz, 2H), 7.61 (d, *J* = 8.3 Hz, 2H), 7.16 (s, 1H), 7.15 (d, *J* = 5.9 Hz, 1H), 7.00 (dd, *J* = 7.9, 1.8 Hz, 1H), 5.13 (s, 2H). ¹³C NMR (101 MHz, DMSO-d₆) δ 167.2, 167.2, 145.8, 144.6, 143.8, 139.5, 130.9, 130.0, 129.9, 129.6, 129.1, 128.8, 126.5, 124.6, 115.5, 113.8; HR-MS:(ESI⁻) calculated for C₂₀H₁₄NO₄ 332.0928 [M-H]⁻, found 332.0922, Df. = -1.90 ppm.

***N*-Hydroxysuccinimide ester terminated poly(*N*-isopropylacrylamide) (PNIPAM-NHS)**

The polymer, poly(*N*-isopropylacrylamide), containing an activated carboxyl end group (PNIPAM-NHS), was synthesized via reversible addition–fragmentation chain-transfer (RAFT) polymerization. *N*-Isopropylacrylamide (1.00 g, 8.84 mmol), 2,2'-azobisisobutyronitrile (AIBN, 2.90 mg, 17.7 μmol, 0.2 mol%), and 4-cyano-4-(phenylcarbonothioylthio)pentanoic acid *N*-succinimidyl ester (RAFT-NHS, 33.3 mg, 88.4 μmol, 1 mol%) were dissolved in abs. 1,4-dioxane (4.14 mL). The solution was transferred into an ampule and degassed by three freezing–evacuating–thawing cycles. The ampule was closed, and the polymerization was initiated at 70°C for 40 h. The post-polymerization mixture was allowed

to cool to room temperature, and the polymer was precipitated by pouring it into 120 mL of diethyl ether under continuous stirring. The precipitate was filtered, washed with 60 mL of ether, and dried under vacuum to yield PNIPAM-NHS as a pale pink powder (693 mg, 69%).

UiO-66-NH₂ and UiO-67-NH₂

In a screw-capped vial, 61 μmol of the organic linker (11 mg of 2-aminoterephthalic acid for UiO-66-NH₂ or 16 mg of bpdc-NH₂ for UiO-66-NH₂), ZrCl₄ (12 mg, 52 μmol), and benzoic acid (190 mg, 1.6 mmol) were dissolved in DMF (1 mL) and filtered through a membrane syringe filter (0.45- μm pore size). The mixture was kept still at 120°C for 24 h. After cooling to room temperature, the crystals were collected by centrifuging (2000 rpm, 3 \times 3 min), with consecutive washes with DMF and methanol.

UiO-68-NH₂

Owing to the limited solubility of tpdc-NH₂, UiO-68-NH₂ was prepared via a slightly different method compared to that used for other MOFs. In a 500-mL, round-bottom flask, tpdc-NH₂ (1.33 g, 4 mmol) and ZrCl₄ (0.93 g, 4 mmol) were dissolved in DMF (320 mL) at 90°C for 5 min and filtered through a membrane filter (0.45- μm pore size). Acetic acid (12 mL) and distilled water (4 mL) were added, and the mixture was kept still at 90°C for 24 h. After cooling to room temperature, the crystals were collected by centrifuging (5000 rpm, 3 \times 3 min), with consecutive washes with DMF and methanol.

UiO-66-PNIPAM, UiO-67-PNIPAM, and UiO-68-PNIPAM

In a 5-mL screw vial, MOF (60 mg) and a 0.1-M PNIPAM-NHS solution (500 μL) in chloroform were mixed; the mixture was kept still at 60°C for 24 h. After cooling to room temperature, the crystals were collected via filtration and repeatedly washed with chloroform and methanol.

Size exclusion chromatography (SEC) was performed on a SHIMADZU LC-20AD system (SHODEX K-805L and K-803L) using a SHIMADZU SPD-20A UV detector (calibrated using standard polystyrene samples) using chloroform as an eluent at 40°C. X-ray powder diffraction (XPRD) patterns were obtained using a Bruker D8Advance instrument with a Cu K α radiation source (40 kV, 40 mA). Nitrogen adsorption measurement was conducted using a Yuasa Ionics Autosorb 6AG at -196°C. Prior to the measurement, the MOF particles were thoroughly activated at 100°C under high vacuum for 12 h. Pore size distribution (PSD) was calculated from the fitted N₂ adsorption isotherms to DFT using slit-cylindrical pores and QSDFT equilibrium model.

4. NMR spectroscopy

NMR spectra of bdpc-NH₂, tdpc-NH₂, and PNIPAM-NHS were recorded using a Bruker Avance III 400 MHz instrument using 128 and 1024 scans for ¹H and ¹³C spectra, respectively. The spectra were processed using the MestRe Nova software. Assignments were performed using 2D experimental data (COSY, ¹H-¹³C HSQC, ¹H-¹³C HMBC, and ¹H-¹⁵N HMBC) and the NMR prediction tool of MestRe Nova. The ¹H and ¹³C NMR spectra of the MOF samples were recorded using a Bruker Avance III 500 MHz using 128 and 1024 scans, respectively. The samples were prepared by digesting 5 mg of MOF in a mixture of 30 μL of HF and 0.6 mL of deuterated dimethylsulfoxide (DMSO-*d*₆) followed by ultrasonication for 10 min. For simplicity, the HF signal was removed from the ¹H spectra using the signal suppression function of MestRe Nova.

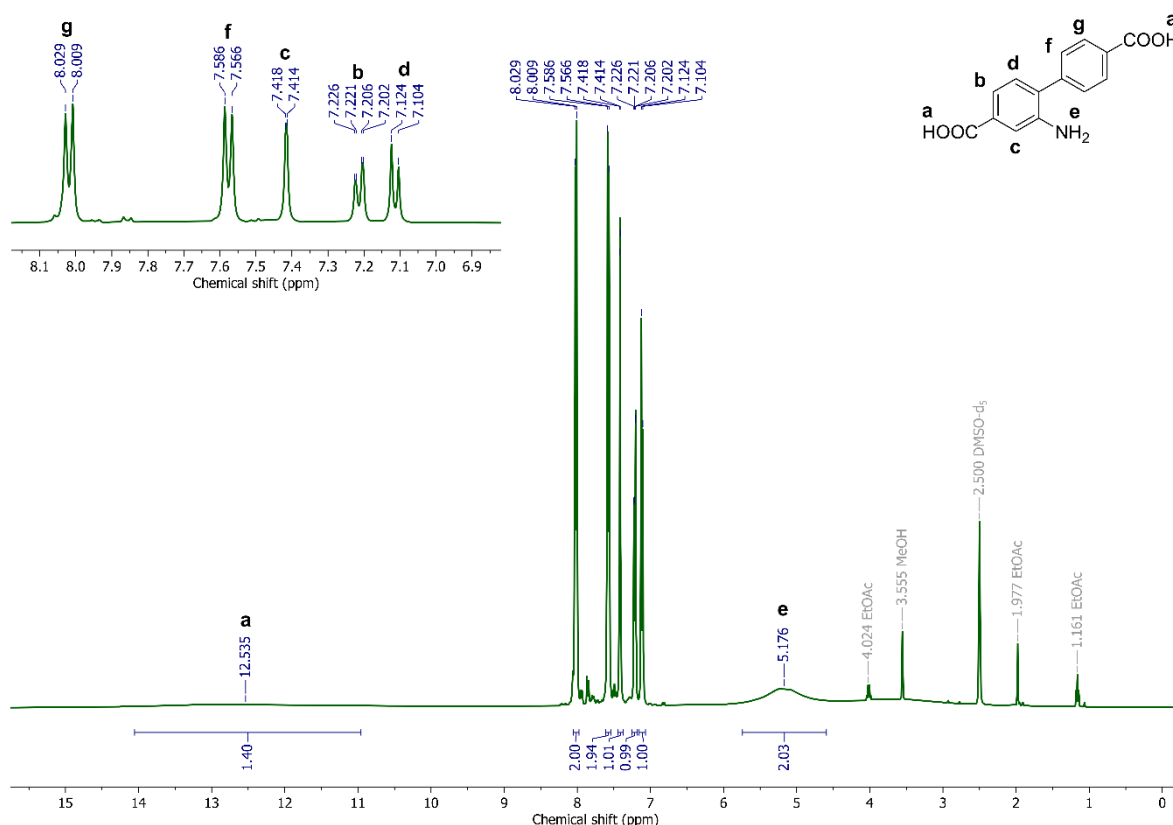


Fig. S3. ¹H NMR spectrum of bdpc-NH₂ recorded in DMSO-*d*₆ at 400 MHz with the structure shown in the inset.

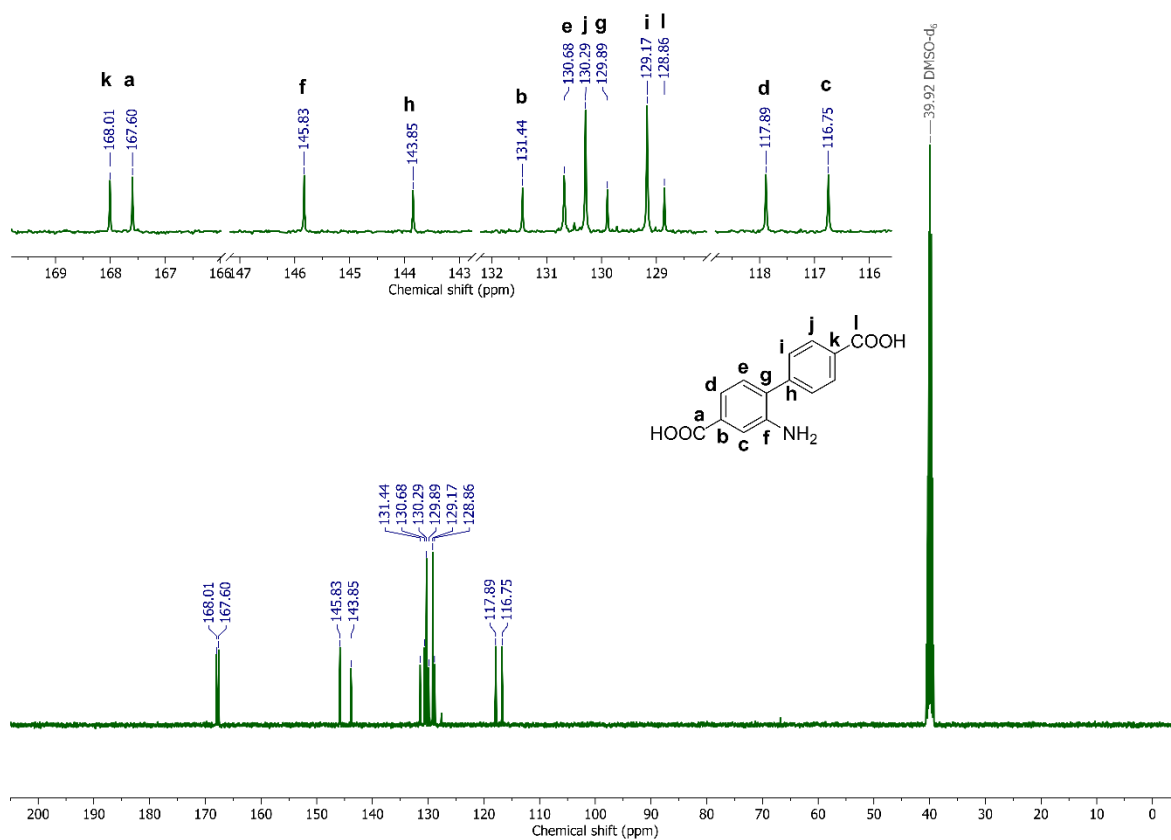


Fig. S4. ¹³C NMR spectrum of bpdC-NH₂ recorded in DMSO-d₆ at 101 MHz with the structure shown in the inset.

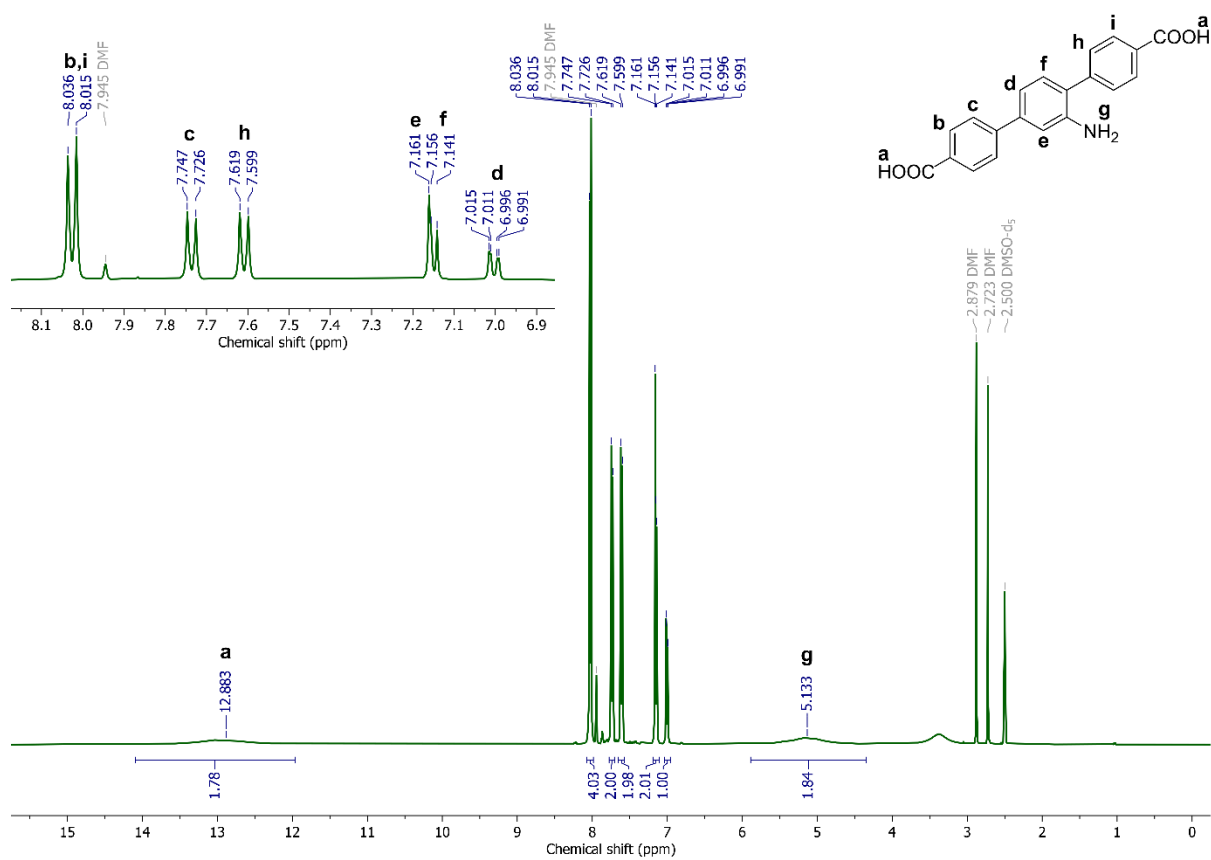


Fig. S5. ¹H NMR spectrum of tpdc-NH₂ recorded in DMSO-d₆ at 400 MHz with the structure shown in the inset.

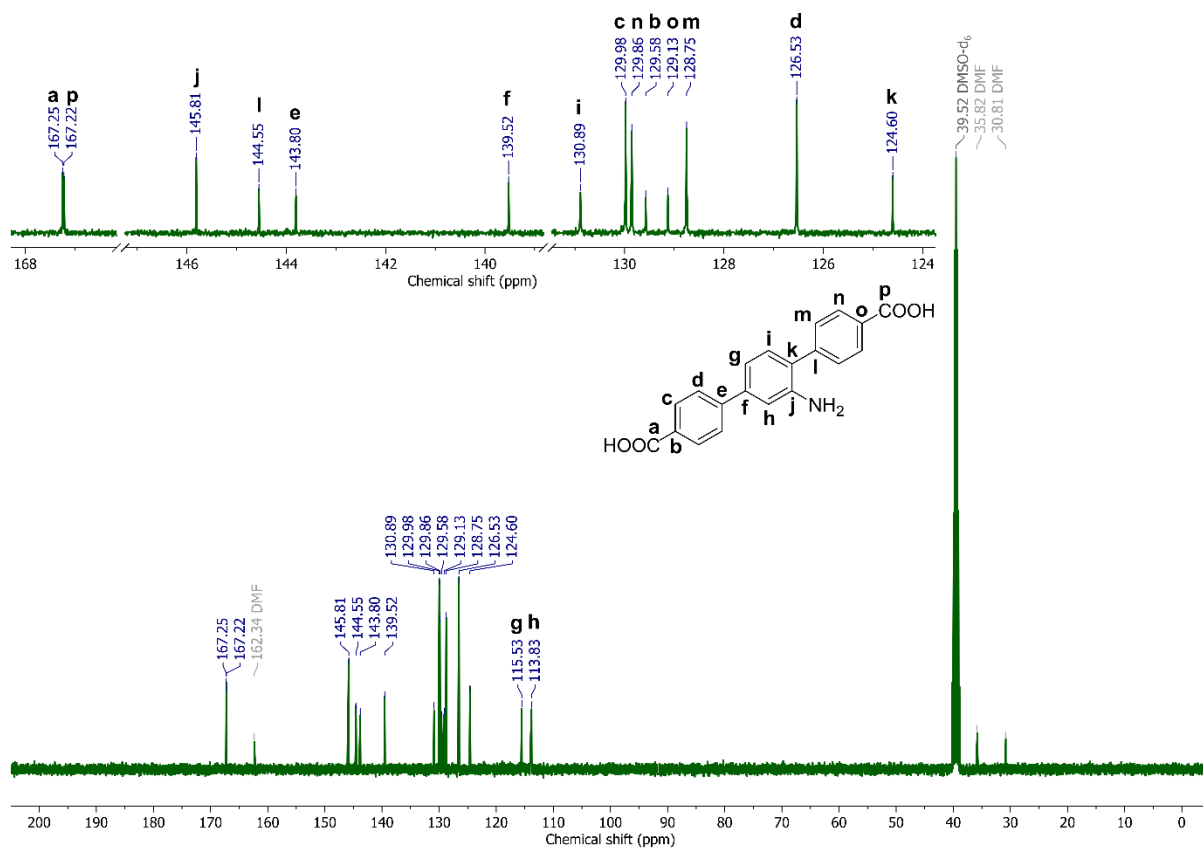


Fig. S6. ^{13}C NMR spectrum of tpdC-NH₂ recorded in DMSO-d₆ at 101 MHz with the structure shown in the inset.

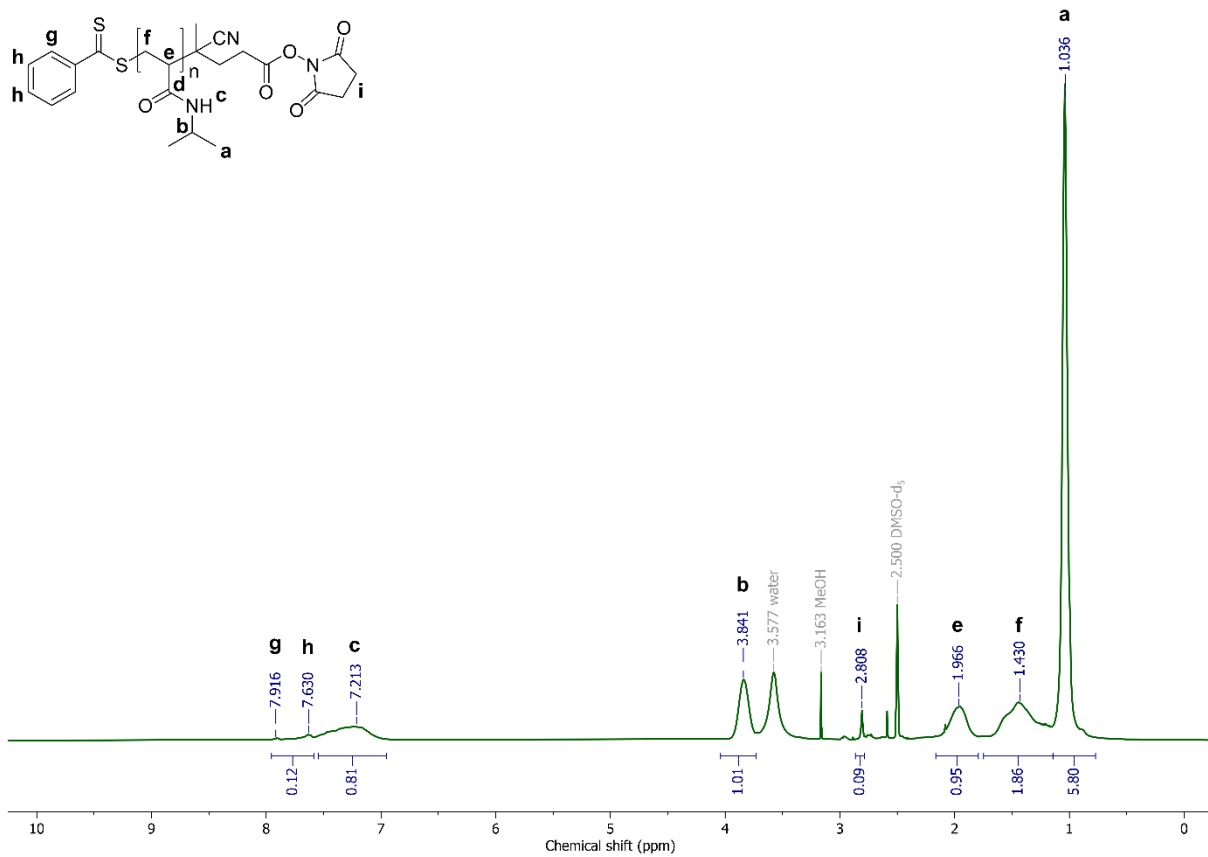


Fig. S7. ¹H NMR spectrum of PNIPAM-NHS recorded in DMSO-d₆ at 400 MHz with the structure shown in the inset.

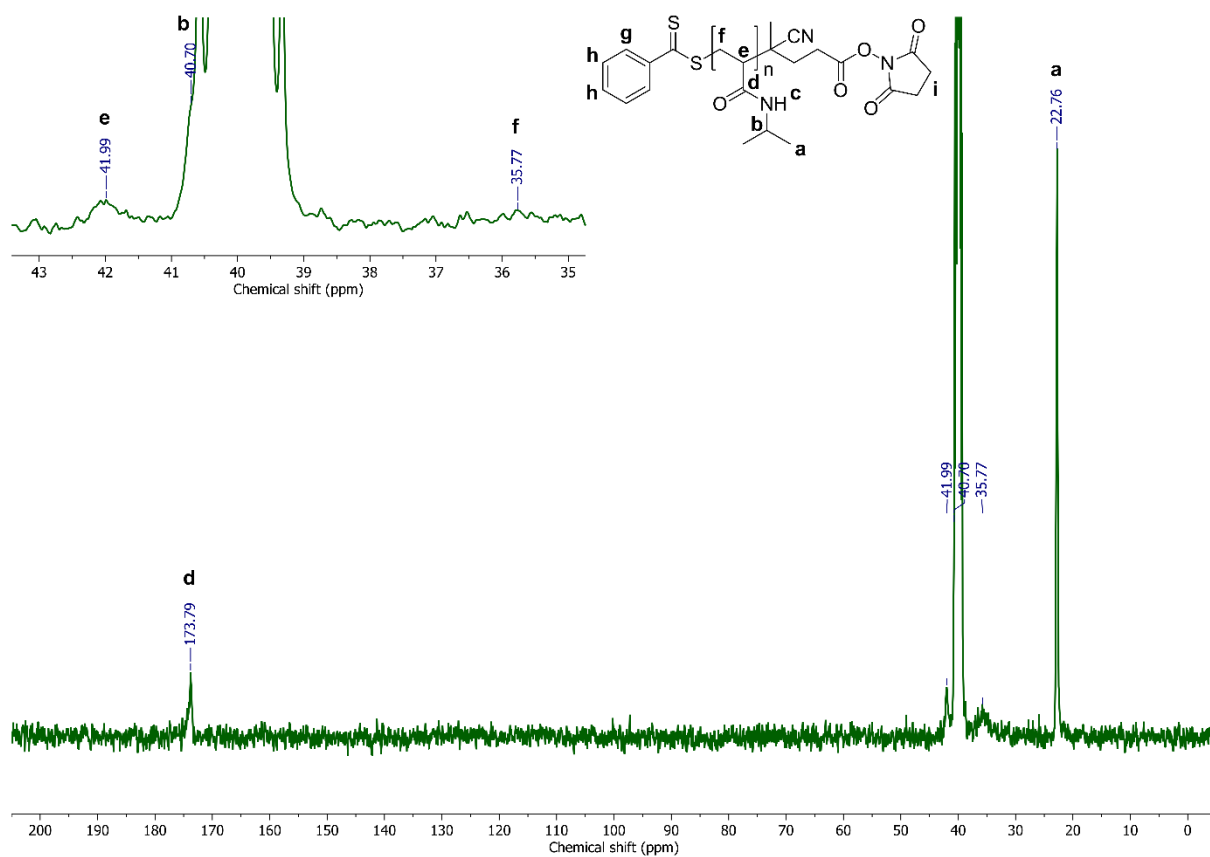


Fig. S8. ^{13}C NMR spectrum of PNIPAM-NHS recorded in DMSO-d_6 at 101 MHz with the structure shown in the inset.

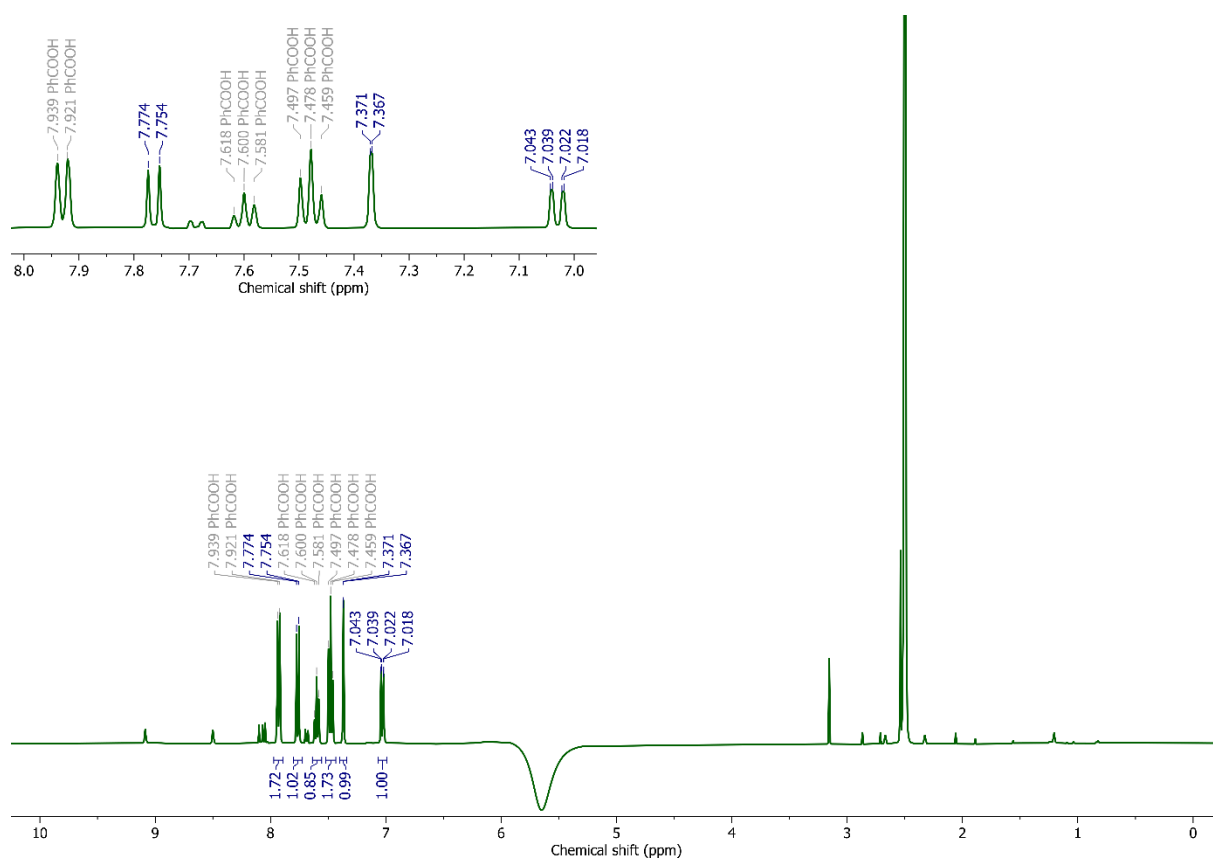


Fig. S9. ^1H NMR spectrum of UiO-66-NH₂ after digestion in HF/DMSO-d₆ at 500 MHz.

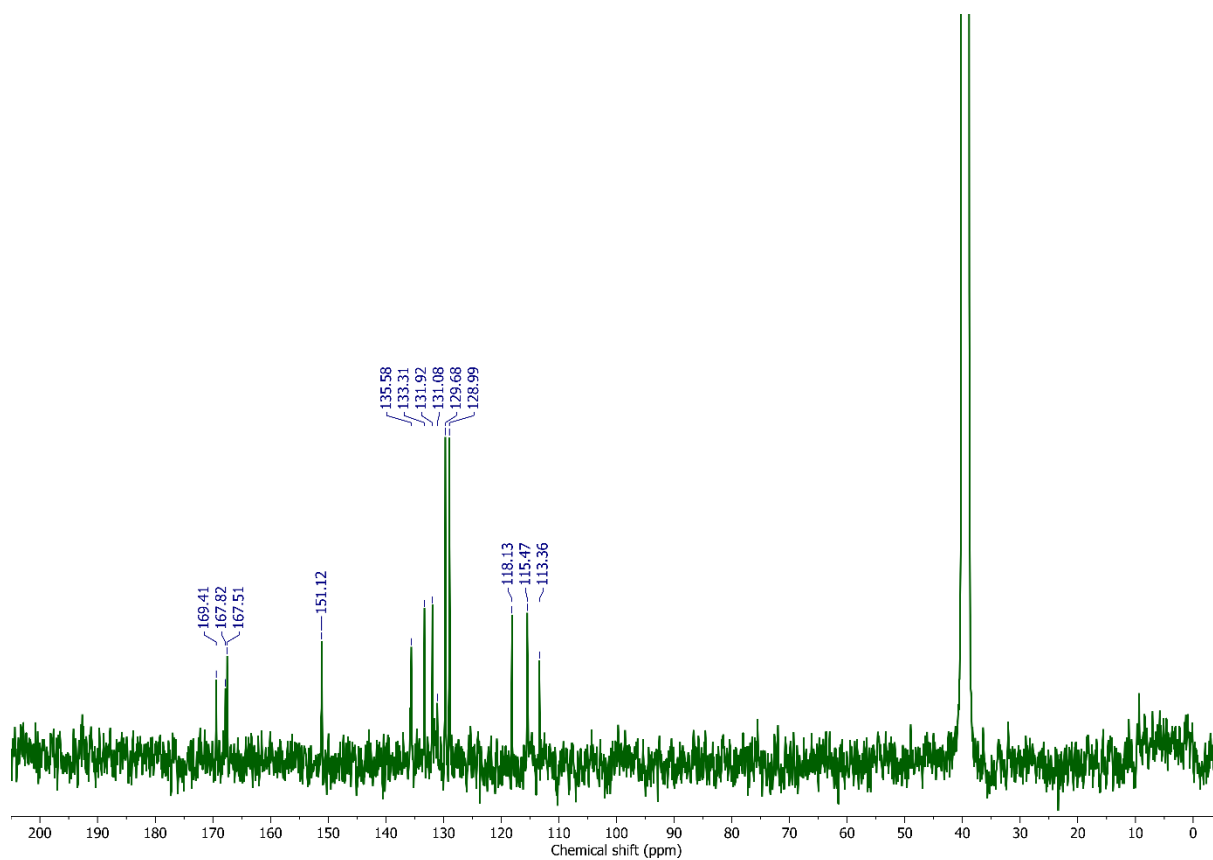


Fig. S10. ^{13}C NMR spectrum of UiO-66-NH₂ after digestion in HF/DMSO-d₆ at 126 MHz.

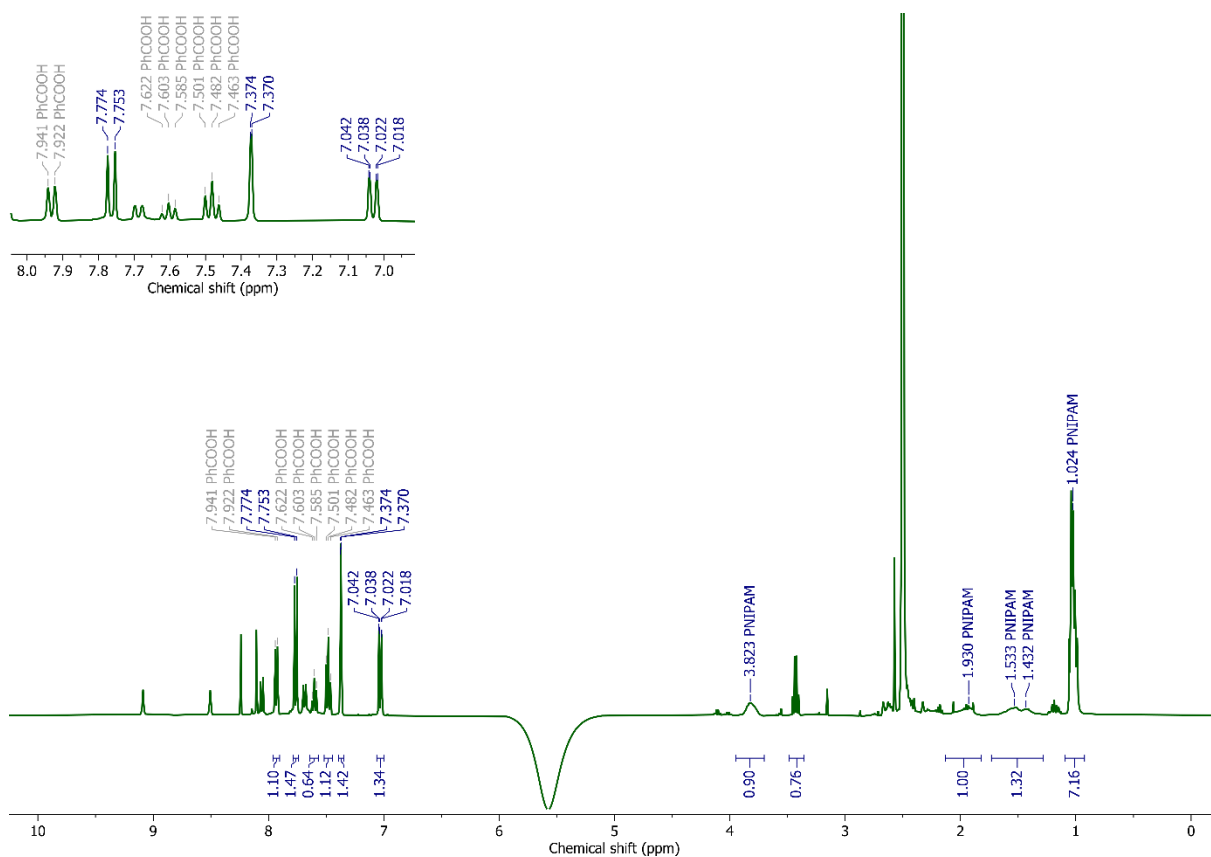


Fig. S11. ¹H NMR spectrum of UiO-66-PNIPAM after digestion in HF/DMSO-d₆ at 500 MHz.

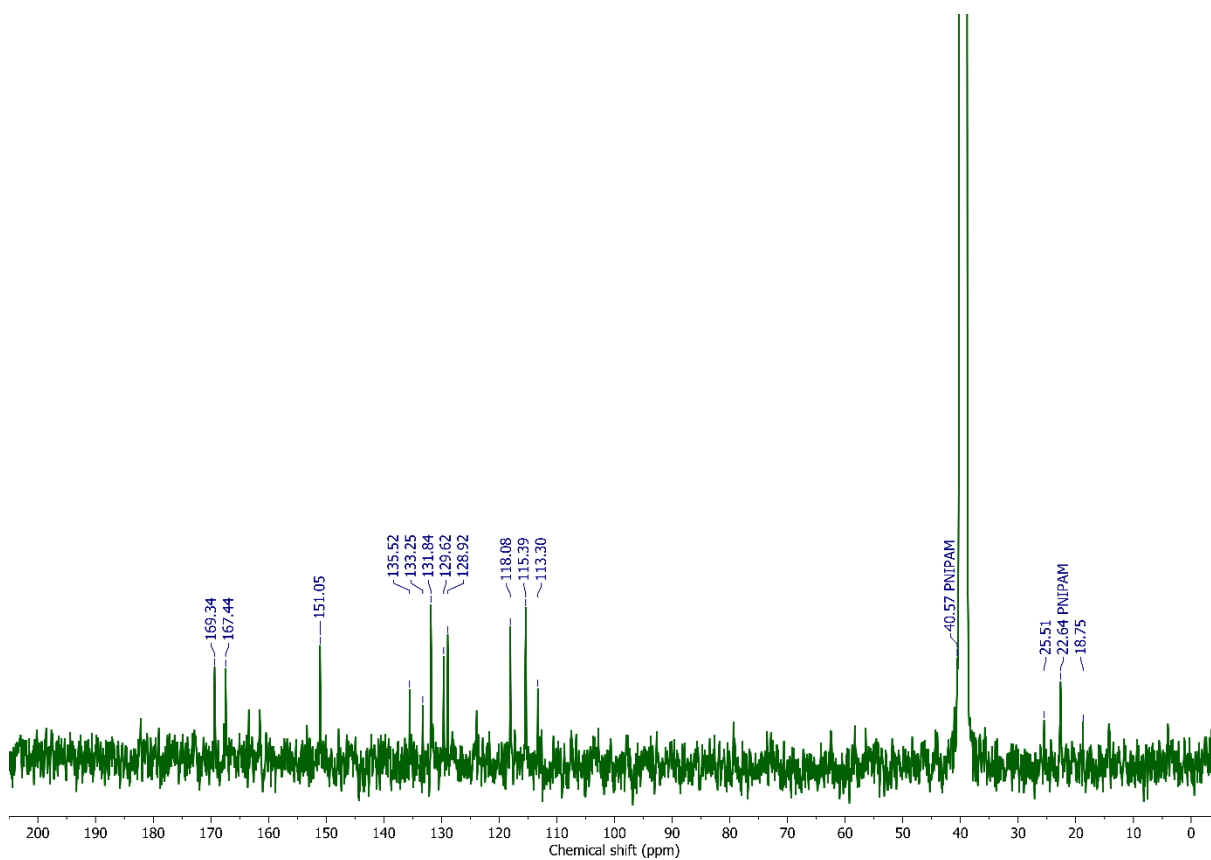


Fig. S12. ¹³C NMR spectrum of UiO-66-PNIPAM after digestion in HF/DMSO-d₆ at 126 MHz.

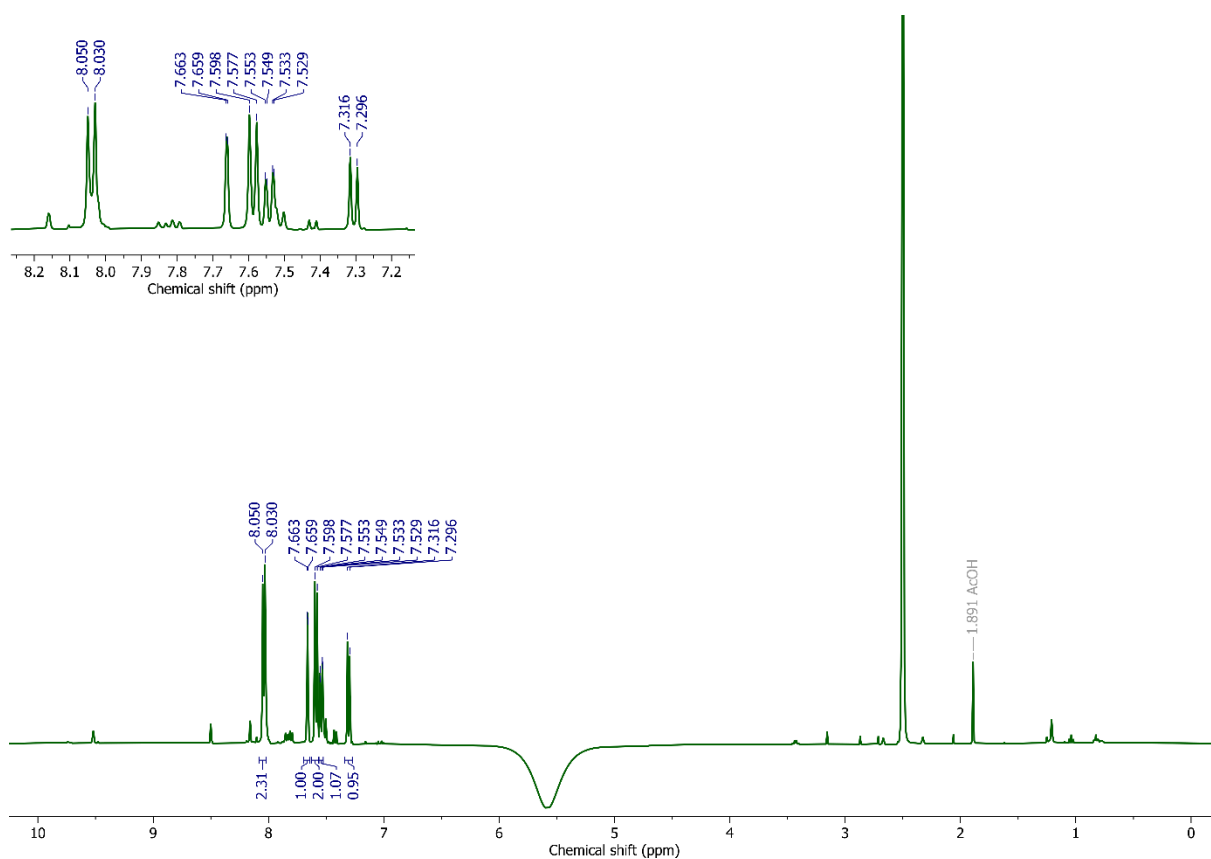


Fig. S13. ^1H NMR spectrum of UiO-67-NH₂ after digestion in HF/DMSO-d₆ at 500 MHz.

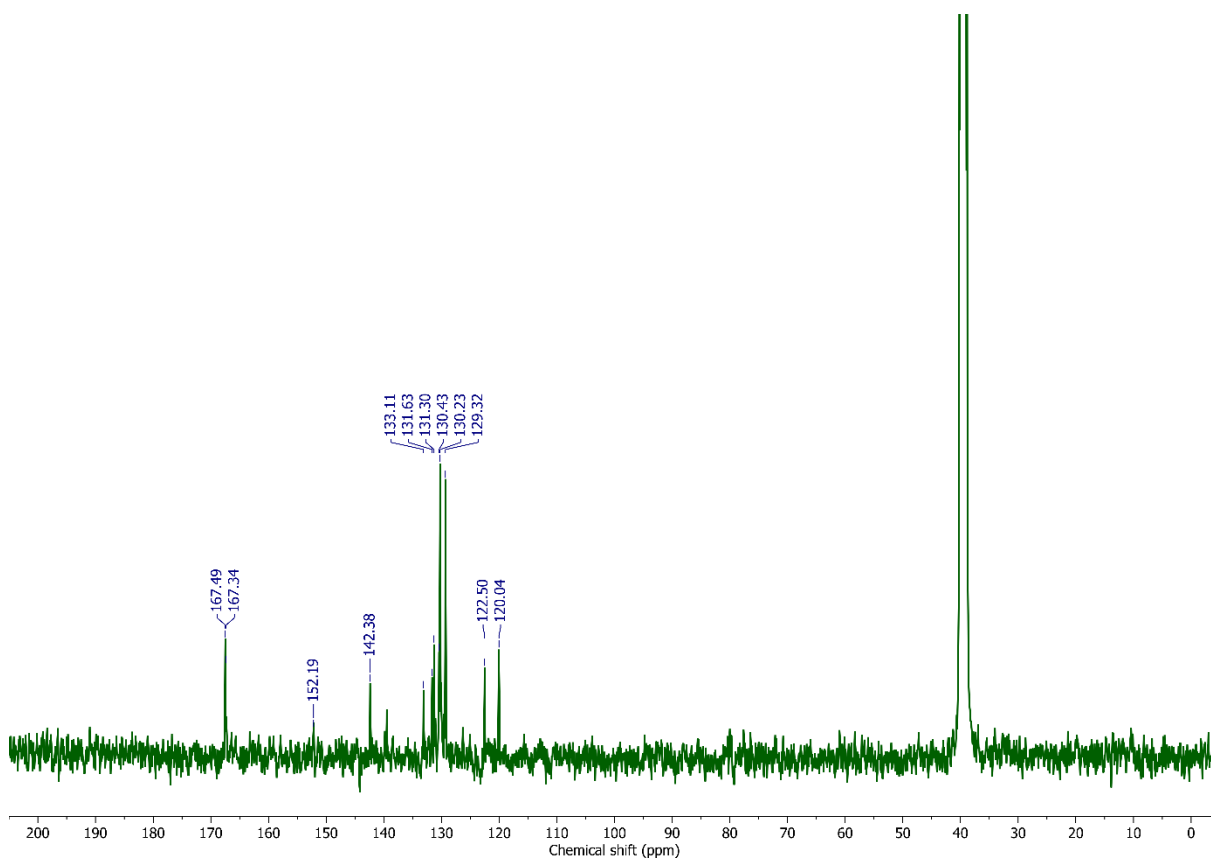


Fig. S14. ^{13}C NMR spectrum of UiO-67-NH₂ after digestion in HF/DMSO-d₆ at 126 MHz.

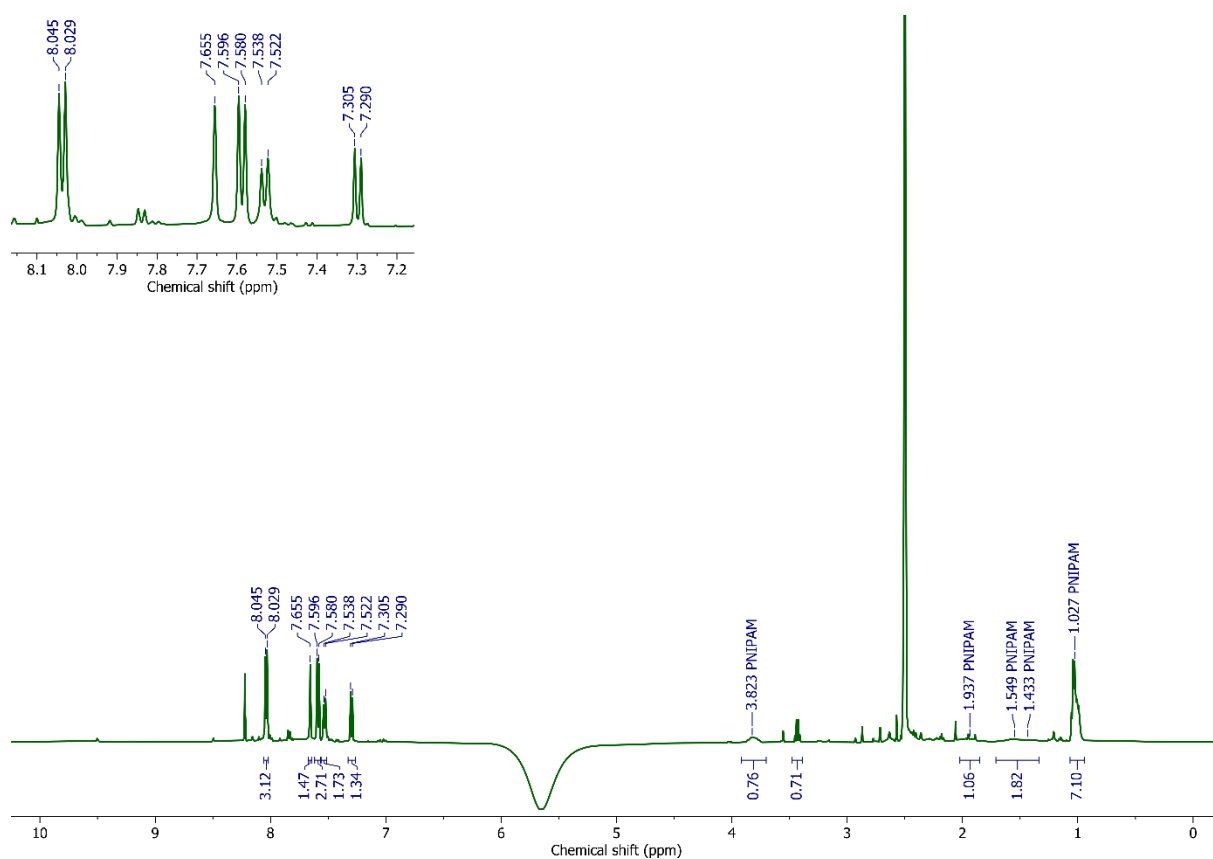


Fig. S15. ^1H NMR spectrum of UiO-67-PNIPAM after digestion in HF/DMSO- d_6 at 500 MHz.

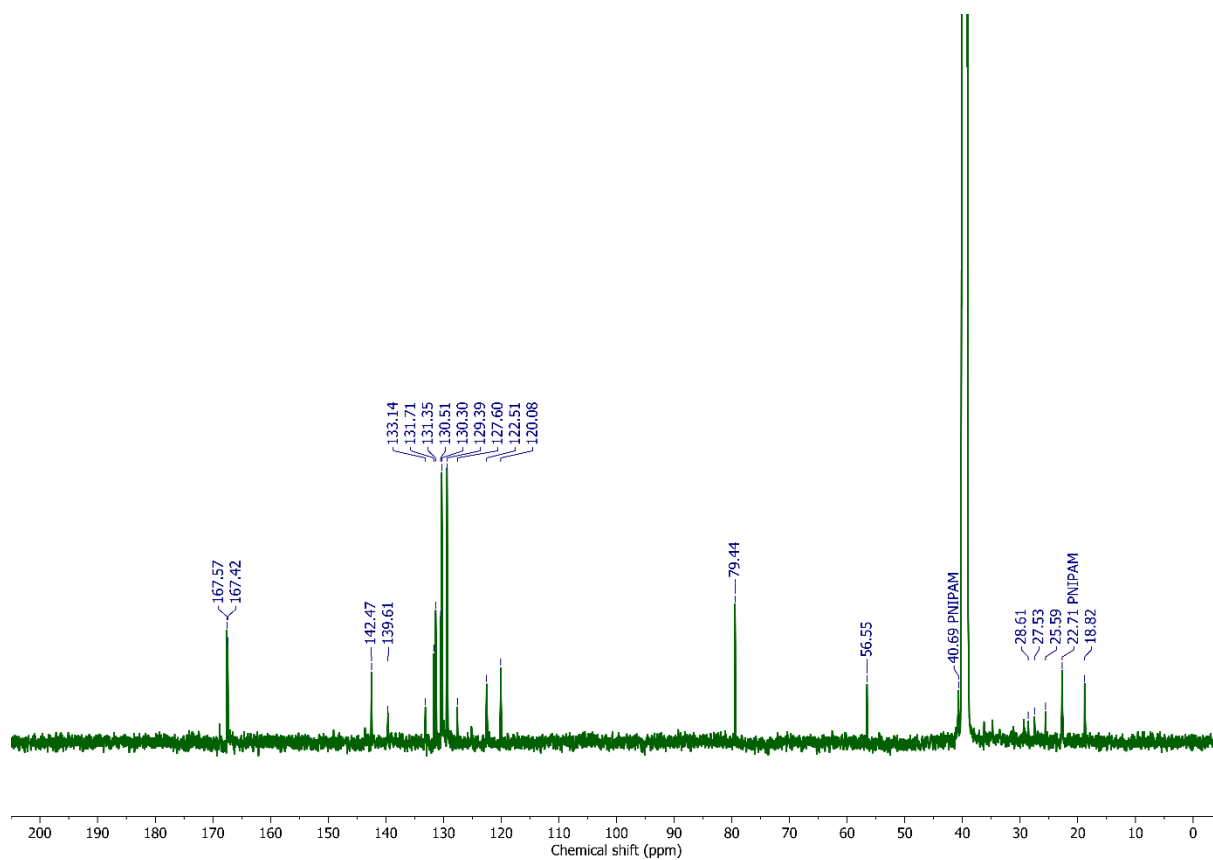


Fig. S16. ^{13}C NMR spectrum of UiO-67-PNIPAM after digestion in HF/DMSO- d_6 at 126 MHz.

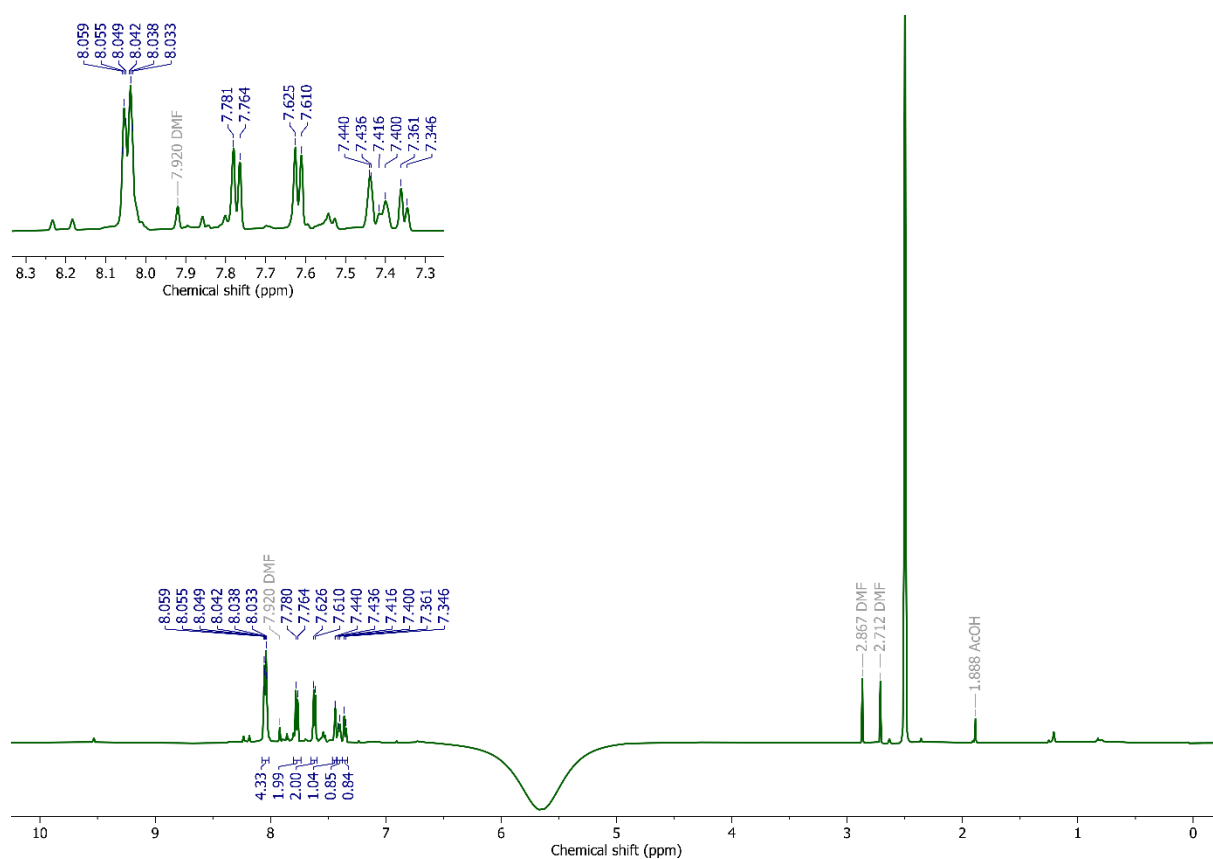


Fig. S17. ^1H NMR spectrum of UiO-68-NH₂ after digestion in HF/DMSO-d₆ at 500 MHz.

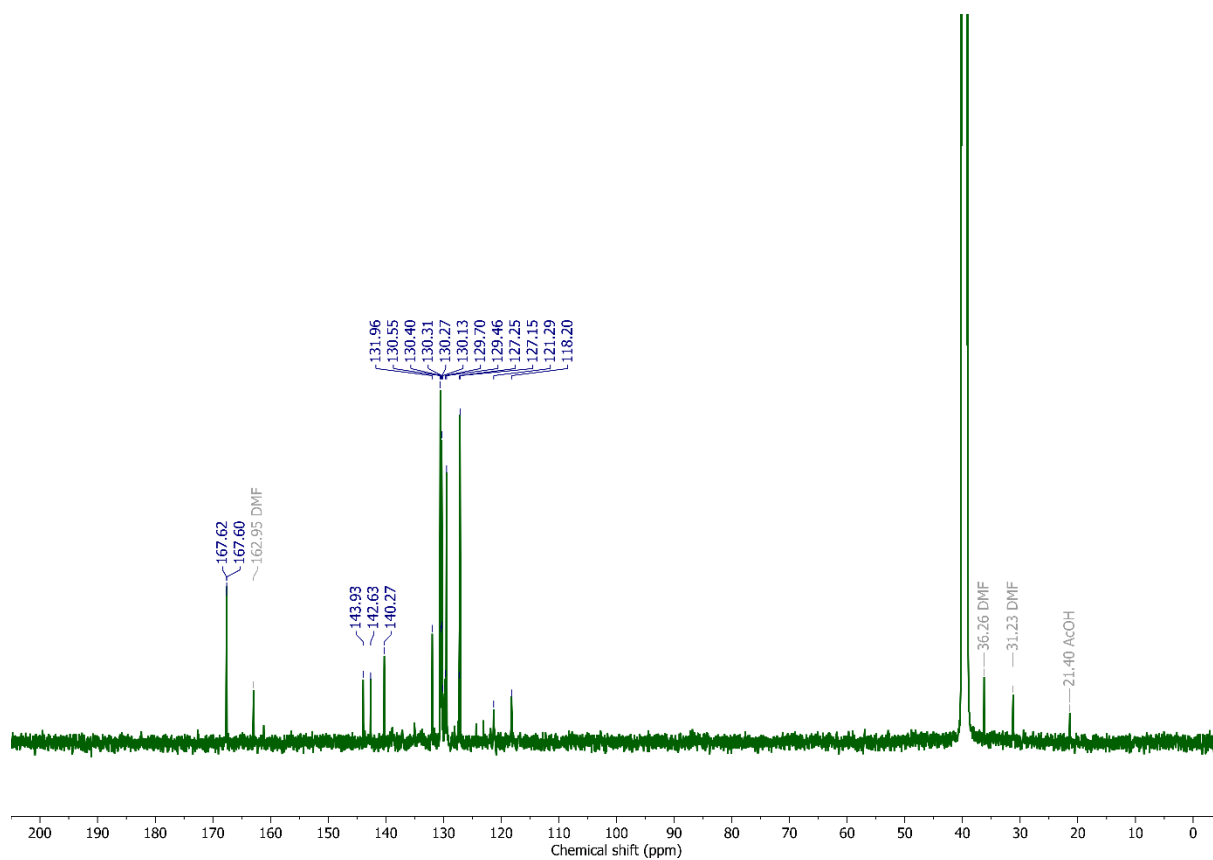


Fig. S18. ^{13}C NMR spectrum of UiO-68-NH₂ after digestion in HF/DMSO-d₆ at 126 MHz.

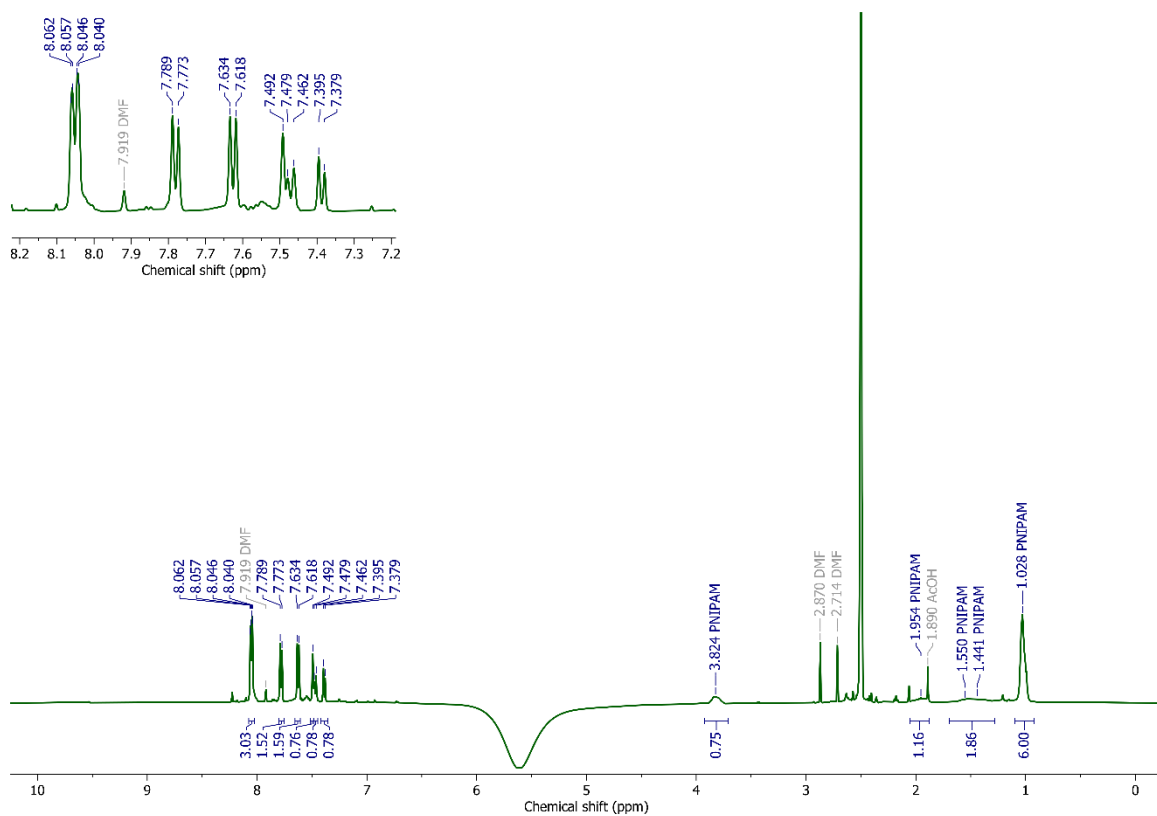


Fig. S19. ^1H NMR spectrum of UiO-68-PNIPAM after digestion in HF/DMSO- d_6 at 500 MHz.

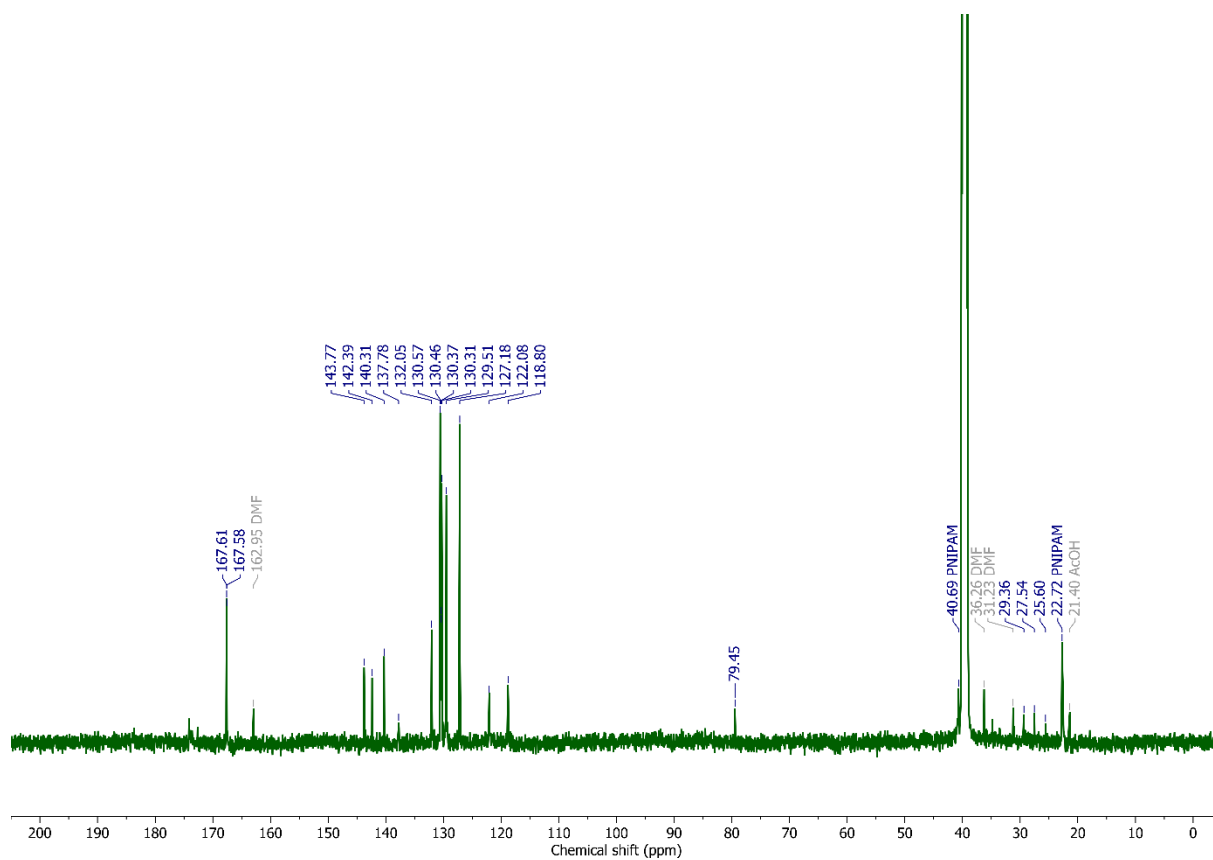


Fig. S20. ^{13}C NMR spectrum of UiO-68-PNIPAM after digestion in HF/DMSO- d_6 at 126 MHz.

5. Mass spectrometry

A Thermo Exactive plus EMR Orbitrap mass spectrometer coupled with a Thermo Ultimate 3000 UHPLC and using 100% methanol as a mobile phase was employed for accurate mass measurements. Electrospray ionization technique was used in the negative mode. Matrix-assisted laser desorption ionization (MALDI) mass spectrometric measurements were performed using a Shimadzu AXIMA Confidence instrument equipped with a 337.1-nm-wavelength nitrogen laser (power set to 132). The spectrum was acquired in the positive-ion linear mode (20 kV accelerating voltage and 5×10^{-6} mbar pressure). The sample was prepared with the CHCA matrix in MeOH.

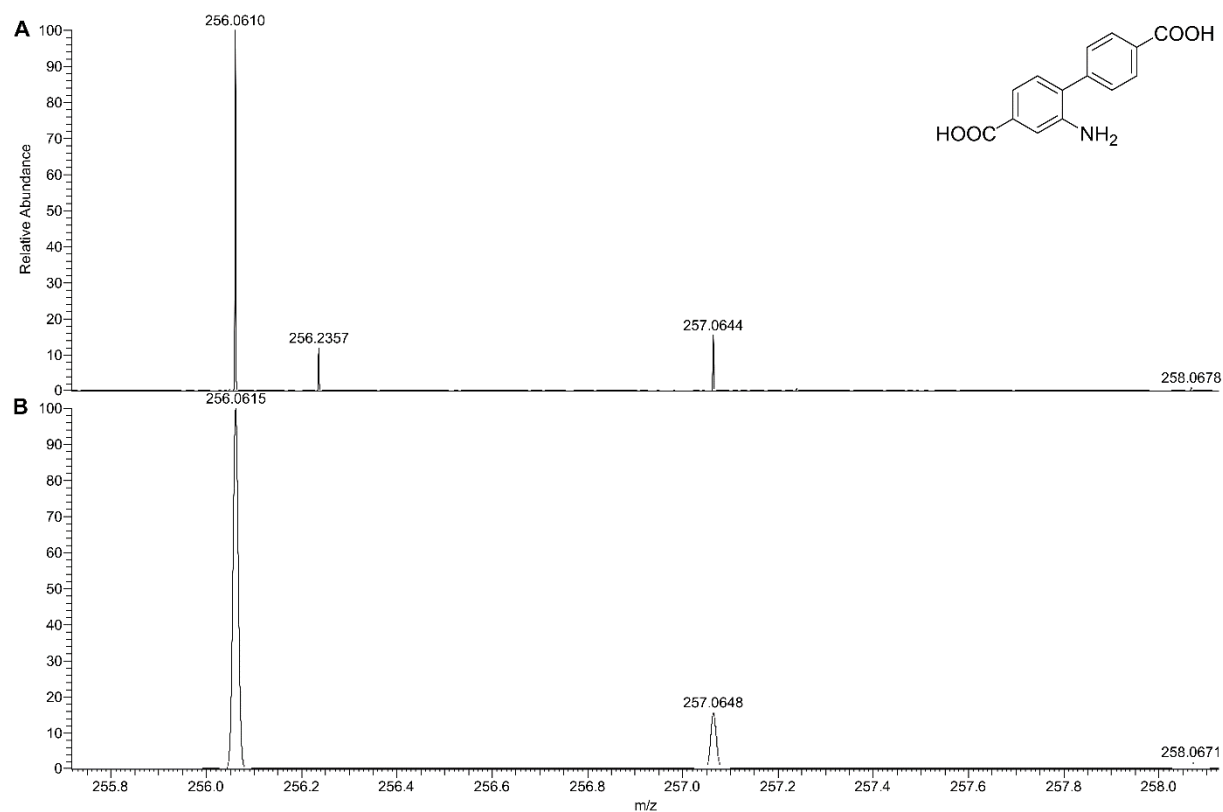


Fig. S21. a) Observed ESI⁻ high-resolution mass spectrum of bpdC-NH₂ and the b) calculated isotopic distribution of the [M-H]⁻ ion with the structure shown in the inset.

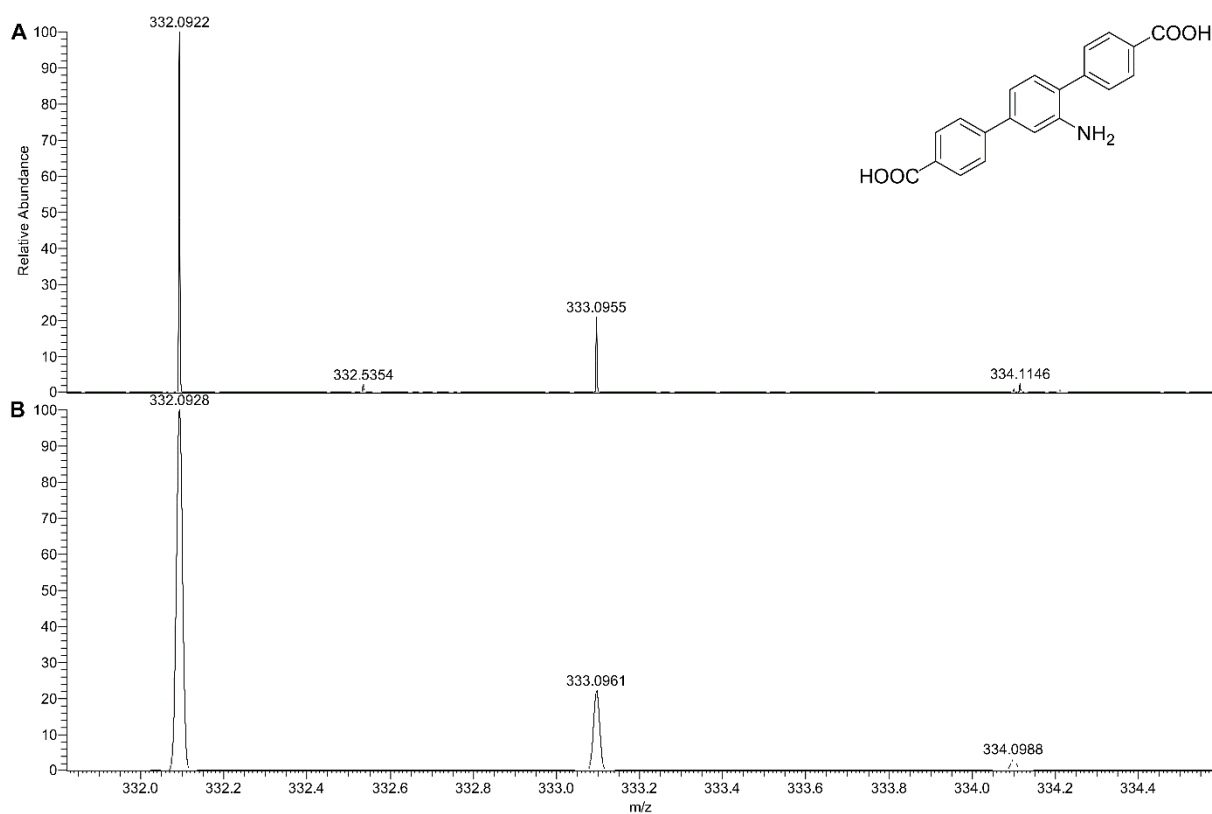


Fig. S22. a) Observed ESI⁻ high-resolution mass spectrum of tpdc-NH₂ and the b) calculated isotopic distribution of the [M-H]⁻ ion with the structure shown in the inset.

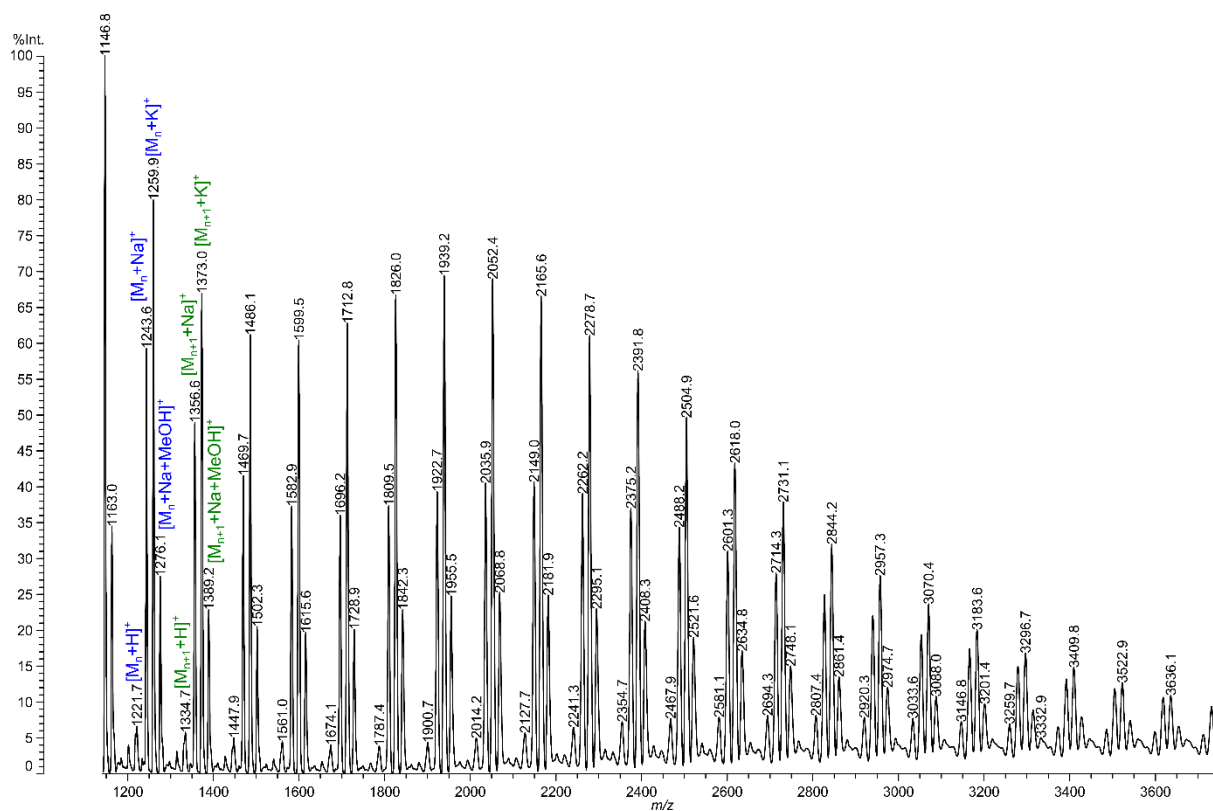


Fig. S23. MALDI spectrum of PNIPAM-NHS showing peak groups repeating by a distance of 113.1 g·mol⁻¹, which corresponds to the molecular weight of the PNIPAM repeating unit.

6. Fourier-transform infrared spectroscopy

Fourier-transform infrared (FTIR) spectra were recorded for bdp_c-NH₂, tdp_c-NH₂, and PNIPAM-NHS using a Bruker Alpha-P ATR-FTIR spectrometer. The spectra were obtained as an average of 24 scans at a resolution of 2 cm⁻¹. MOF samples were measured using a Bruker ATR-FTIR spectrometer (VERTEX 70/70v) with a total of 64 scans for each sample.

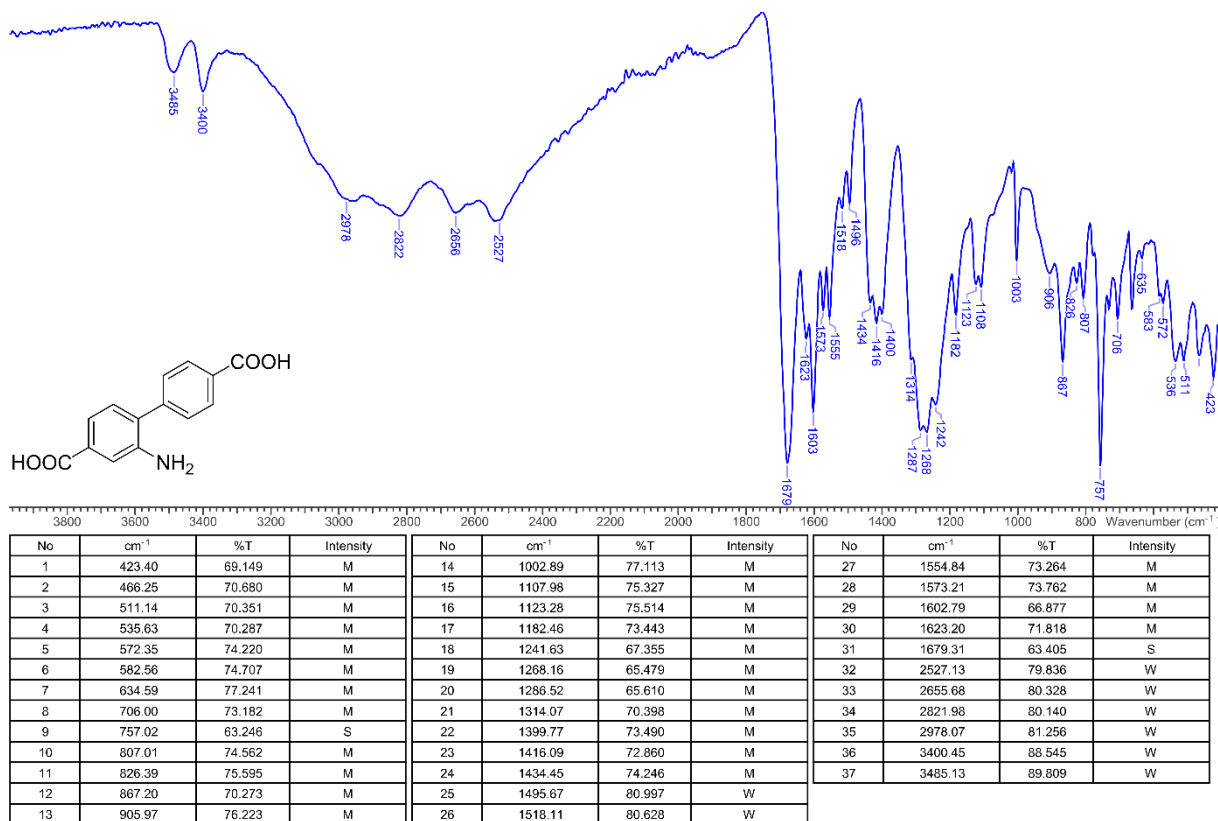


Fig. S24. FTIR spectrum of bdp_c-NH₂ with the table of peaks and the structure shown in the inset.

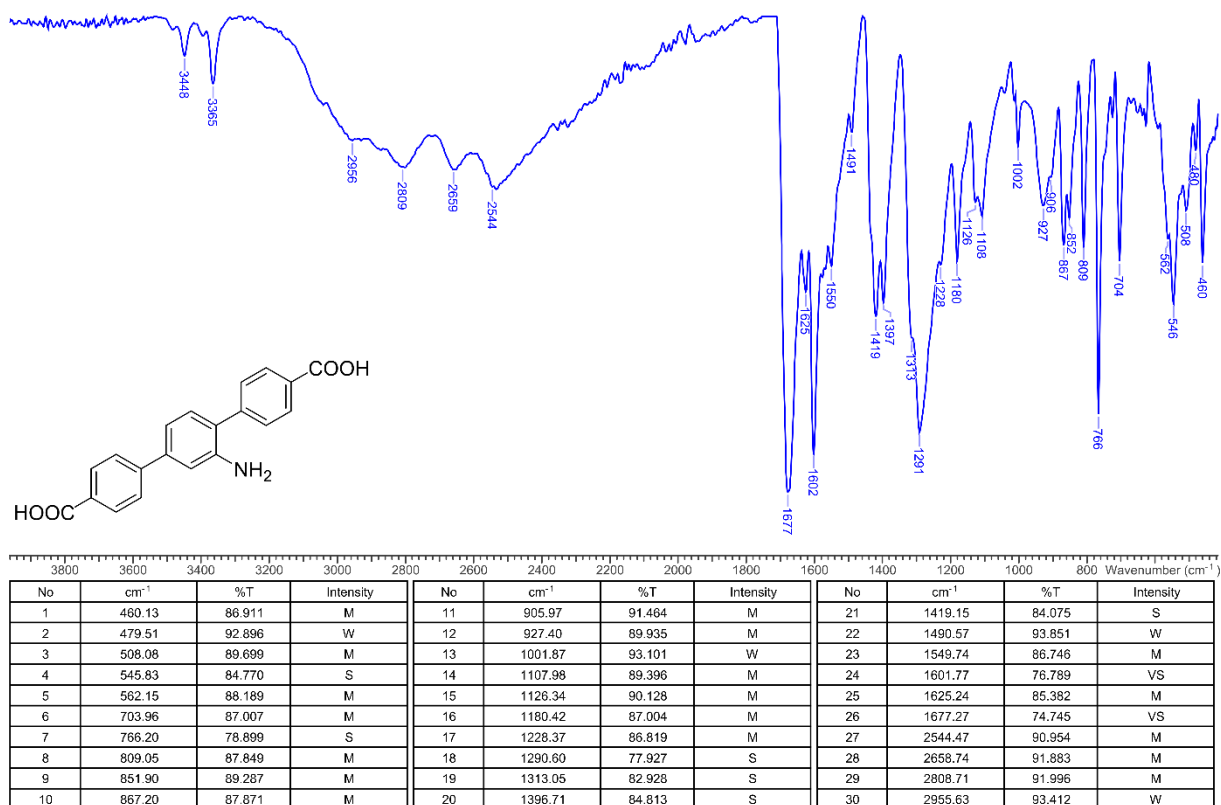


Fig. S25. FTIR spectrum of tpdc-NH₂ with the table of peaks and the structure shown in the inset.

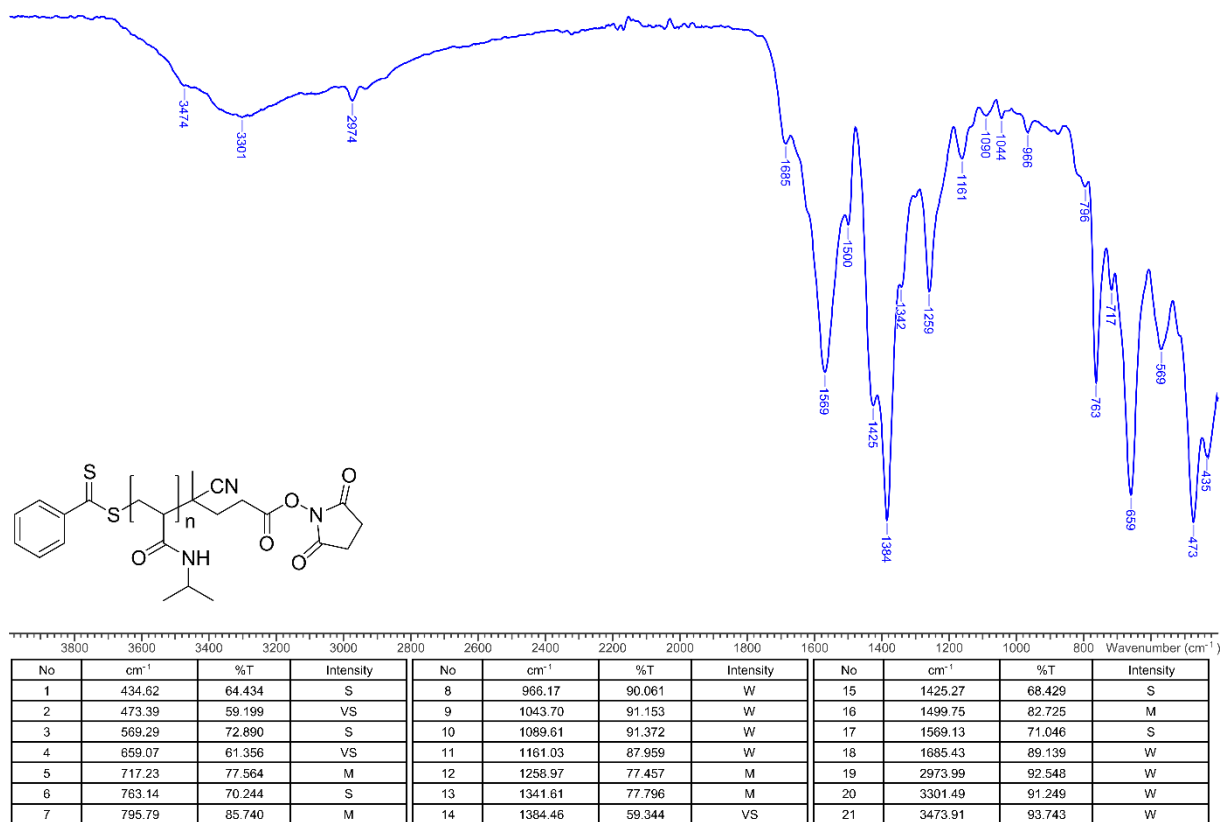


Fig. S26. FTIR spectrum of tpdc-NH₂ with the table of peaks and the structure shown in the inset.

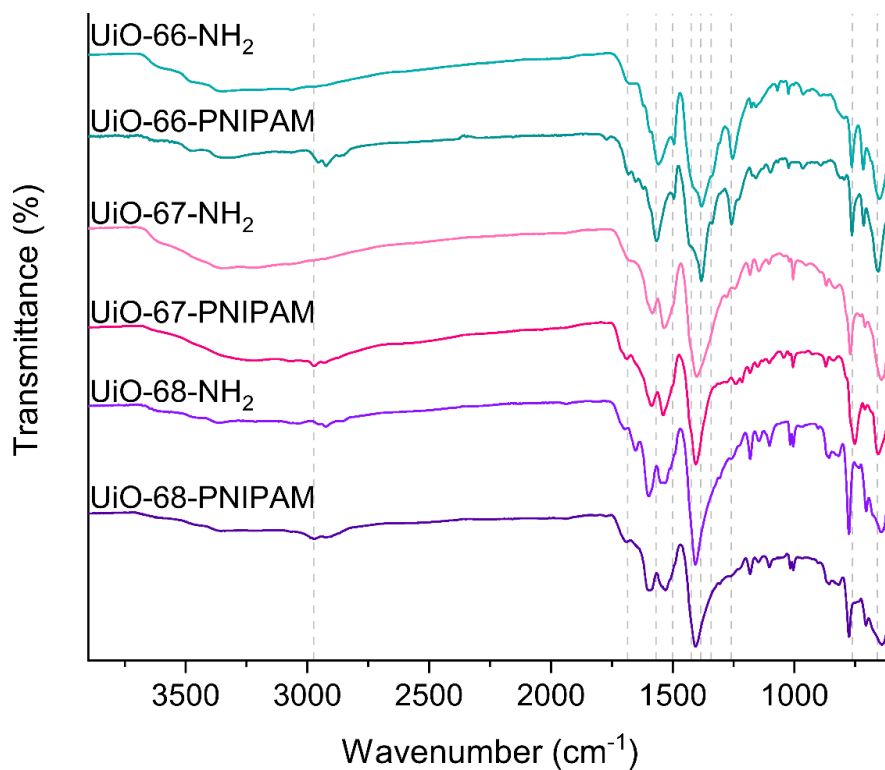


Fig. S27. FTIR spectra of pristine and PNIPAM-tethered MOFs. Gray dashed lines indicate the positions of major peaks in the FTIR spectrum of PNIPAM.

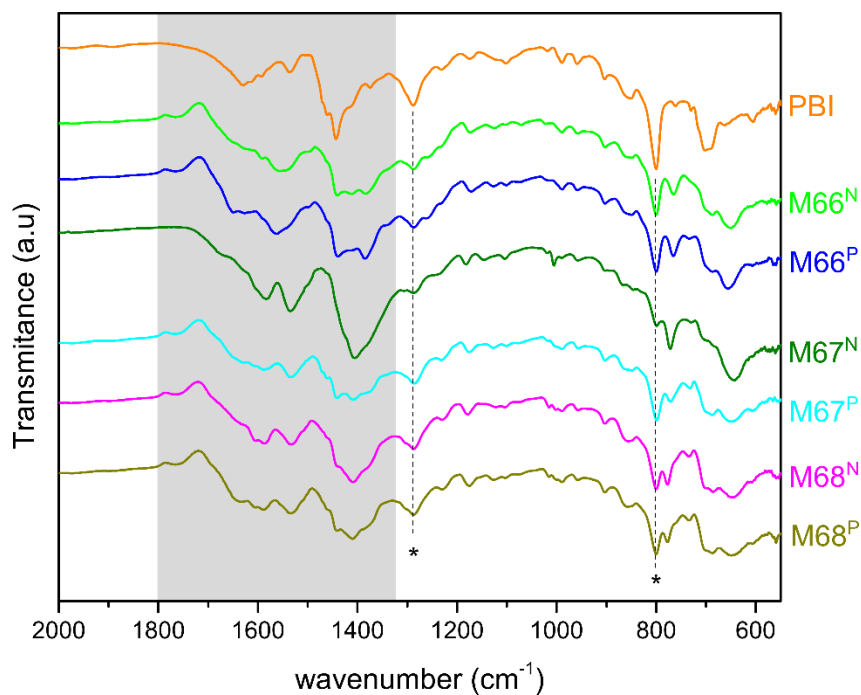


Fig. S28. FTIR spectra of PBI (orange), MMM comprising PBI with UiO-66NH₂ (green), UiO-66-PNIPAM (blue), UiO-67NH₂ (dark green), UiO-67-PNIPAM (light blue), UiO-68NH₂ (purple), and UiO-68-PNIPAM (gold). The characteristic peaks of PBI (indicated by dashed line and stars) are observed in all MMMs. The characteristic peaks for each MOF are indicated by the gray area.

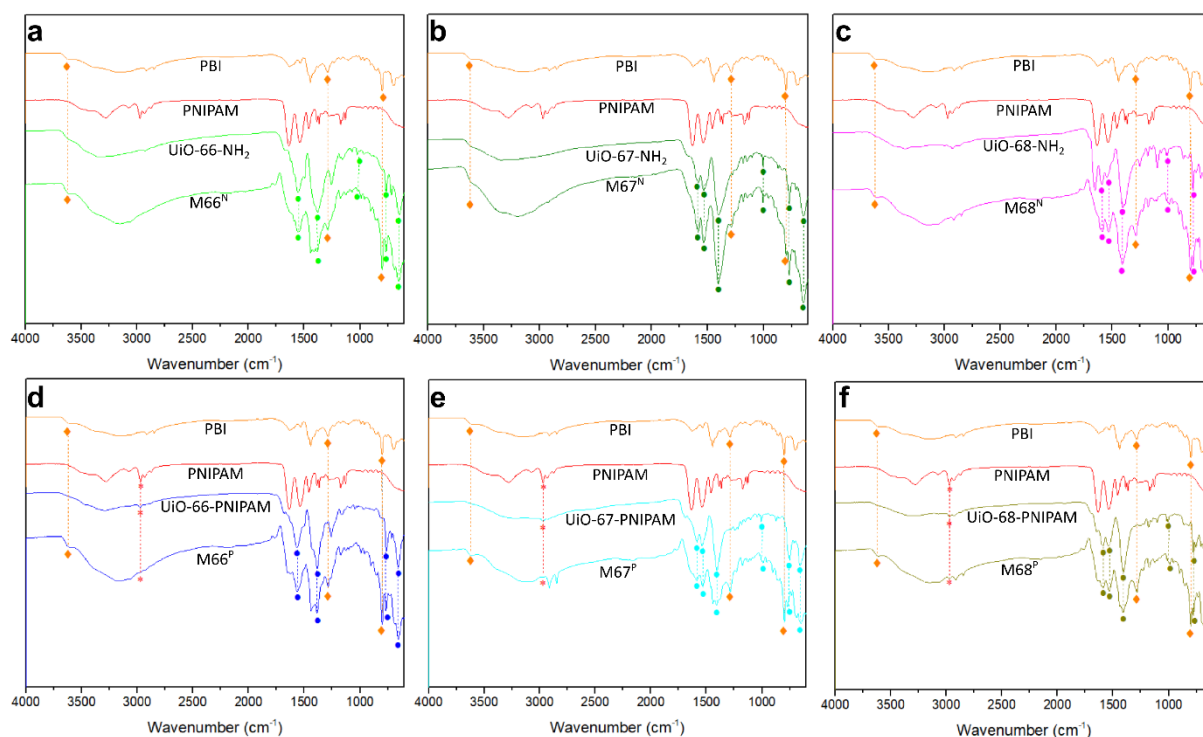


Fig. S29. Detailed comparison of the FTIR spectra of a) M66^N, b) M67^N, c) M68^N, d) M66^P, e) M67^P, and f) M68^P and their respective components.

In general, the characteristic peaks of PBI are prominent in all mixed-matrix membranes (MMMs), as shown in Fig. S28 and Fig. S29. The characteristic peaks of each MOF are in the range of 1300–1800 cm^{-1} and correspond to vibrations of organic linkers.¹ Amino-functionalized MOFs typically exhibit characteristic peaks at approximately 3477 and 3363 cm^{-1} , which are attributed to the asymmetric and symmetric vibrations of N–H bonding, respectively. However, this region also overlaps with the broad peak of adsorbed water molecules on the external and internal surface of MMMs. The FTIR spectrum of UiO-66-NH₂ shows characteristic bands resulting from C–N stretching at approximately 1257 and 1393 cm^{-1} . Characteristic N–H wagging peaks are observed at approximately 729 and 743 cm^{-1} .² The characteristic peak of the Zr–O mode (at approximately 764 cm^{-1}) can also be observed.³ The peak at approximately 1621 cm^{-1} corresponds to the N–H bending vibration. The peaks at approximately 1482 and 1382 cm^{-1} can be attributed to N–H bending and C–N stretching vibrations, respectively.⁴ The three peaks in the spectrum of UiO-67-NH₂ at approximately 793, 722, and 662 cm^{-1} correspond to Zr–O longitudinal and transverse mode vibrations. The sharp and intense peaks at approximately 1615 and 1417 cm^{-1} correspond to in-plane and out-of-plane stretching of the carboxylate groups of the ligand, respectively.⁵ Zr–O–Zr and Zr–O stretches are indicated by peaks at approximately 661 and 462 cm^{-1} , respectively.⁶ IR bands are present at approximately 671 cm^{-1} (Zr– μ_3 -O stretching), 1409 cm^{-1} (C=O stretching), and 1593 cm^{-1} (C=C stretching). The low frequency of the carbonyl stretching band, which is usually observed at approximately 1750 cm^{-1} for free carbonyls, can be explained by the coordination of the linker carboxylate group to high molecular weight Zr atoms.⁷

7. Size exclusion chromatography

SEC was performed using a SHIMADZU LC-20AD system (SHODEX K-805L and K-803L) equipped with a SHIMADZU SPD-20A UV detector using chloroform as an eluent at 40°C after calibration with standard polystyrene samples.

Fig. S30 shows the molecular weight distribution of PNIPAM-NHS obtained via SEC. Results show that PNIPAM-NHS had number average and weight average molecular weights (M_n and M_w) of 4100 $\text{g}\cdot\text{mol}^{-1}$ and 5400 $\text{g}\cdot\text{mol}^{-1}$, respectively. The polymer exhibits relatively low polydispersity with a M_w/M_n ratio of 1.31.

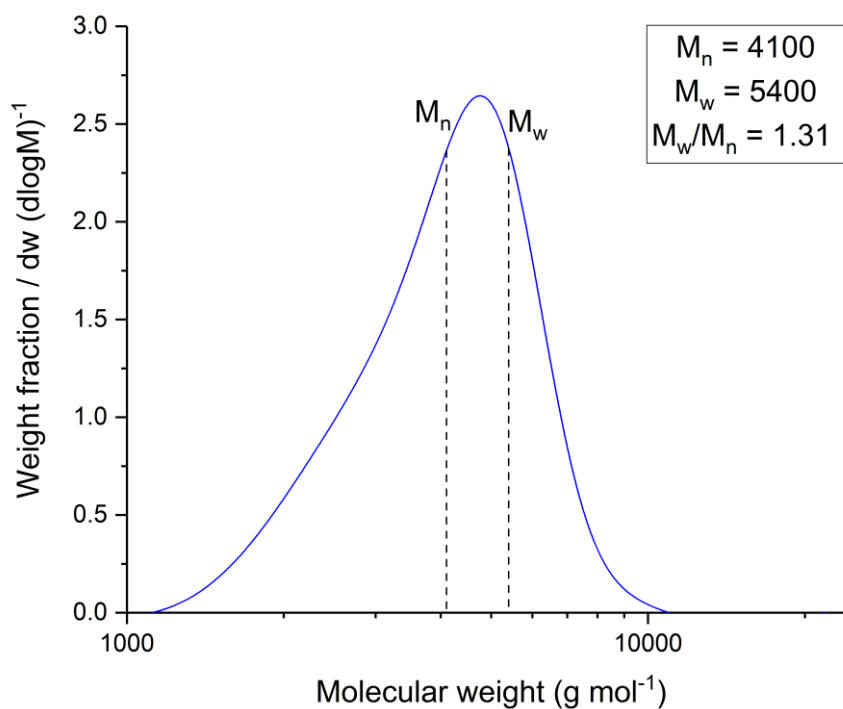


Fig. S30. Molecular weight distribution of PNIPAM-NHS obtained via GPC.

8. Elemental analysis

Determination of organic elements (C, H, N, S, and O) was performed in a Flash 2000 organic elemental analyzer (Thermo Fisher Scientific). Approximately 2 mg of the sample was weighed, wrapped, and placed in a tin crucible to be inserted into the analyzer furnace. For sulfur content analysis, approximately 10 mg of vanadium pentoxide powder was mixed with the sample.

Table S1. Elemental analysis of the synthesized MOFs and their polymer-tethered counterparts. n.a.: not analyzed

| Element | UiO-66 | | | UiO-67 | | | UiO-68 | | |
|---------|----------------------------|---------------------------|------------------|----------------------------|---------------------------|------------------|----------------------------|---------------------------|------------------|
| | Calc. for -NH ₂ | Obs. for -NH ₂ | Obs. for -PNIPAM | Calc. for -NH ₂ | Obs. for -NH ₂ | Obs. for -PNIPAM | Calc. for -NH ₂ | Obs. for -NH ₂ | Obs. for -PNIPAM |
| O | 29.22 | 27.82 | 26.44 | 23.19 | 24.45 | 27.12 | 19.22 | 17.23 | 20.23 |
| C | 32.88 | 32.87 | 32.36 | 45.65 | 40.66 | 40.66 | 54.05 | 48.84 | 47.96 |
| H | 1.94 | 3.22 | 3.83 | 2.63 | 4.46 | 4.46 | 3.08 | 4.37 | 3.91 |
| N | 4.79 | 2.65 | 3.94 | 3.80 | 3.37 | 3.37 | 3.15 | 3.31 | 3.03 |
| S | 0.00 | n.a. | 0.7 | 0.00 | n.a. | 0.4 | 0.00 | n.a. | 0.5 |

9. Dynamic light scattering for particle size analysis

Particle size and zeta potential were determined using a Malvern Zetasizer Nano instrument capable of simultaneously measuring the dynamic light scattering (DLS) and electrophoretic light scattering (for zeta potential). Prior to the measurement, approximately 0.5 mg of the fine sample powder was dispersed in 1 mL of deionized water followed by ultrasonication for 5 min. The measurements were repeated thrice for each material to obtain the standard deviation.

Table S2. Particle size and zeta potential determined via dynamic light scattering.

| | Particle size (nm) | Zeta potential (mV) |
|------------------------|--------------------|---------------------|
| UiO-66-NH ₂ | 535 ± 19 | 33.8 ± 0.4 |
| UiO-66-PNIPAM | 452 ± 136 | 54.3 ± 1.0 |
| UiO-67-NH ₂ | 532 ± 196 | 19.3 ± 0.5 |
| UiO-67-PNIPAM | 600 ± 211 | 24.3 ± 0.8 |
| UiO-68-NH ₂ | 771 ± 171 | 28.0 ± 0.6 |
| UiO-68-PNIPAM | 651 ± 195 | 41.6 ± 0.5 |

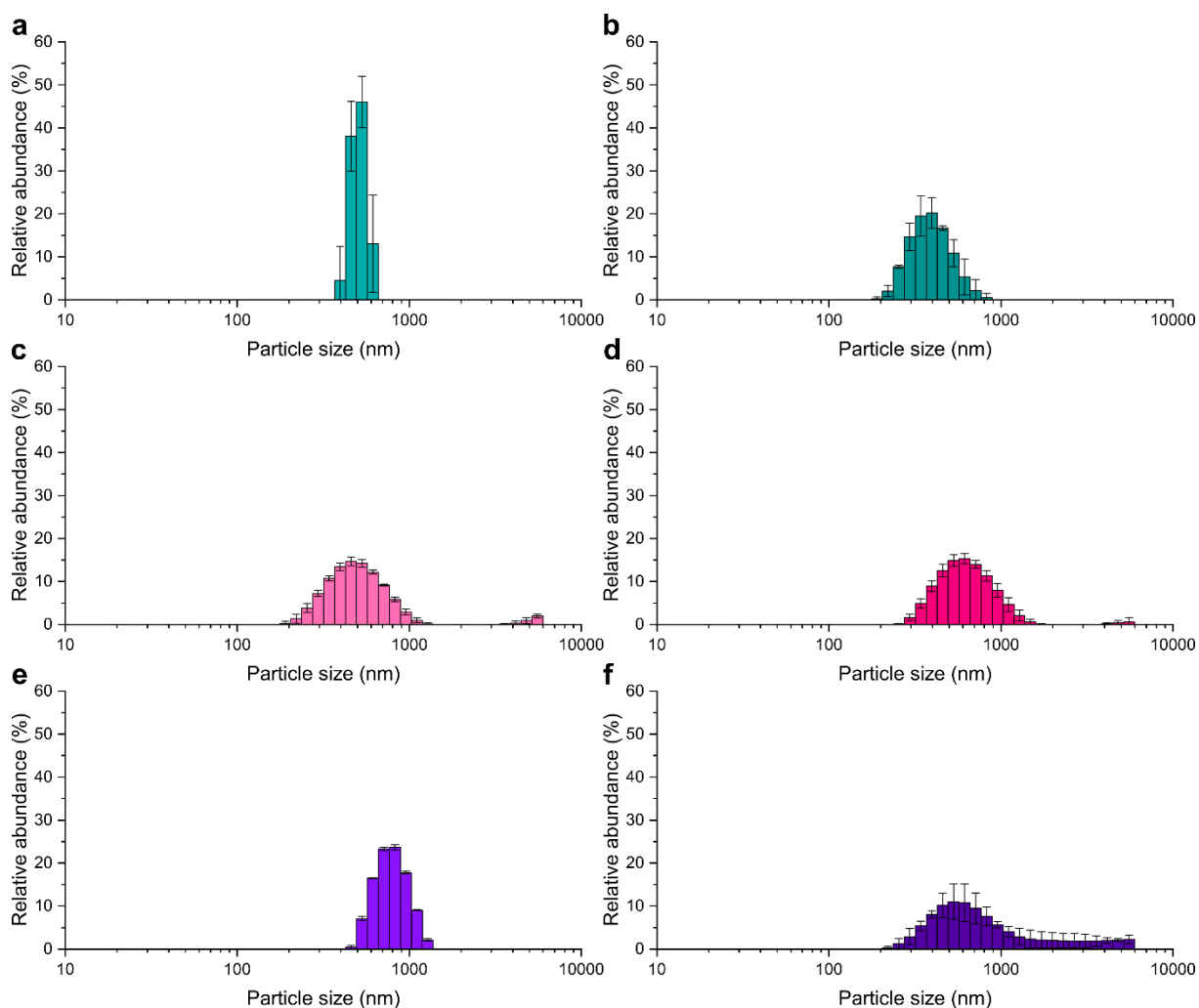


Fig. S31. Particle size distribution of a) UiO-66-NH₂, b) UiO-66-PNIPAM, c) UiO-67-NH₂, d) UiO-67-PNIPAM, and e) UiO-68-NH₂ and UiO-68-PNIPAM determined via DLS.

10. MOF-PNIPAM coverage calculations

PNIPAM modification given in weight percentage and surface coverage were calculated using experimental NMR, elemental analysis, and DLS experiments. Digestion NMR spectra of MOF-PNIPAMs were used to calculate the PNIPAM-repeating-unit-linker mole ratio ($n_{\text{PNIPAMrep}}/n_{\text{linker}}$). The moles of linkers equal the moles of nitrogen in unmodified MOF-NH₂. Using nitrogen mass fraction from the elemental analysis ($x_{\text{N,MOF-NH}_2}$), the PNIPAM weight percentage can be calculated according to Equation (S1).

$$x_{\text{PNIPAM}} = \frac{\frac{n_{\text{PNIPAMrep}}}{n_{\text{linker}}} M_{\text{PNIPAMrep}}}{\frac{n_{\text{PNIPAMrep}}}{n_{\text{linker}}} M_{\text{PNIPAMrep}} + x_{\text{N,MOF-NH}_2} M_{\text{N}}} \cdot 100\% \quad (\text{S1})$$

where $M_{\text{PNIPAMrep}}$ and M_{N} are the molecular weights of the PNIPAM repeating unit and nitrogen, respectively.

To estimate the PNIPAM surface coverage, several assumptions and approximations were required. First, the MOF particles were assumed to be perfect octahedrons with a circumscribed sphere diameter that was equal to the average particle size obtained from DLS experiments. Second, PNIPAM chains were assumed to have equal lengths. The number of repeating units in the chain was obtained as the quotient of the PNIPAM molecular weight and molecular weight of the repeating unit. This is not necessarily a whole number that does not have physical meaning; however, this was disregarded as part of the approximations. Assuming perfect crystal structure and using geometric considerations (Fig. S32), the number of linker molecules in one octahedral crystal ($n_{\text{linker,oct}}$) can be calculated from the particle size (d) and metal center distance (a). The PNIPAM-repeating-unit-linker mole ratio allows calculating the estimated average number of PNIPAM chains belonging to one crystal with a surface of A_{oct} ; thus, the PNIPAM coverage (ρ_{PNIPAM}) in nm⁻² can be calculated as

$$\rho_{\text{PNIPAM}} = \frac{n_{\text{linker,oct}}}{\frac{n_{\text{PNIPAMrep}}}{n_{\text{linker}}} \frac{M_{\text{PNIPAM}}}{M_{\text{PNIPAMrep}}}} \frac{1}{A_{\text{oct}}} \quad (\text{S2})$$

where M_{PNIPAM} is the number averaged molecular weight of PNIPAM (2000 g·mol⁻¹).

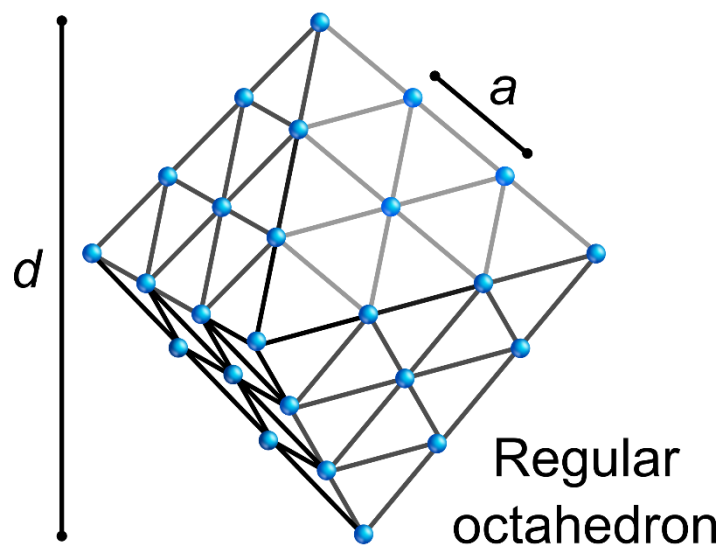


Fig. S32. Geometry of octahedral MOF crystals used for the PNIPAM coverage calculations. The spheres and lines represent the metal nodes and linkers, respectively.

Table S3. PNIPAM content and surface coverage of the MOF-PNIPAM particles determined from NMR, elemental analysis, and DLS results.

| MOF-PNIPAM | PNIPAM content/ x_{PNIPAM} (wt.%) | PNIPAM coverage/ ρ_{PNIPAM} (nm^{-2}) |
|---------------|---|---|
| UiO-66-PNIPAM | 13.1 | 4.68 |
| UiO-67-PNIPAM | 15.6 | 2.80 |
| UiO-68-PNIPAM | 25.5 | 3.77 |

11. X-ray powder diffraction

X-ray powder diffraction (XPRD) patterns were obtained using Bruker D8Advance with a Cu K α radiation source (40 kV, 40 mA).

XRPD patterns of all synthesized MOFs and their PNIPAM-tethered counterparts were recorded. The experimental patterns were compared with the simulated pattern corresponding to the crystal structures of UiO-66-NH₂ (ID: 1507786), UiO-67-NH₂ (ID: 1026990), and UiO-68-NH₂ (ID: 1847052) from the Cambridge Structural Database (CCDC).⁸ The simulation was performed using the Mercury 2020.1 software for the Cu K α radiation source.

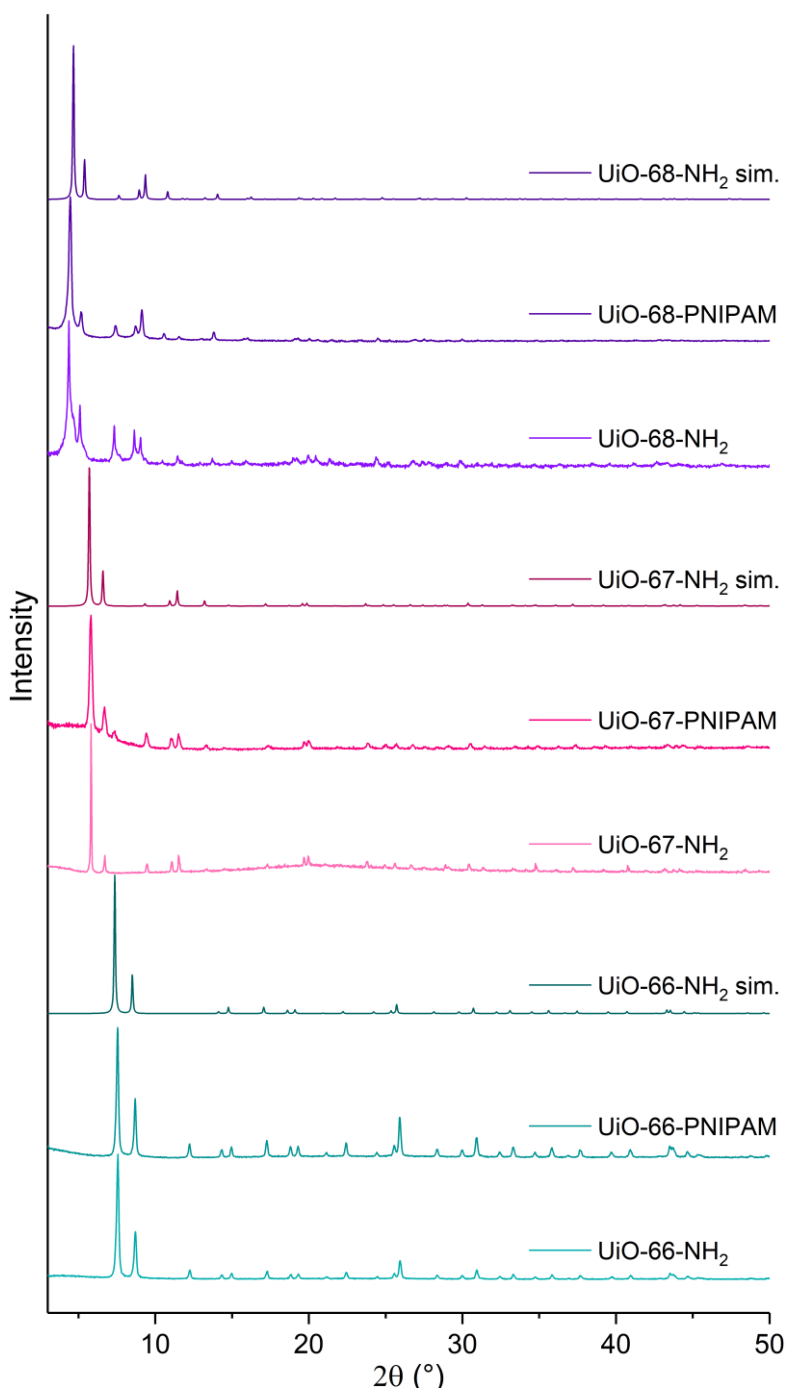


Fig. S33. X-ray powder diffraction patterns of the synthesized MOFs and their polymer-tethered analogs compared with simulated patterns (sim.) obtained from the previously reported single-crystal data.

12. Nitrogen adsorption measurements

Nitrogen adsorption measurements were conducted using a Yuasa Ionics Autosorb 6AG at -196°C . Prior to the measurement, the MOF particles were thoroughly activated at 100°C under high vacuum for 12 h. The PSD was calculated from the fitted N_2 adsorption isotherms using slit-cylindrical pores and QSDFT equilibrium model. Log-normal distribution was fitted to the PSD results, and the mean pore size (r_p^*) and pore size standard deviation (σ_p^*) were later used in nanofiltration modeling.

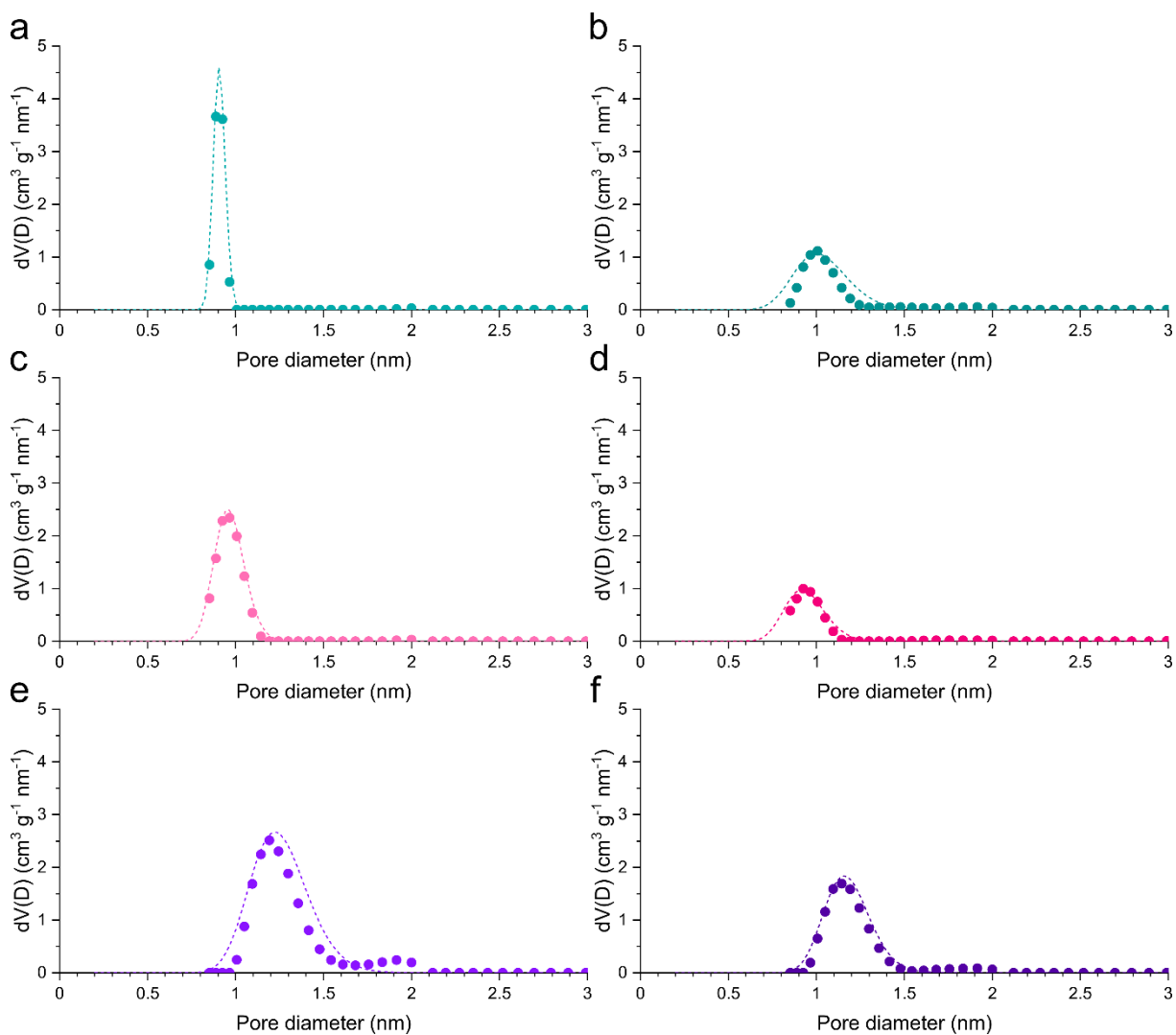


Fig. S34. Pore size distribution data of a) UiO-66-NH₂, b) UiO-66-PNIPAM, c) UiO-67-NH₂, d) UiO-67-PNIPAM, e) UiO-68-NH₂, and f) UiO-68-PNIPAM represented with symbols determined by fitting slit-cylindrical pores in the QSDFT equilibrium model using experimental N_2 adsorption isotherms. The dashed lines show log-normal distributions fitted over the datapoints.

13. Scanning electron microscopy

A Nova Nano scanning electron microscope was used to record electron images of selected samples using TLD and ETD detectors at 5-mm working distance, 5-keV voltage, and 56-pA current at various magnifications. Prior to the measurement, the samples were placed on an aluminum sample holder. Then, the prepared samples were coated with 4 nm of platinum using a sputter coating machine.

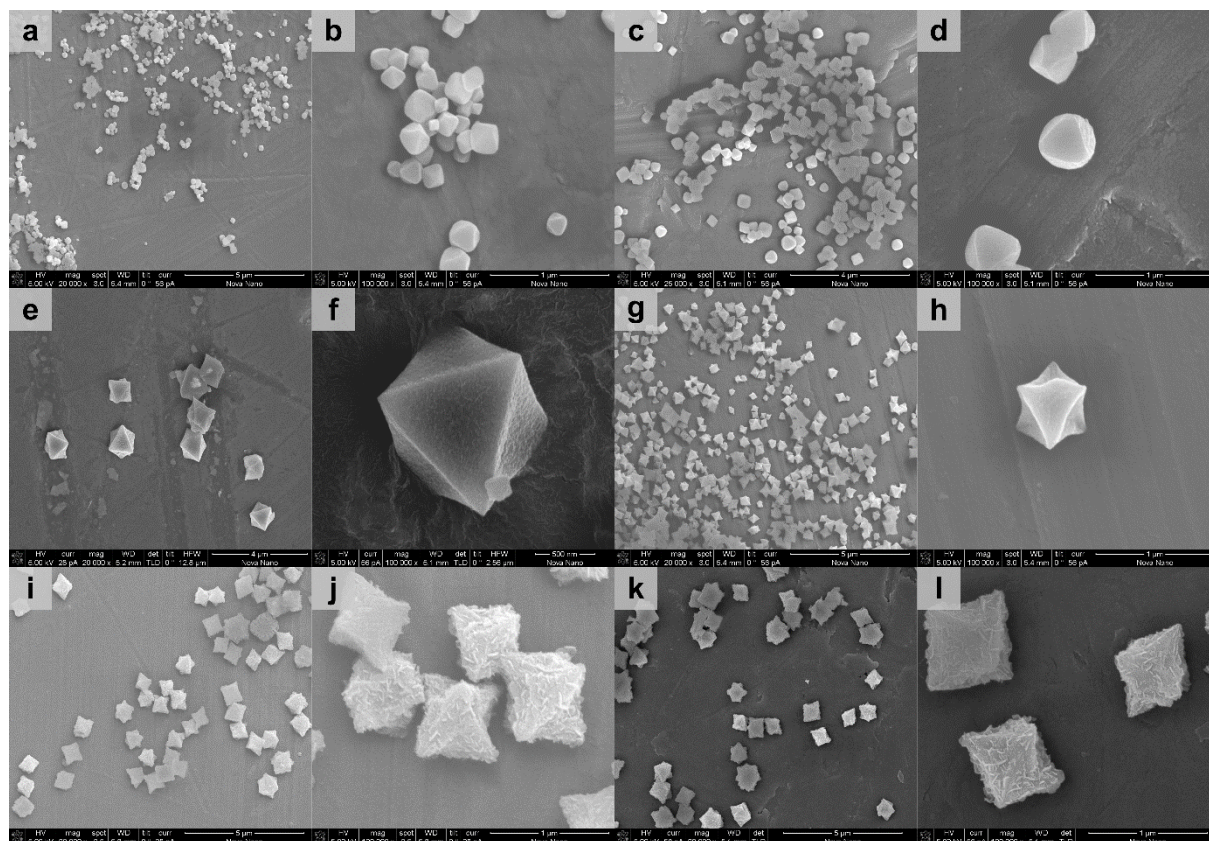


Fig. S35. SEM images of a–b) UiO-66-NH₂, c–d) UiO-66-PNIPAM, e–f) UiO-67-NH₂, g–h) UiO-67-PNIPAM, i–j) UiO-68-NH₂, and k–l) UiO-68-PNIPAM at low (a, c, e, g, i, and k) and high (b, d, f, h, j, and l) magnification.

Particle size analysis was performed based on the low magnification images of MOFs using the ImageJ software. This method can only provide information on the magnitude of the particle size. It is not very accurate because the particles in the frame of the analysis are not necessarily representative of the total population. Overlapping particles, artefacts, and insufficient contrast may also distort the results. Nevertheless, the magnitude of particle size obtained from SEM was in line with the DLS results.

Table S4. Particle size analysis of MOFs based on SEM images.

| | UiO-66-NH ₂ | UiO-66-PNIPAM | UiO-67-NH ₂ | UiO-67-PNIPAM | UiO-68-NH ₂ | UiO-68-PNIPAM |
|-------------------------------------|------------------------|---------------|------------------------|---------------|------------------------|---------------|
| Number of particles in the analysis | 207 | 143 | 81 | 219 | 202 | 116 |
| Particle diameter (nm) | 214.4 ± 97 | 337.4 ± 93 | 1096.5 ± 375 | 337.2 ± 97 | 849.5 ± 165 | 832.8 ± 117 |

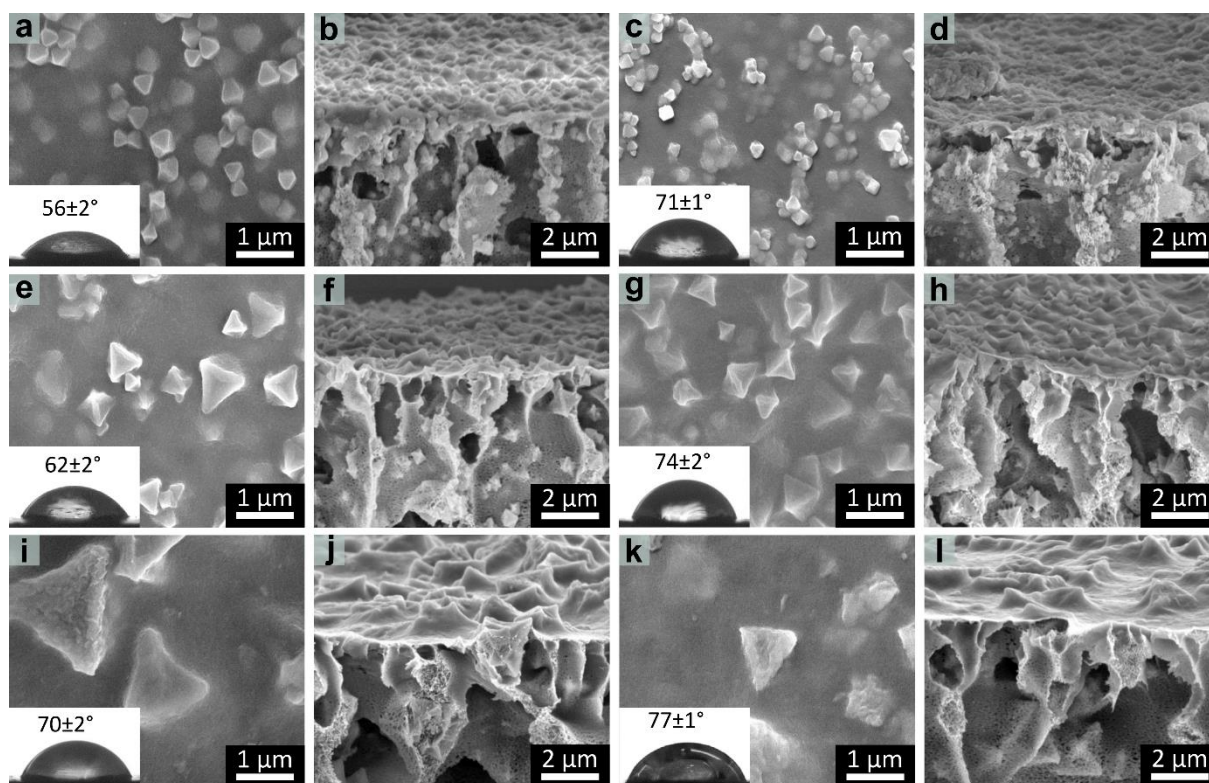


Fig. S36. Surface and cross-section SEM images of M66^N (a, b), M66^P (c, d), M67^N (e, f), M67^P (g, h), M68^N (i, j), and M68^P (k, l). The insets show the digital camera images of the water contact angles.

The MOF particles were homogeneously distributed across the surface and cross-section of the membrane. The cross-section images show MOF nanoparticles extending over the polymer surface. The membrane hydrophobicity increased from M66^N to M68^N (inset of a, e, i) owing to the longer aromatic linkers in their fillers that induce a more hydrophobic character. The contact angles of M66^P, M67^P, and M68^P were lower than those of their unmodified counterparts, which confirms the presence of hydrophilic PNIPAM chains on their surface.

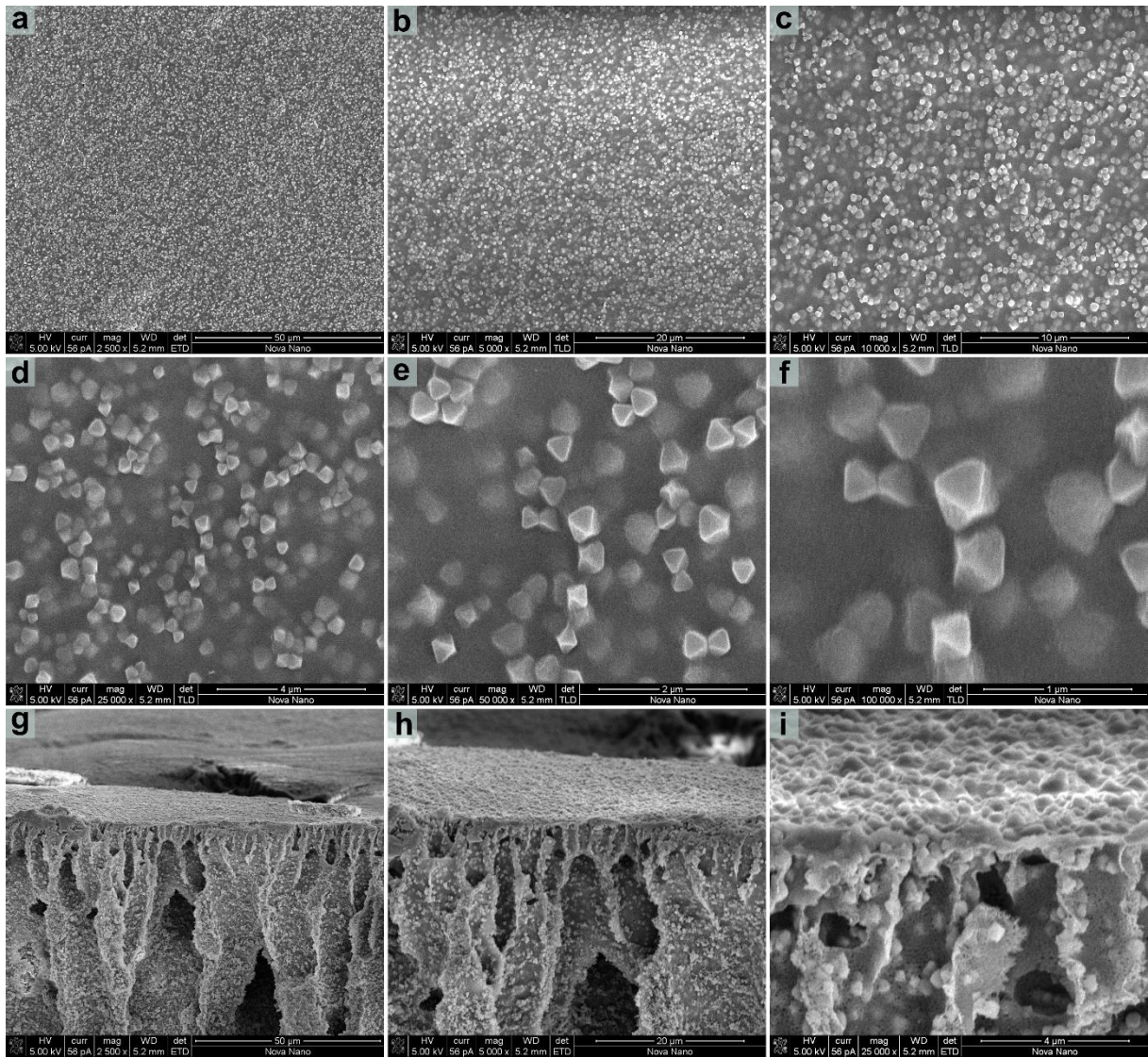


Fig. S37. SEM top-section (a–f) and cross-section (g–i) images of M66^N at various magnifications.

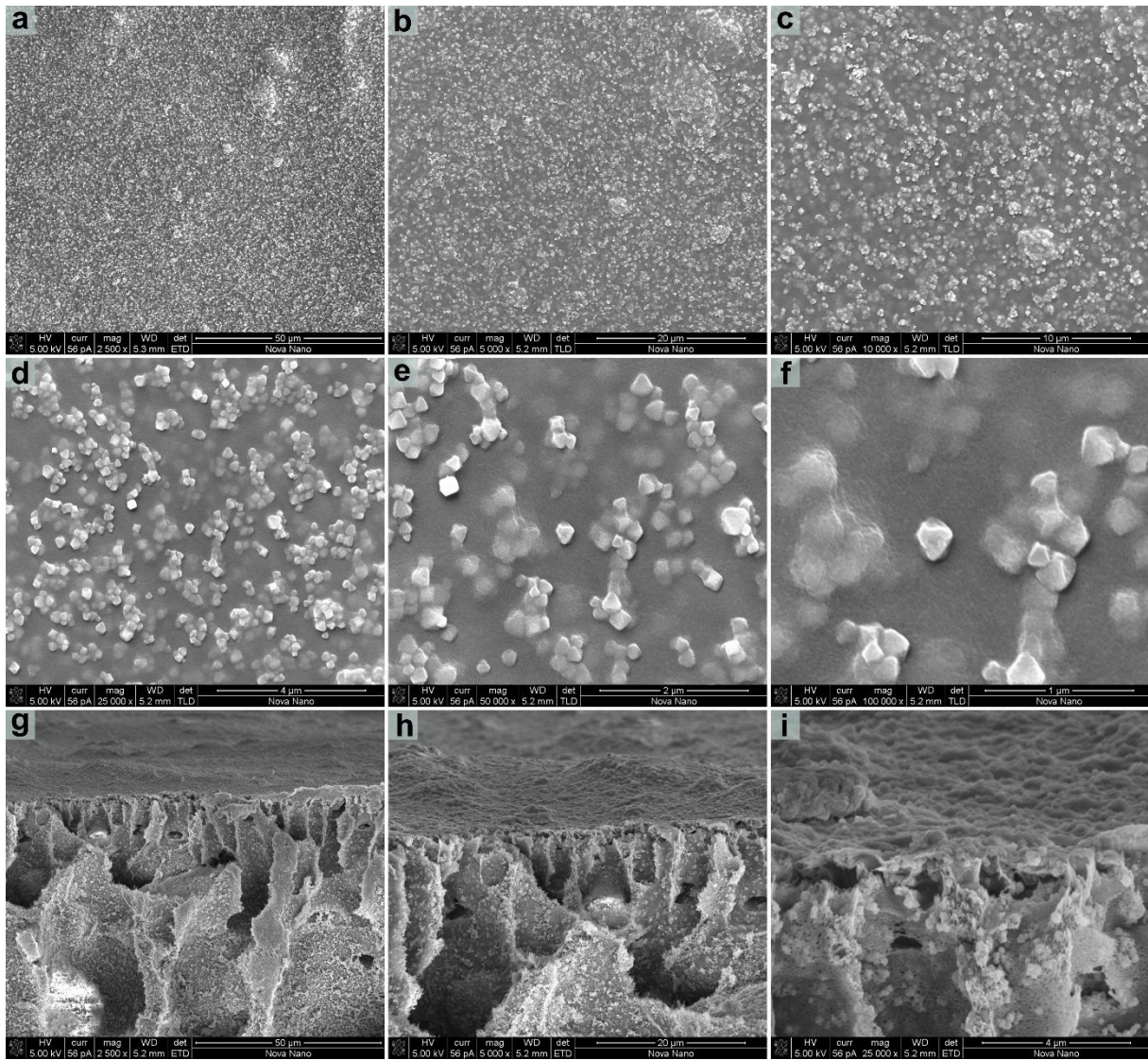


Fig. S38. SEM top-section (a–f) and cross-section (g–i) images of M66^P at various magnifications.

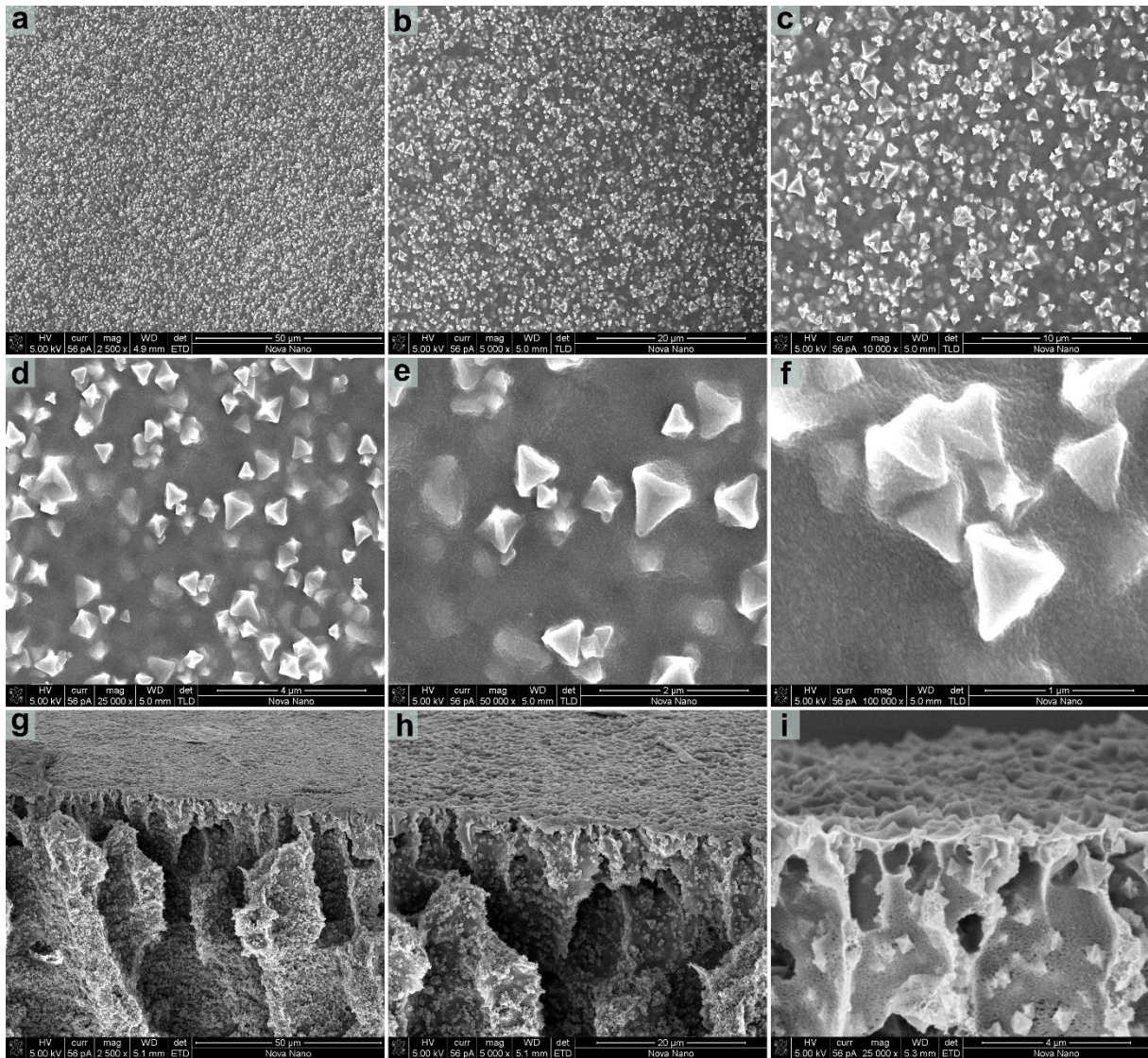


Fig. S39. SEM top-section (a–f) and cross-section (g–i) images of M67^N at various magnifications.

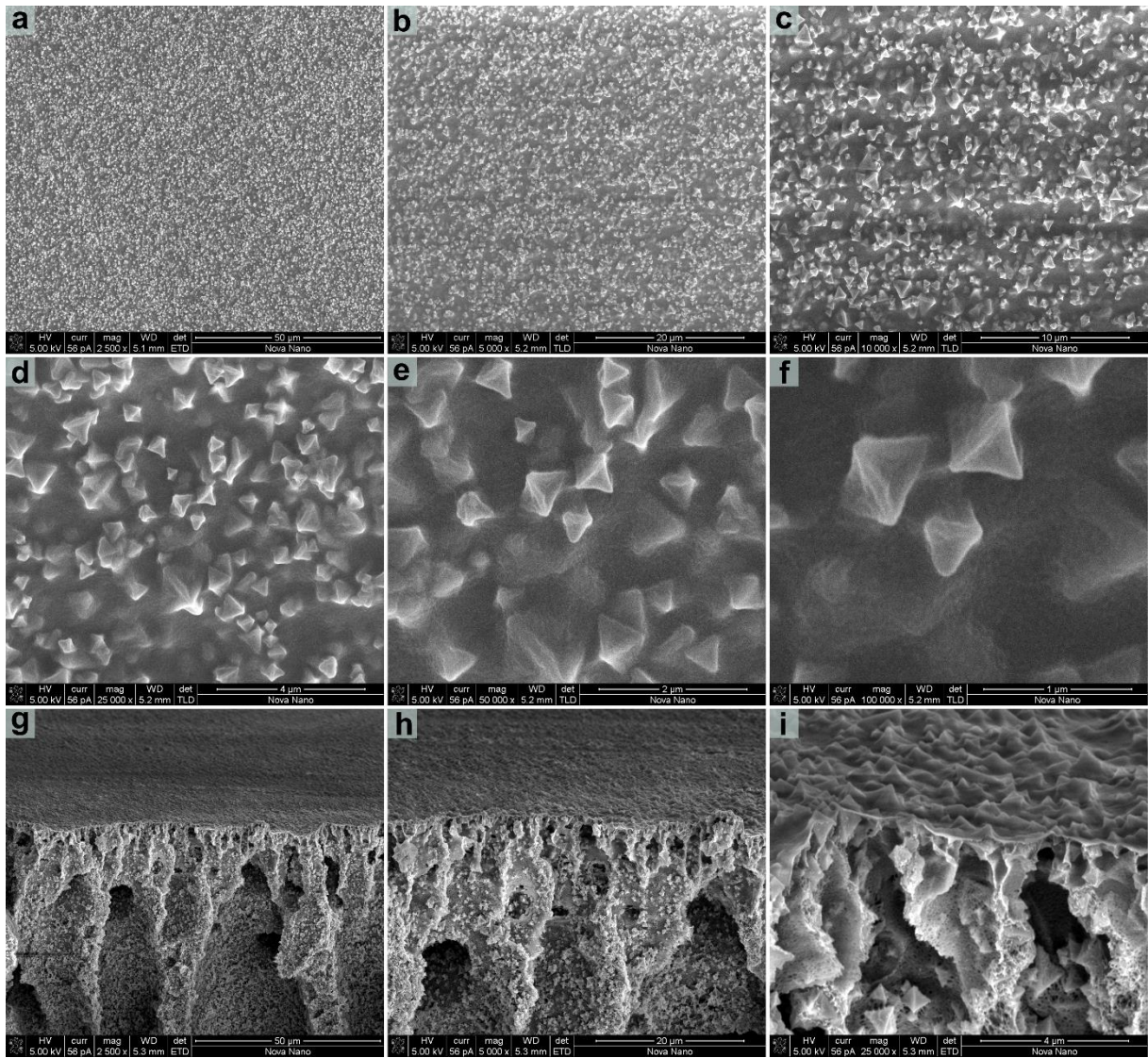


Fig. S40. SEM top-section (a–f) and cross-section (g–i) images of M67^P at various magnifications.

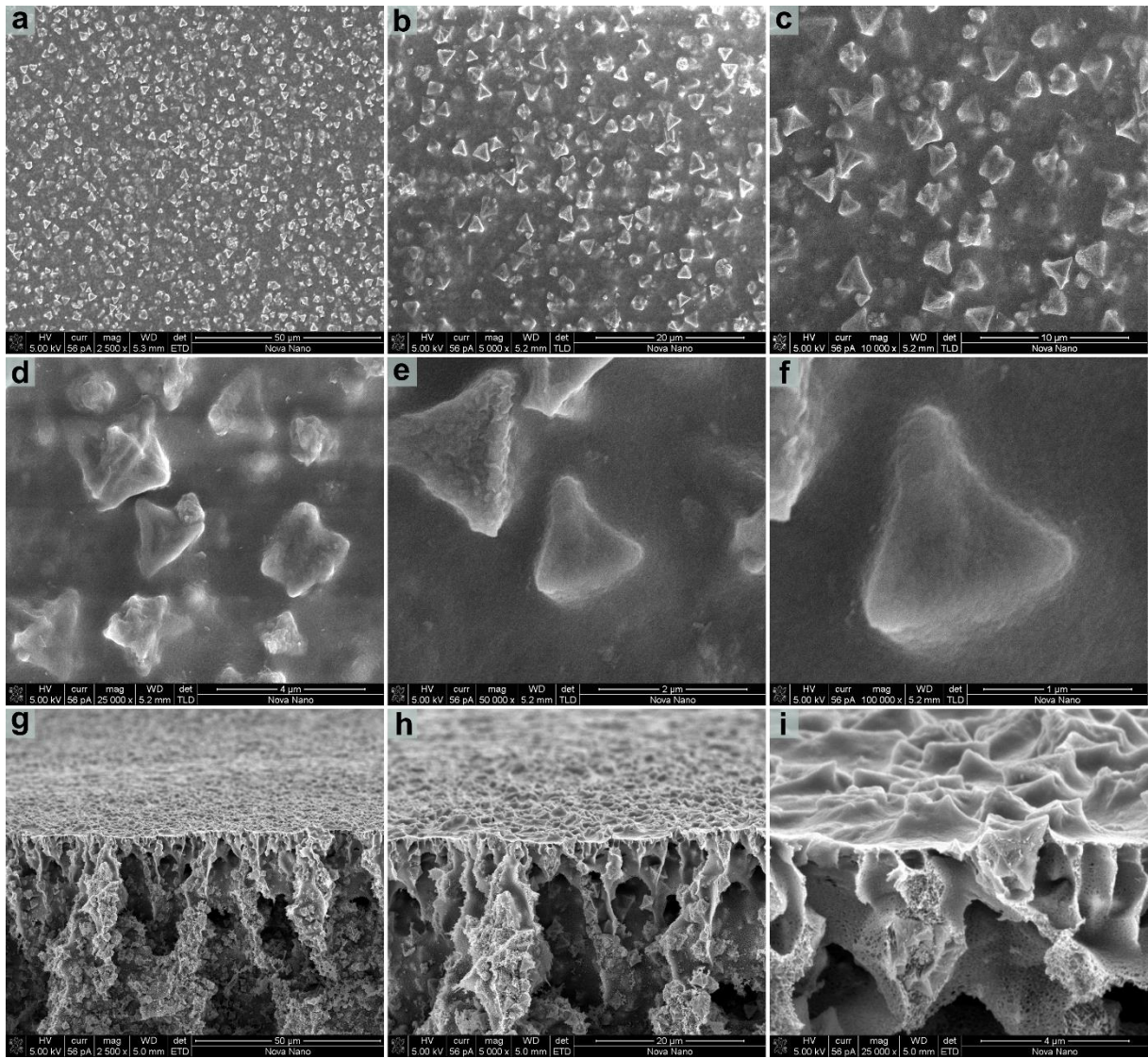


Fig. S41. SEM top-section (a–f) and cross-section (g–i) images of M68^N at various magnifications.

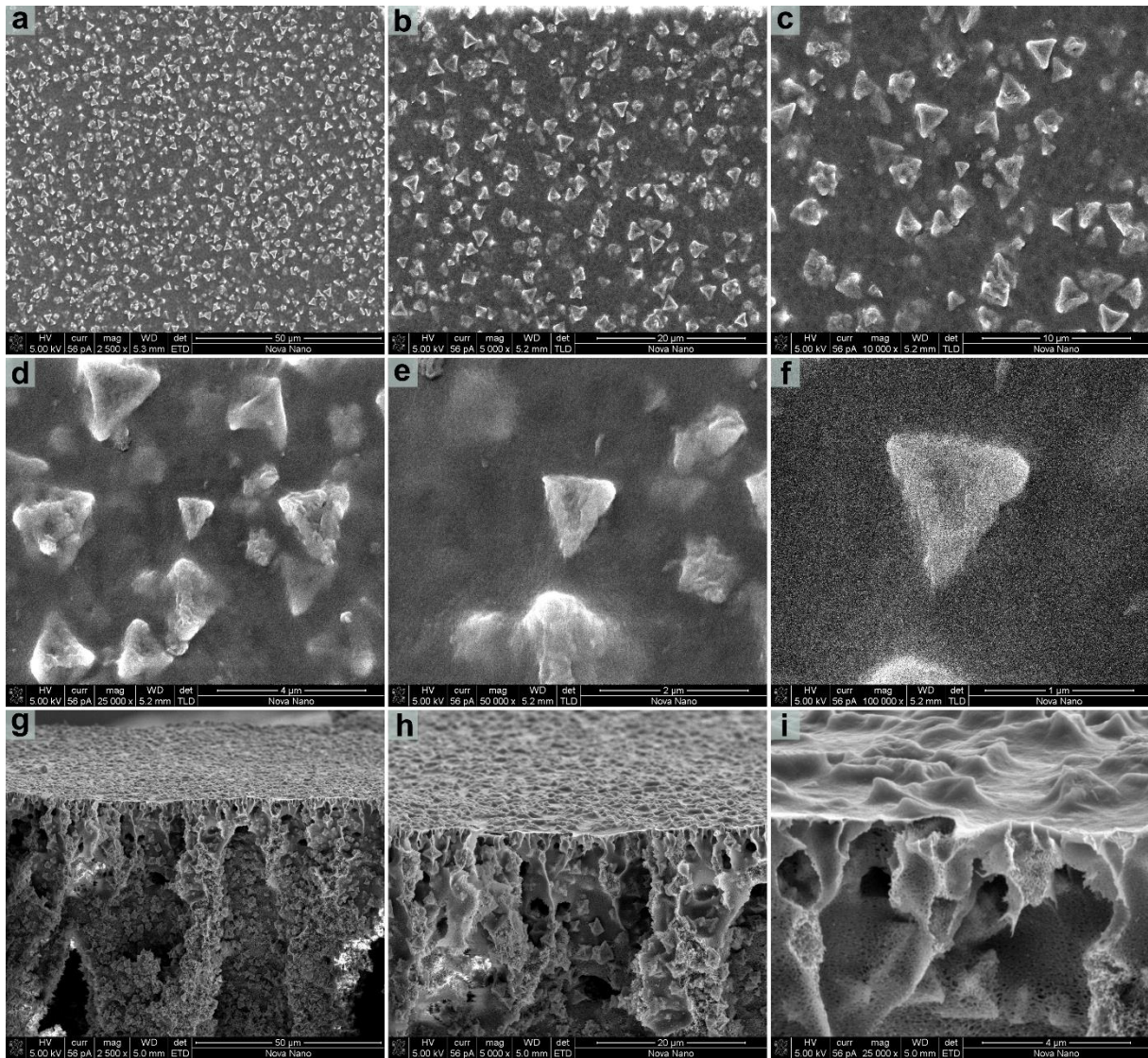


Fig. S42. SEM top-section (a–f) and cross-section (g–i) images of M68^P at various magnifications.

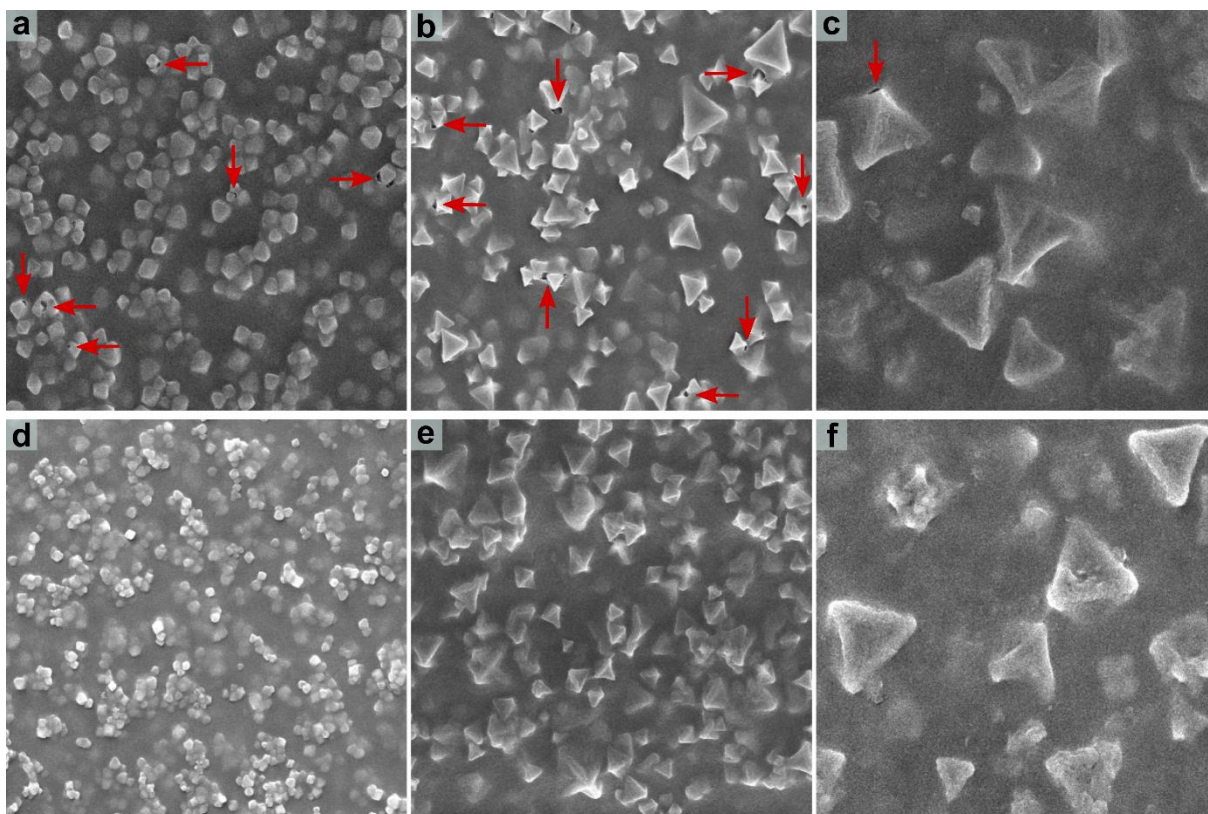


Fig. S43. Interfacial defects (indicated by red arrows) around the MOF filler particles in the a) M66^N, b) M67^N, and c) M68^N membranes. In contrast, no defects were observed in the d) M66^P, e) M67^P, and f) M68^P membranes. All images are 10 μm × 10 μm in size.

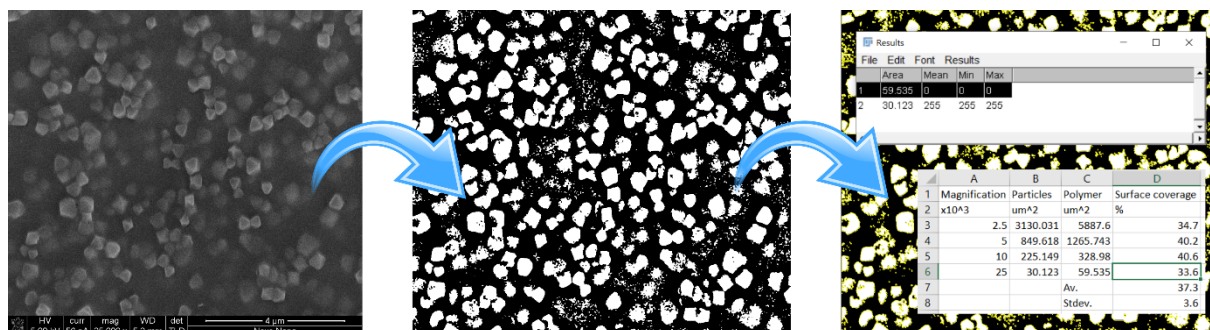


Fig. S44. Illustration of the image-processing steps used to extract MOF coverage data from SEM images based on the example of the M66^N membrane.

Table S5. MOF surface coverage data of different membranes obtained from the analysis of SEM images. Averages and standard deviations were calculated based on the data obtained at four different magnifications (2.5k, 5k, 10k, and 25k).

| Membrane | MOF coverage (%) | MOF coverage std. dev. (%) |
|------------------|------------------|----------------------------|
| M66 ^N | 37.3 | 3.6 |
| M67 ^N | 41.7 | 5.2 |
| M68 ^N | 40.4 | 6.4 |
| M66 ^P | 40.2 | 1.8 |
| M67 ^P | 42.4 | 1.7 |
| M68 ^P | 38.2 | 3.9 |

14. Thermal analysis

Simultaneous differential scanning calorimetry and thermogravimetric analysis (DSC-TGA) was performed using a STA 449 F1 Jupiter instrument (NETZSCH-Gerätebau GmbH) at the temperature ramp rate of $10^{\circ}\text{C}\cdot\text{min}^{-1}$ from 25°C to 700°C under pure oxygen atmosphere.

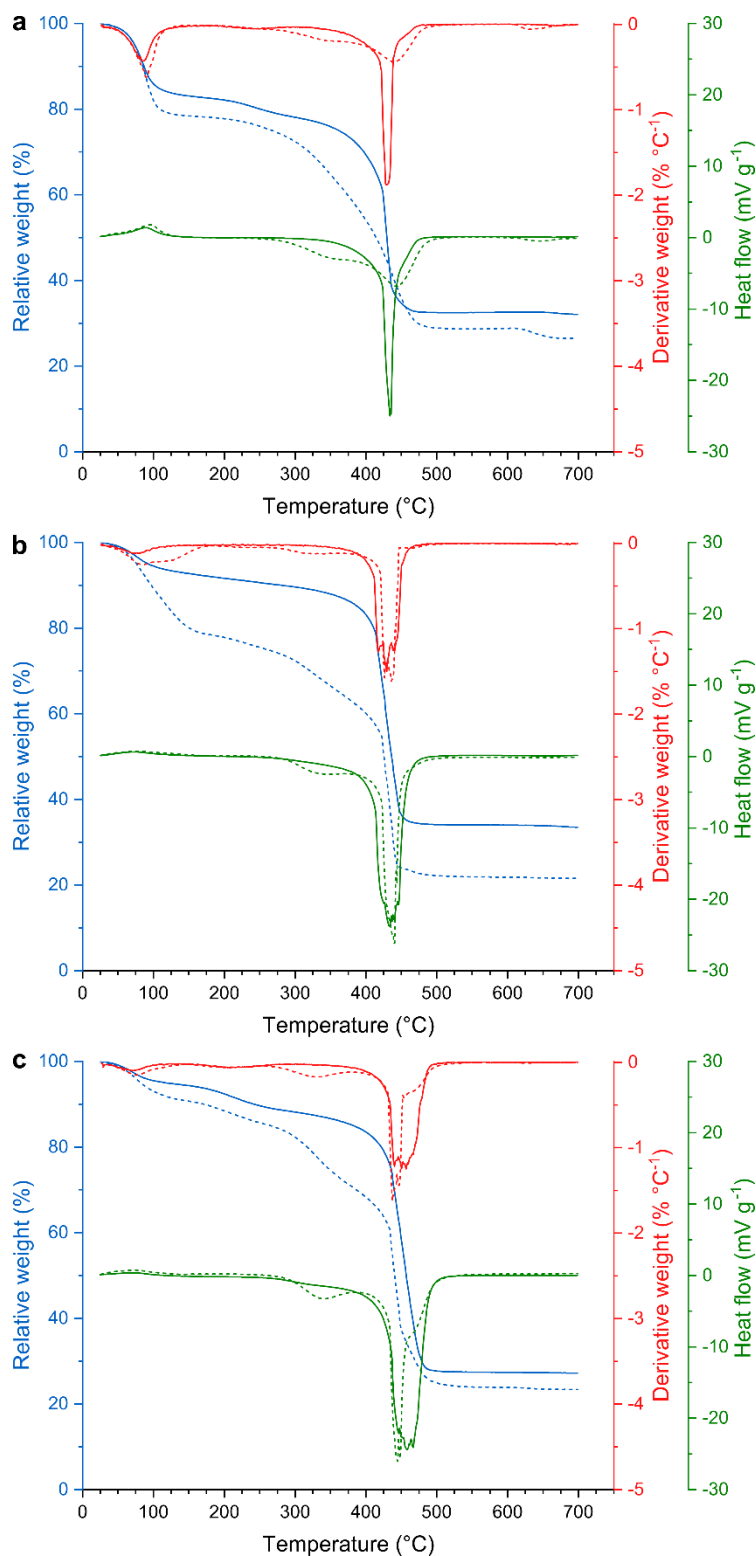


Fig. S45. Simultaneous differential scanning calorimetry and thermogravimetric analysis (DSC-TGA) of a) UiO-66-, b) UiO-67-, and c) UiO-68-based MOFs under oxygen atmosphere. The solid lines belong to the parent MOF-NH₂, and the dashed lines belong to the PNIPAM-modified MOFs (MOF-PNIPAM).

The PNIPAM content of the modified MOFs can be calculated from the TGA data. The samples are regarded to be solvent free without any PNIPAM or linker degradation at 150°C. At 600°C, complete oxidation to ZrO₂ is assumed. Therefore, the PNIPAM content (x_{PNIPAM}) of PNIPAM-grafted MOFs can be calculated as

$$x_{\text{PNIPAM}} = \left(1 - \frac{x_{\text{MOF-PNIPAM},600} \cdot x_{\text{MOF-NH}_2,150}}{x_{\text{MOF-PNIPAM},150} \cdot x_{\text{MOF-NH}_2,600}} \right) \cdot 100\% \quad (\text{S3})$$

where $x_{\text{MOF-PNIPAM},600}$, $x_{\text{MOF-NH}_2,150}$, $x_{\text{MOF-PNIPAM},150}$, and $x_{\text{MOF-NH}_2,600}$ are the residual weights of the PNIPAM-grafted MOF at 600°C, the ungrafted MOF at 150°C, the PNIPAM-grafted MOF at 150°C, and the ungrafted MOF at 600°C, respectively.

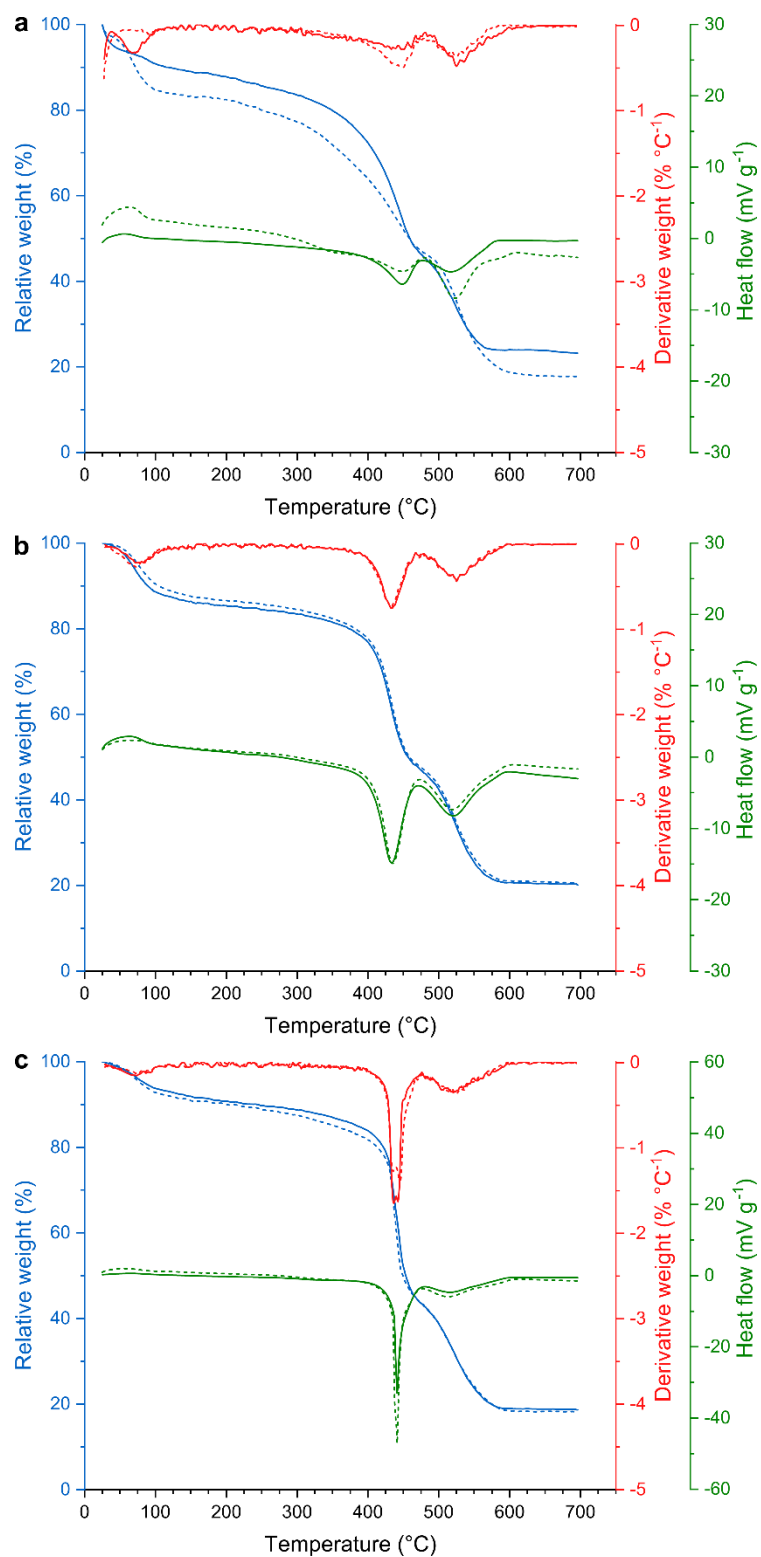


Fig. S46. Simultaneous differential scanning calorimetry and thermogravimetric analysis (DSC-TGA) of a) M66^N and M66^P, b) M67^N and M67^P, and c) M68^N and M68^P membranes under oxygen atmosphere. The solid lines belong to the membranes with an unmodified MOF filler (*^N), and the dashed lines belong to the membranes with a PNIPAM-modified MOF filler (*^P). For all membranes, an initial water desorption step can be observed below 100 °C. MOF filler degradation occurs at 400 °C–475 °C followed by PBI oxidation at 475 °C–600 °C, which leaves behind only ZrO₂ residue.

15. Polymer solubility

Solvent selection for membrane casting was performed based on three considerations: i) the solvent should be able to dissolve PBI at high concentrations (>20 wt%) to enable film formation, ii) the solvent should be able to dissolve PNIPAM to allow intertwining of polymer chains at the MOF surface, and iii) the polymer should promote (or at least not hinder) PBI–PNIPAM intermolecular interactions to minimize the formation of interfacial gaps.

Small-scale solubility testing of PBI in nine polar aprotic solvents was performed as follows. 50 mg (10 wt%) of PBI powder was added to 450 mg of the solvent. The mixture was heated to 150°C while shaking intermittently and was cooled to room temperature. Solubility testing of PNIPAM was performed using a similar approach. 50 mg (10 wt%) of PBI powder was added to 200 mg of the solvent. The mixture was heated to 40°C while shaking intermittently and cooled to room temperature. The results are summarized in Table S6.

Table S6 Experimental solubilities of PBI (10 wt%) and PNIPAM (20 wt%) in nine conventional and emerging polar aprotic solvents.

| Polymer | Solvent | | | | | | | | |
|---------|---------|------|----------------|-----|----------------|----------------|-----|----------------|--------|
| | DMSO | DMAc | DMF | NMP | Sulfolane | PC | GVL | PolarClean | Cyrene |
| PBI | + | + | P ^a | + | - | - | - | P ^a | - |
| PNIPAM | + | + | + | + | G ^b | G ^b | + | + | + |

^aPartially soluble; ^bGelation

The DMAc, DMSO, and DMF solubilities of PBI are in agreement with those reported in the literature.⁹ Overall, the solubility results narrow down the solvent selection to DMSO, DMAc, and NMP; only these solvents can dissolve both PNIPAM and PBI at the concentration suitable for membrane fabrication. Among these, DMAc was selected based on the computational results.

16. Membrane fabrication

The MMMs were prepared from a dope solution obtained by mixing a MOF suspension with a PBI polymer solution to minimize the formation of aggregates. In a typical procedure, a suspension of MOF particles (300 mg) in DMAc (623 mg) and PBI dope solution (577 mg; 26 wt% in DMAc) were blended under inert atmosphere. The blend was stirred for 6 h to obtain a homogeneous solution. Bubbles were removed via incubation prior to casting. The final mass ratio of polymer to MOF in the dope solution was 1:2 (Table S7). The dope solution was cast onto a nonwoven polypropylene support using an Elcometer 4340 film applicator with a casting thickness of 250 μm and casting speed of 8 cm s^{-1} . The cast film was immediately immersed in a coagulation bath at 23°C to form the membrane. The coagulation bath was replaced after 30 min, and the membrane was kept in the bath until use. All membranes were prepared using different MOF fillers. The membrane notations are summarized in Table S8.

Table S7. Amount of PBI, MOF, and solvent in the mixed-matrix membrane casting solutions.

| Added mass (mg) | | | Total mass (mg) | Dope solution composition (wt%) | | | Dry composition (wt%) | |
|-----------------|-----|------|-----------------|---------------------------------|-----|------|-----------------------|-----|
| PBI 26 wt% | MOF | DMAc | | PBI | MOF | DMAc | PBI | MOF |
| 577 | 300 | 623 | 1500 | 10 | 20 | 70 | 33 | 67 |

Table S8. Mixed-matrix membrane notations and their corresponding MOF filler materials.

| Membrane | MOF filler |
|------------------|------------------------|
| M66 ^N | UiO-66-NH ₂ |
| M67 ^N | UiO-67-NH ₂ |
| M68 ^N | UiO-68-NH ₂ |
| M66 ^P | UiO-66-PNIPAM |
| M67 ^P | UiO-67-PNIPAM |
| M68 ^P | UiO-68-PNIPAM |

17. Atomic force microscopy

Atomic force microscopy (AFM; Bruker Dimension ICON) was employed to analyze the membrane surfaces. The measurements were performed in tapping mode (Acoustic AC) at room temperature. For each membrane, an area of $5 \times 5 \mu\text{m}^2$ was scanned at the rate of 1 Hz and 256 samples/line. The obtained results were processed using the NanoScope Analysis (v. 1.5) software to obtain the mean roughness (R_a), height images, and 3D projections.

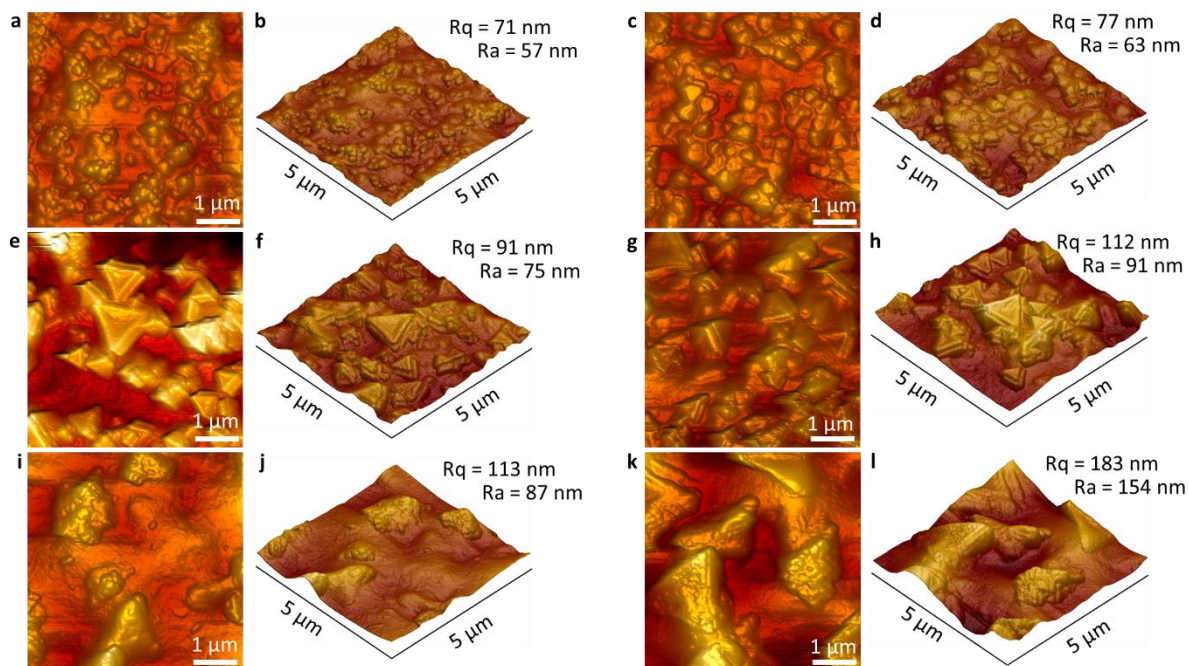


Fig. S47. AFM height images and 3D projections of M66^N (a, b), M66^P (c, d), M67^N (e, f), M67^P (g, h), M68^N (i, j), and M68^P (k, l).

18. Water contact angle measurements

A Kruss EasyDrop equipment was used to measure the water contact angle of the MMMs, employing a sessile drop method and Young–Laplace model. The membranes were attached to a glass plate using double-sided tape, and four measurements were performed at different locations on the membrane to obtain the average contact angle value for each sample. In each case, a drop volume of 2 μL was applied and the contact angle reading was made after 5 s.

The results are shown in Fig. S35 alongside the SEM images of the membranes.

19. Computational methods

All density functional computations were performed with the M06-2X functional (which is suitable for calculation of noncovalent interactions) and 6-31+G** basis set using the Gaussian 09 package.¹⁰ The interaction energy of bimolecular systems was calculated as

$$E_{\text{int}} = E_{\text{molecule1+2}} - (E_{\text{molecule1}} + E_{\text{molecule2}}) \quad (\text{S4})$$

where $E_{\text{molecule1+2}}$, $E_{\text{molecule1}}$, and $E_{\text{molecule2}}$ are the total energy of the complex and two separate molecules, respectively.

The interaction energy of ternary (polymer–polymer–solvent) systems was calculated as

$$E_{\text{int}} = E_{\text{polymer1+2+solvent}} - (E_{\text{polymer1+2}} + E_{\text{solvent}}) \quad (\text{S5})$$

where $E_{\text{polymer1+2+solvent}}$, $E_{\text{polymer1+2}}$, and E_{solvent} are the total energies of the ternary complex, bimolecular polymer complex, and solvent, respectively.

Molecular dynamics simulations of the polymer–solvent mixtures at 298 K were performed using Material Studio (version 8.0). The COMPASS force field was employed to assign charge and force field parameters. The Forcite module was used with isothermal–isobaric and isothermal–isopycnic ensembles for equilibration runs of 500 ps and production runs of 5000 ps, respectively. The time step was set to 1 fs. The Andersen and Berendsen methods were adapted for temperature and pressure control, respectively. Long-range Coulomb interactions were accounted for by the Ewald sum method; and nonbonded energy was calculated with a cut-off distance of 12 Å. The PNIPAM coverage was calculated by counting the average occupied apertures over the run with respect to the total number of apertures.

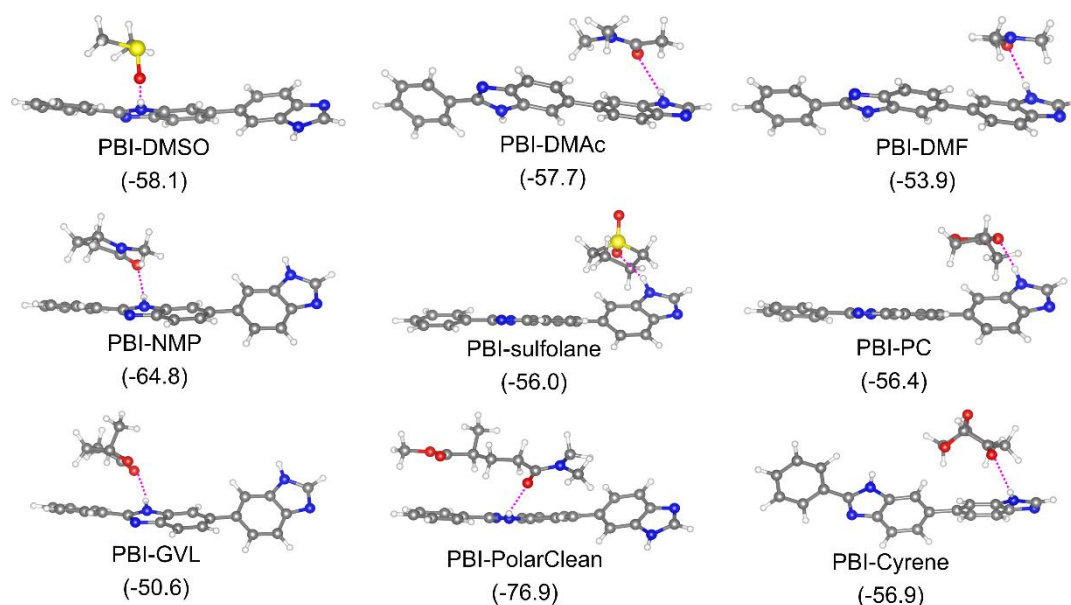


Fig. S48. Optimized structures of PBI–solvent complexes and interaction energies (in $\text{kJ}\cdot\text{mol}^{-1}$).

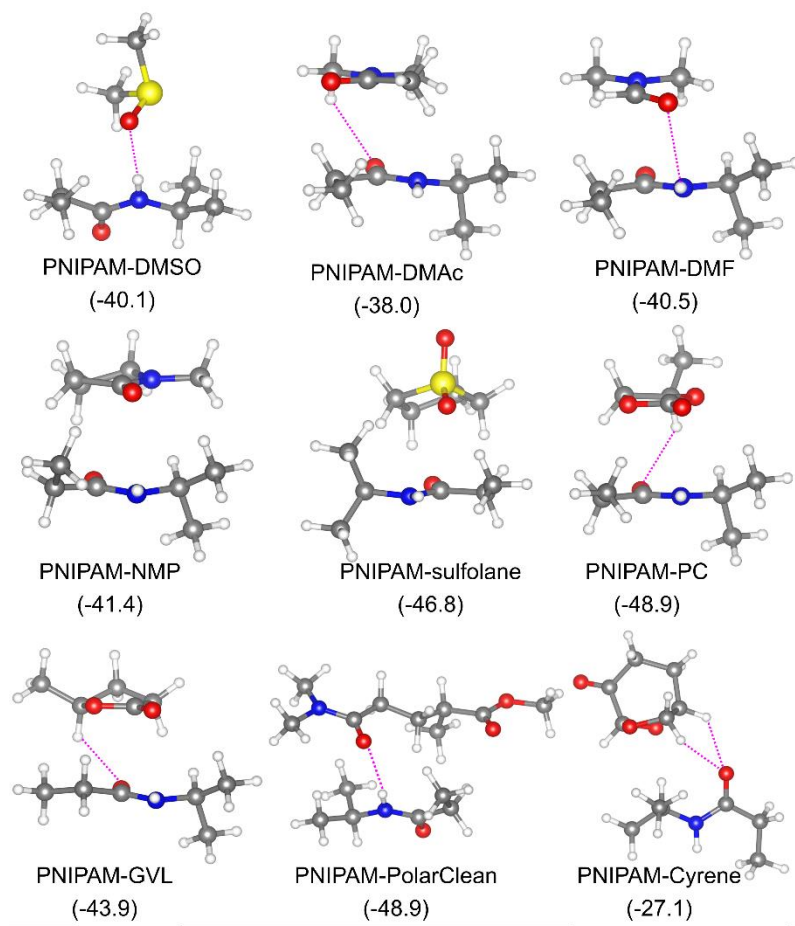


Fig. S49. Optimized structures of PNIPAM-solvent complexes and interaction energies (in $\text{kJ}\cdot\text{mol}^{-1}$).

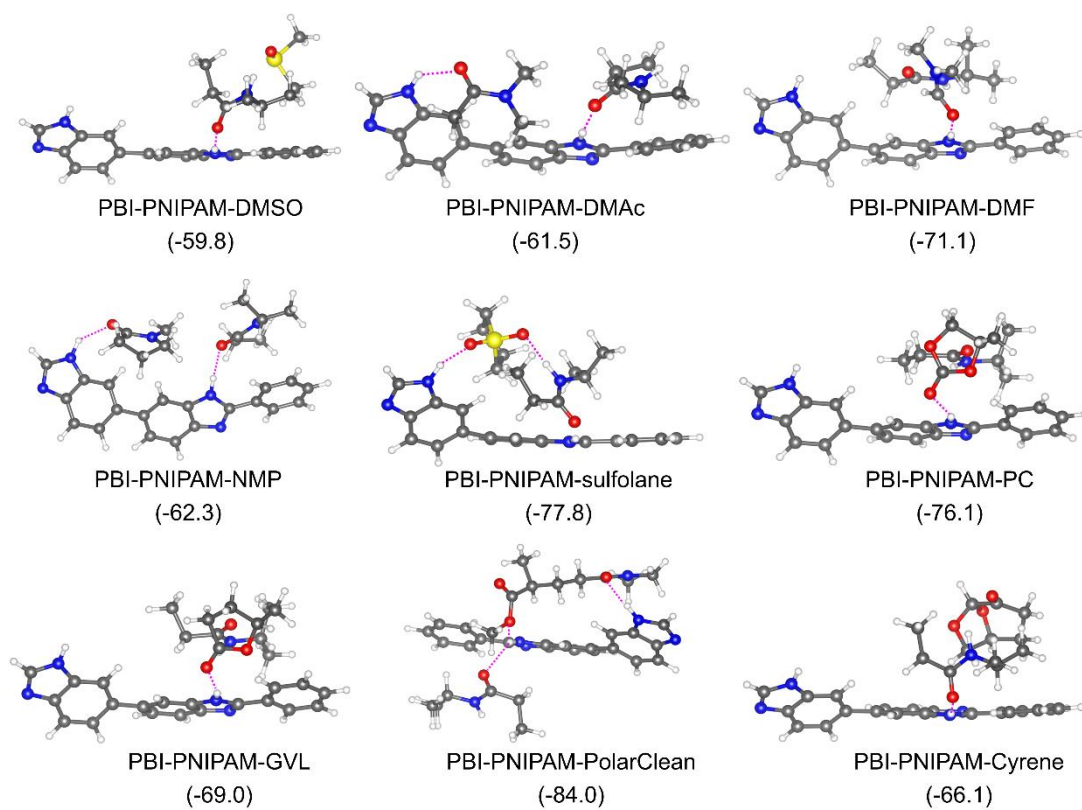


Fig. S50. Optimized structures of PBI-PNIPAM-solvent complexes and interaction energies (in $\text{kJ}\cdot\text{mol}^{-1}$).

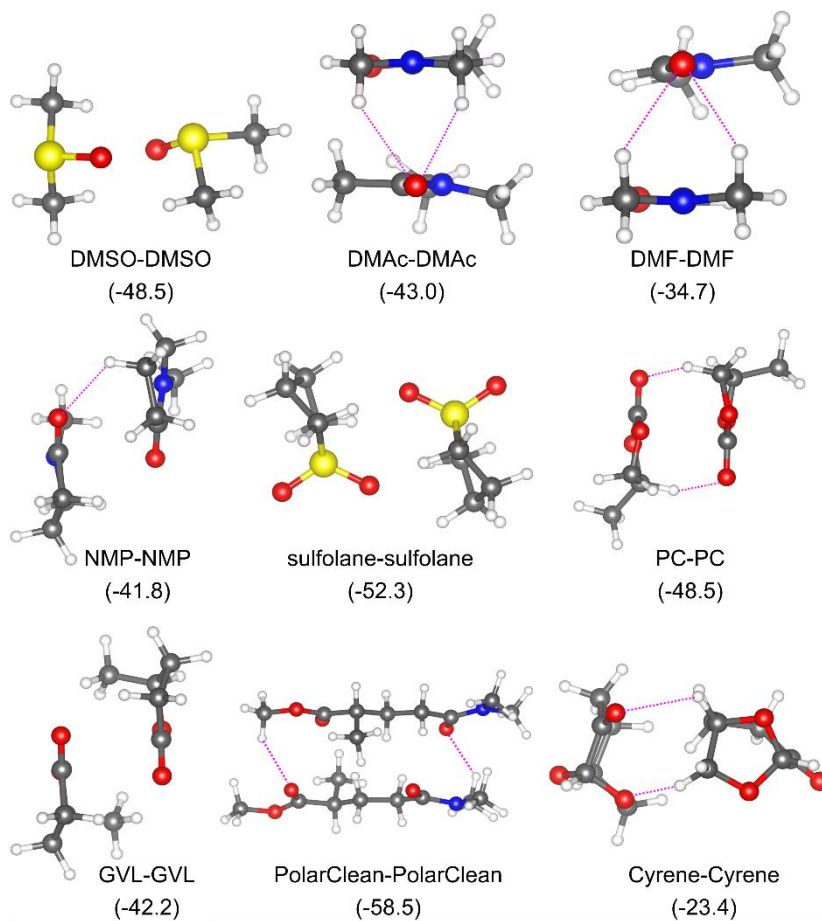


Fig. S51. Optimized structures of solvent-solvent complexes and interaction energies in (kJ·mol⁻¹).

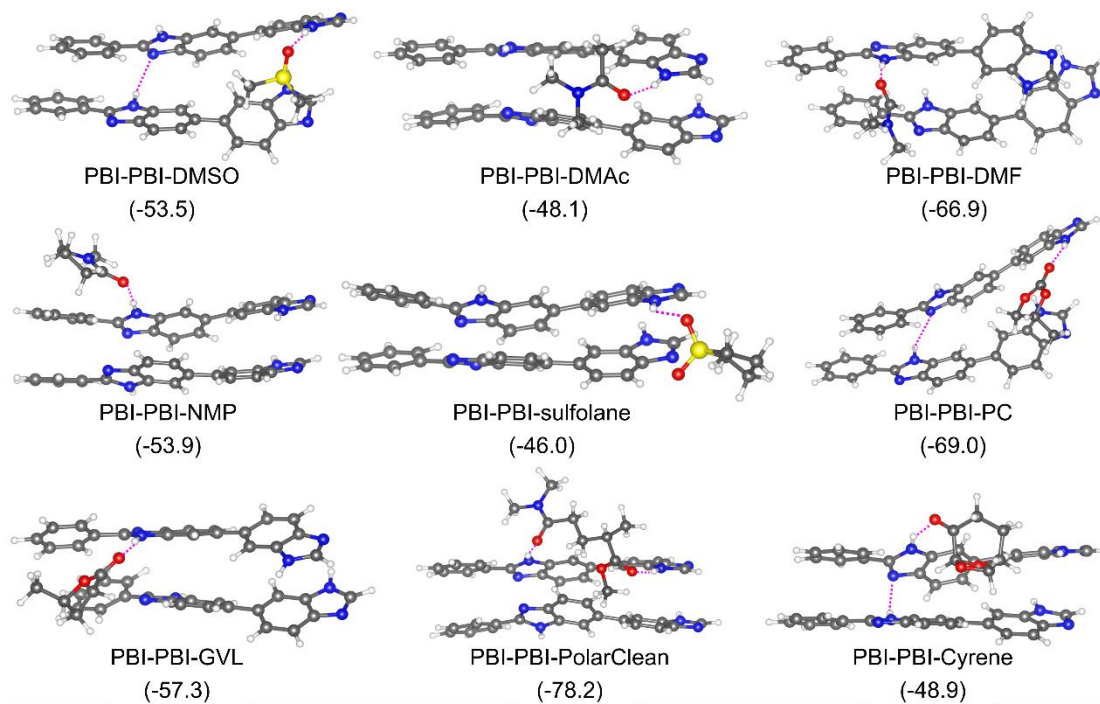


Fig. S52. Optimized structures of PBI-PBI-solvent complexes and interaction energies in (kJ·mol⁻¹).

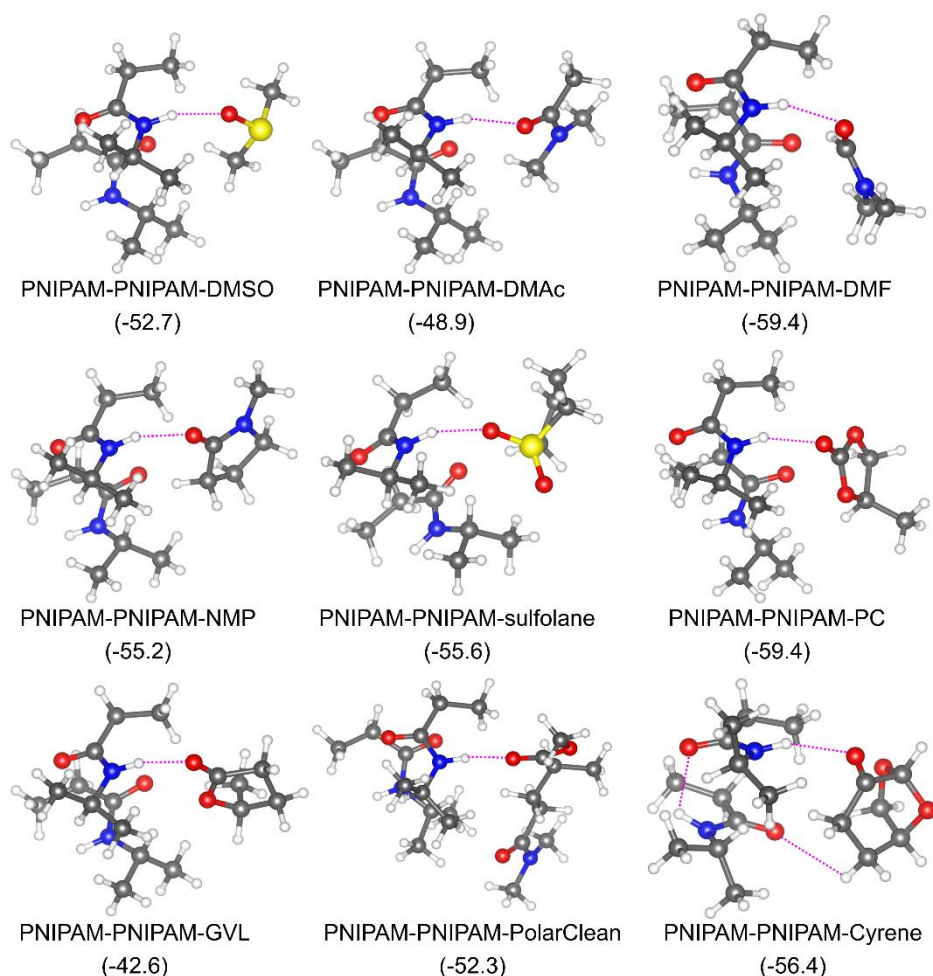


Fig. S53. Optimized structures of PNIPAM–PNIPAM–solvent complexes and interaction energies (in $\text{kJ}\cdot\text{mol}^{-1}$).

Table S9. Binding energies of different binary or ternary complexes with polar aprotic solvents.

| Solvents | Binding energy ($\text{kJ}\cdot\text{mol}^{-1}$) | | | | | |
|-------------------------|--|--------------|---------------------------|--------------|------------------------|------------------------|
| | PBI–* | PNIPAM–* | PBI-PNIPAM–* ^a | Solvent–* | PBI-PBI–* ^b | PNI-PNI–* ^c |
| Cyrene | -56.9 | -27.2 | -66.1 | -23.4 | -49.0 | -56.5 |
| DMAc^d | -57.7 | -38.1 | -61.5 | -43.1 | -48.1 | -49.0 |
| DMF | -54.0 | -0.6 | -71.1 | -34.7 | -66.9 | -59.4 |
| DMSO^d | -58.2 | -40.2 | -59.8 | -48.5 | -53.6 | -52.7 |
| GVL | -50.6 | 43.9 | -69.0 | -42.3 | -57.3 | -42.7 |
| NMP^d | -64.9 | -41.4 | -62.3 | -41.8 | -54.0 | -55.2 |
| PC | -56.5 | -49.0 | -76.1 | -48.5 | -69.0 | -59.4 |
| PolarClean | -77.0 | -49.0 | -84.1 | -58.6 | -78.2 | -52.3 |
| Sulfolane | -56.1 | -46.9 | -77.8 | -52.3 | -46.4 | -55.6 |

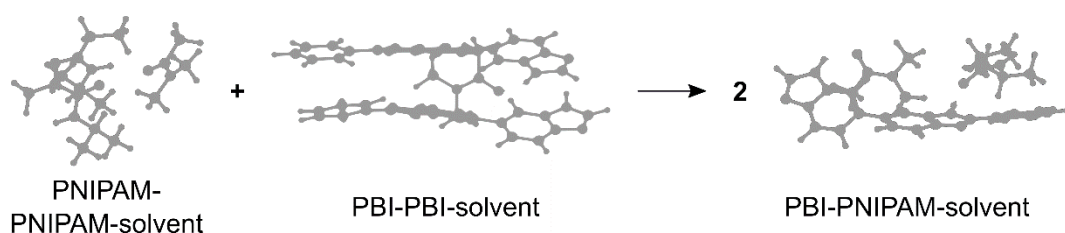
^a $E_{\text{PBI-PNIPAM}}$: $-90.4 \text{ kJ}\cdot\text{mol}^{-1}$. ^b $E_{\text{PBI-PBI}}$: $-51.0 \text{ kJ}\cdot\text{mol}^{-1}$. ^c $E_{\text{PNI-PNI}}$: $-39.7 \text{ kJ}\cdot\text{mol}^{-1}$. ^dSolvents that performed sufficiently well in solubility tests to be considered for membrane fabrication were DMAc, DMSO, and NMP.

The solvent selection was made on the basis of the polymer heterocomplexation energies ($E_{\text{net.comp.}}$) in three suitable solvents (DMAc, DMSO, and NMP) calculated using (S6).

$$E_{\text{het.comp.}} = 2 * E_{\text{PBI-PNIPAM-solvent}} - (E_{\text{PBI-PBI-solvent}} + E_{\text{PNIPAM-PNIPAM-solvent}}) \quad (\text{S6})$$

The lower the value of $E_{\text{het.comp.}}$ in a certain solvent, the more favorable is the interaction between PBI and PNIPAM chains. Therefore, low $E_{\text{het.comp.}}$ can be associated with highly intertwined polymer chains in the interfacial region between the PBI matrix and MOF-PNIPAM filler, which results in a dense and defect-free interface.

Table S10. Ternary polymer–polymer–solvent interaction energies and heterocomplexation energies in solvents with sufficient solvency for PBI for membrane fabrication via solution casting.



| Solvent | $E_{\text{PBI-PNIPAM-solvent}}$ (kJ·mol ⁻¹) | $E_{\text{PBI-PBI-solvent}}$ (kJ·mol ⁻¹) | $E_{\text{PNIPAM-PNIPAM-solvent}}$ (kJ·mol ⁻¹) | $E_{\text{het.comp.}}$ (kJ·mol ⁻¹) |
|-------------|--|---|---|---|
| DMAC | -61.5 | -48.1 | -49.0 | -25.9 |
| DMSO | -59.8 | -53.6 | -52.7 | -13.4 |
| NMP | -62.3 | -54.0 | -55.2 | -15.5 |

20. Theoretical model of nanofiltration

To study the effect of MOF micropores on the nanofiltration performance, a predictive model was created to simulate nanofiltration through MMMs at different operational parameters to correlate structural properties with filtration performance. The pore flow model developed by Bowen and Welfoot was used to describe the nanofiltration process.¹¹ A detailed description of this model, including equations and assumptions, can be found in the Supporting Information. Most importantly, the model assumes the permeation of a diluted solution of uncharged spherical solutes dissolved in a continuous medium through isolated, parallel, and cylindrical pores. The model can be used to obtain rejection and flux values if the pore size or pore distribution, porosity, selective layer thickness, solvent properties, solute chemical structure, temperature, and pressure are known. The pore properties of MOFs can be obtained by analyzing their crystal structure; thus, nanofiltration through the internal pores of a MOF layer can be studied using this model. The highly ordered crystal structure of MOFs allows pore size to be estimated from single-crystal X-ray data. However, the rotational dynamics of *p*-phenylene rings in the MOF and the random orientation of the amino groups in the lattice makes the aperture diameter reading less precise.^{12,13} Assuming different angles between the planes of the phenylene ring and aperture, three pore diameter estimates (tight, mid, and loose) were established for each type of MOF (Fig. S56). Furthermore, the pore-limiting diameter can be calculated from structural data using computational tools such as PoreBlazer v4.0. Other experimental information, namely the PSD obtained from nitrogen sorption experiments, can be used in nanofiltration modeling. The porosity in the direction of flow can be calculated using the pore size and distance of neighboring metal nodes in the framework. To better correlate the experimental results with that obtained using the nanofiltration model, the selective layer thickness was derived from analytical data, namely the average particle size of MOFs. This estimation reflects a scenario when permeation occurs through the MOF particles in the top layer of the membrane and the finger-like pores underneath do not significantly contribute to the overall selectivity or flow resistance. By the same logic, a correction of the estimated flux value is required to account for the proportion of MOF particles in the membrane top layer to that in the polymeric matrix, which is assumed to be impermeable in the model. The MOF coverage of the selective layer was obtained from the relative cumulative areas of the particles and polymer matrix in the top-section SEM images of the prepared MMMs. Predicted MWCO curves were constructed using a hypothetical polystyrene series comprising ethylbenzene, 1,3-diphenylbutane, and 1,3,5-triphenylhexane. To obtain continuous curves, virtual molecules with a 1-g·mol⁻¹ step size whose molecular properties were spline-interpolated between polystyrene oligomers were inputted in the model calculations.

The pore flow model developed by Bowen and Welfoot was used to describe the nanofiltration process.¹¹ The most important assumptions and equations are discussed here. For a detailed description of the model and its comparison with other nanofiltration models, please refer to Bowen and Welfoot,¹¹ Silva and Livingston,¹⁴ and Santos *et al.*¹⁵

The model assumes that the membrane has a selective layer with uniform Δx thickness, which is solely responsible for the selectivity and flow resistance of the membrane. Laminar solution flux occurs through unconnected cylindrical pores perpendicular to the plane of the membrane. The average fluid velocity (V) can be described using the Hagen–Poiseuille equation:

$$V = \frac{r_p^2 \Delta P_e}{8\eta \Delta x} \quad (S7)$$

where r_p is the pore radius, ΔP_e is the effective pressure difference between the two sides of the membrane, and η is the solution viscosity, which equals solvent viscosity at low concentrations.

ΔP_e is the difference of the applied transmembrane pressure (ΔP) and the osmotic pressure difference ($\Delta \pi$). In dilute organic solutions of uncharged solutes, osmotic pressure is negligible compared to the applied transmembrane pressure; thus, ΔP_e equals ΔP . The uncharged solute flux (j_s) at a certain point inside the membrane is the sum of convective and diffusional terms. The convective term is directly proportional to the product of fluid velocity and solute concentration ($c = c(x)$) at that point. The coefficient of proportionality is the uncharged solute hindrance factor for convection (K_c). The diffusional term can be described by one-dimensional Fick's first law assuming ideal solution and no radial diffusion:

$$j_s = K_c c V - \frac{D_p c}{RT} \frac{d\mu}{dx} \quad (S8)$$

where D_p is the pore diffusion coefficient, R is the universal gas constant ($8.314 \text{ J}\cdot\text{K}^{-1}\cdot\text{mol}^{-1}$), T is the absolute temperature, μ is the chemical potential, and x is the cross-membrane coordinate.

In ideal solutions and isothermal conditions, the chemical potential is made up from concentration-dependent, pressure-dependent, and constant terms:

$$\mu = RT \ln c + V_s P + \text{constant} \quad (S9)$$

where V_s is the molar volume of the solute, and P is the pressure. In equilibrium, the solute flux can be also written as the product of the permeate concentration (C_p) and fluid velocity.

Therefore, by combining Equations. (S7)–(S9) and assuming constant pressure gradient, the following differential equation is obtained.

$$\frac{dc}{dx} = \frac{V}{D_p} \left[\left(K_c - \frac{D_p V_s 8\eta}{RT r_p^2} \right) c - C_p \right] = \frac{V}{D_p} [(K_c - Y)c - C_p] \quad (S10)$$

For simplicity, Y is often introduced to denote the coefficient of the pressure-induced diffusion term. The differential equation can be integrated for the length of the membrane pores, i.e., between 0 and membrane thickness (Δx). The pore concentration boundaries are the feed and permeate concentrations multiplied by the steric partitioning coefficient (ϕ).

$$\int_{\phi C_f}^{\phi C_p} \frac{1}{(K_c - Y)c - C_p} dc = \int_0^{\Delta x} \frac{V}{D_p} dx \quad (S11)$$

Integration and rearrangement results in an equation that correlates the permeate and feed concentrations:

$$\frac{C_p}{C_f} = \frac{(K_c - Y)\phi \cdot e^{\frac{(K_c - Y)V\Delta x}{D_p}}}{(K_c - Y)\phi - 1 + e^{\frac{(K_c - Y)V\Delta x}{D_p}}} = \frac{(K_c - Y)\phi \cdot e^{Pe'}}{(K_c - Y)\phi - 1 + e^{Pe'}} \quad (S12)$$

The exponent is often defined as the modified Peclet number (Pe'). Pe' can be written in a different form by expressing $V\Delta x$ using the Hagen–Poiseuille equation. After rearrangement of the equation and insertion in the definition of rejection, the following equation is obtained, which allows calculating rejections according to the pore flow model (Equation (S13)).

$$R = 1 - \frac{(K_c - Y)\phi}{1 - [1 - (K_c - Y)\phi] \cdot e^{-Pe'}} \quad (S13)$$

Y and Pe' both contain the product of pore viscosity and pore diffusion coefficient. This product is directly proportional to the bulk parameters through the hindrance factor for diffusion (K_d).

$$D_p\eta = K_d D_\infty \eta_0 \quad (S14)$$

Therefore, Y and Pe' can be written as follows:

$$Y = \frac{8K_d D_\infty \eta_0}{RT r_p^2} V_s \quad (S15)$$

$$Pe' = \frac{(K_c - Y) r_p^2}{8K_d D_\infty \eta_0} \Delta P \quad (S16)$$

The solute molar volumes (V_s) at normal boiling point can be estimated using group contribution methods described by Schotte.¹⁶ With V_s in hand, bulk diffusivity (D_∞) can be calculated using the Wilke–Chang correlation.¹⁷ The dimensionless association coefficient (α_{sv}) for the solvent was used according to Miyabe and Isogai, while the solute was presumed to be nonassociating ($\alpha_s = 1$).¹⁸

$$D_\infty = \frac{7.4 \times 10^{-8} T \sqrt{\alpha_{sv} M_{sv}}}{\eta_0 (\alpha_s V_s)^{0.6}} \quad (S17)$$

The empiric correlation provides D_∞ in $\text{cm}^2 \cdot \text{s}^{-1}$ when T is given in K, solvent molecular weight (M_{sv}) in $\text{g} \cdot \text{mol}^{-1}$, η_0 in cP, and V_s in $\text{cm}^3 \cdot \text{mol}^{-1}$. K_c , K_d , and ϕ depend on the solute-to-pore-radii fraction (λ). The solute radius (r_s) can be obtained from the Stokes–Einstein equation; thus, λ can also be calculated:

$$r_s = \frac{k_B T}{6\pi\eta_0 D_\infty} \quad (S18)$$

$$\lambda = \frac{r_s}{r_p} \quad (S19)$$

where k_B is the Boltzmann constant ($1.38 \times 10^{-23} \text{ J}\cdot\text{K}^{-1}$).

Consequently, ϕ can be easily calculated as follows when assuming purely steric interactions between the solute and pore wall.

$$\phi = (1 - \lambda)^2 \quad (S20)$$

K_c and K_d can be calculated using the empiric model developed by Bowen et al. for $0 < \lambda \leq 0.8$ ¹⁹ and extended by Bandini and Vezzani to $0.8 \leq \lambda \leq 1$ for practical purposes.²⁰ The model assumes fully developed flow and uses the center-line approximation. The model parameters are listed in Table S11.

$$K_c = (2 - \phi)(A + B\lambda + C\lambda^2 + D\lambda^3) \quad (S21)$$

$$K_d = E + F\lambda + G\lambda^2 + H\lambda^3 \quad (S22)$$

Table S11. Model parameters used to calculate the hindrance factors, K_c and K_d .

| Parameter | $0 < \lambda \leq 0.8$ | $0.8 \leq \lambda \leq 1$ |
|-----------|------------------------|---------------------------|
| <i>A</i> | 1 | -6.830 |
| <i>B</i> | 0.054 | 19.348 |
| <i>C</i> | -0.988 | -12.518 |
| <i>D</i> | 0.441 | 0 |
| <i>E</i> | 1 | -0.105 |
| <i>F</i> | -2.30 | 0.318 |
| <i>G</i> | 1.154 | -0.213 |
| <i>H</i> | 0.224 | 0 |

Equations (S20)–(S22) are applicable only when $\lambda \leq 1$, i.e., when the solute radius is smaller than the pore radius. When $\lambda \geq 1$, the solute molecule does not fit into the pore; therefore, the rejection is 1.

Equations (S13)–(S22) can be used directly to calculate rejections of isoporous membranes for any given molecule. Of note, rejections do not depend on either the membrane thickness (Δx) or pore

viscosity (η) according to this set of presumptions; moreover, knowledge of accurate molecular structures is essential to obtain the V_s values. To obtain continuous MWCO curves, interpolation can be used to obtain V_s values for arbitrary molecular weights. In this study, predicted MWCO curves were constructed using a hypothetical polystyrene series comprising ethylbenzene, 1,3-diphenylbutane, and 1,3,5-triphenylhexane. To obtain continuous curves, virtual molecules with a 1-g-mol⁻¹ step size, whose molecular properties were spline-interpolated between polystyrene oligomers, were inputted into model calculations. This approach can be modified for any polymer series as necessary, e.g., for a polyethylene glycol series comprising ethylene glycol, diethylene glycol, and triethylene glycol (Fig. S54).

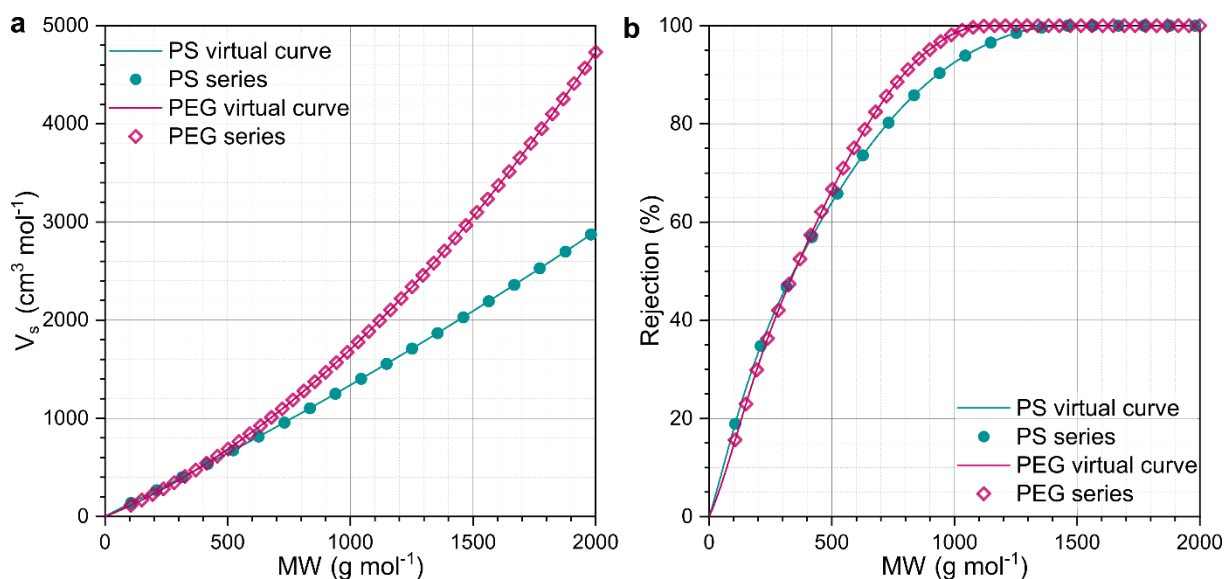


Fig. S54. a) Solute molar volumes (V_s) of polystyrene (PS) and polyethylene glycol (PEG) series obtained using the group contribution method, and continuous curves showing interpolated values. b) Predicted discrete rejection values and continuous MWCO curves constructed using data from the PS and PEG series and from interpolated virtual values on a hypothetical isoporous membrane with a pore diameter of 2.5 nm at 30 bar and 20°C.

The pore flow model can be extended to membranes with log-normal PSD. The key considerations and equations are described here; however, the reader can refer to Bowen and Welfoot for a detailed discussion.²¹ The log-normal distribution can be described using the following probability density function of the pore size variable (r):

$$f_R(r) = \frac{1}{r\sqrt{2\pi b}} e^{-\frac{\left(\ln\frac{r}{r_p^*} + \frac{b}{2}\right)^2}{2b}} \quad (\text{S23})$$

where

$$b = \ln \left[1 + \left(\frac{\sigma_p^*}{r_p^*} \right)^2 \right] \quad (\text{S24})$$

and r_p^* and σ_p^* are the PSD mean and standard deviation, respectively.

The number of pores per unit area ($n(r)$) with a radius in the infinitesimal surrounding of r can be obtained using the density function:

$$n(r) = f_R(r)N_0 \quad (S25)$$

where N_0 is the total number of pores per unit area.

Total solute flux (j_s) and volumetric flux (Q) can be obtained by integrating their porewise values over the entire range of PSD. Consequently, the overall permeate concentration can be written as the quotient of the two:

$$C_p = \frac{j_s}{Q} = \frac{\int_0^\infty N_0 f_R(r) V(r) r^2 \pi C_p(r) dr}{\int_0^\infty N_0 f_R(r) V(r) r^2 \pi dr} \quad (S26)$$

where porewise values are shown as a function of the pore radius.

$V(r)$ and $C_p(r)$ can be substituted using Equation (S7) and the definition of rejection. Accordingly, the overall rejection can be written as

$$R = \frac{\int_0^\infty \frac{f_R(r) R(r) r^4}{\eta(r)} dr}{\int_0^\infty \frac{f_R(r) r^4}{\eta(r)} dr} \quad (S27)$$

Bowen and Welfoot argued that the mathematical formula that describes the log-normal distribution can lead to results that lack physical validity.²¹ According to Equation (S23), the probability density of any arbitrarily large pore is low but not zero. At certain values of r_p^* and σ_p^* , the presence of these large pores implied by the mathematical description can significantly affect the predicted values of rejection and other process parameters. Truncation of the probability density function can bring the mathematical model closer to the physical reality. Based on experimental evidence, truncation at $r_{\max} = 2r_p^*$ has been previously proposed.²¹ Furthermore, pores smaller than solvent molecules can be disregarded for permeation. Therefore, the $r_{\min} = r_{sv}$ lower limit can be applied, where r_{sv} is the radius of solvent molecules. The corrected distribution function and the overall rejection can be written as follows:

$$f'_R(r) = \frac{f_R(r)}{\int_{r_{\min}}^{r_{\max}} f_R(r) dr} \quad (S28)$$

$$R = \frac{\int_{r_{\min}}^{r_{\max}} \frac{f'_R(r) R(r) r^4}{\eta(r)} dr}{\int_{r_{\min}}^{r_{\max}} \frac{f'_R(r) r^4}{\eta(r)} dr} \quad (S29)$$

There is little experimental work on solvent viscosities in nanosized channels, but these suggest that viscosities at pore walls are substantially higher than their bulk values. Based on these observations, the following correlation was proposed to calculate porewise average viscosities.

$$\eta(r) = \eta_0 \left[1 + 18 \frac{d_{sv}}{r} - 9 \left(\frac{d_{sv}}{r} \right)^2 \right] \quad (S30)$$

The diameter of solvent molecules can be calculated from van-der-Waals volumes assuming spherical particles. The van-der-Waals volumes can be obtained via the group contribution method.²²

Equations (S13) and (S29) can be used to predict rejections based on isoporous pore size and PSD, respectively. These can also be applied to obtain pore size information using experimental rejection values; for this, the model can be fitted on the experimental MWCO curve using the ordinary least squares method.

Solvent permeance (P) can be easily obtained for isoporous membranes using the Hagen–Poiseuille correlation. For composite materials, the correlation is corrected with the proportion of the porous media in the selective layer (ω), which is referred to as MOF coverage in this study:

$$P = \varepsilon \frac{r_p^2}{8\eta \Delta x} \omega \quad (S31)$$

where ε is the porosity of the selective membrane layer.

The pore viscosity (η) can be obtained from Equation (S30). The analogous equation for a membrane with a log-normal PSD can be written as follows.

$$P = \frac{N_0 \pi \omega}{8 \Delta x} \int_{r_{\min}}^{r_{\max}} \frac{f'_R(r)r^4}{\eta(r)} dr \quad (S32)$$

N_0 is rarely known; however, if the porosity of the selective layer is known, it can be obtained using the following correlation.

$$\varepsilon = N_0 \pi \int_{r_{\min}}^{r_{\max}} f'_R(r)r^2 dr \quad (S33)$$

By combining Equations (S32) and (S33), a single equation is obtained to calculate solvent permeance.

$$P = \frac{\varepsilon}{8 \Delta x} \frac{\int_{r_{\min}}^{r_{\max}} \frac{f'_R(r)r^4}{\eta(r)} dr}{\int_{r_{\min}}^{r_{\max}} f'_R(r)r^2 dr} \quad (S34)$$

For isoporous membrane predictions, the porosity was obtained using the estimated pore size and pore density obtained from crystallographic data, as shown in Fig. S55. For pore-distribution-corrected membrane predictions, N_0 was assumed to be identical to an isoporous scenario.

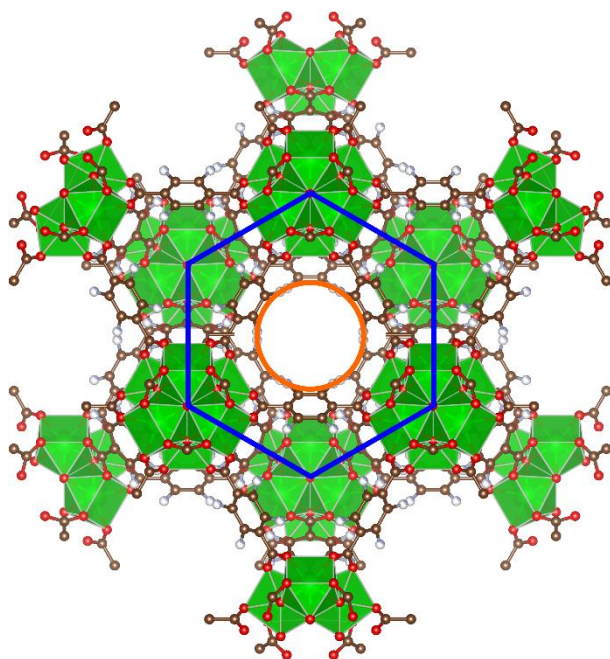


Fig. S55. For MOFs studied herein, the flow-direction porosity was obtained as the quotient of one circular pore area (orange) and the area of the hexagon determined by the neighboring metal nodes (blue).

21. Estimating pore size for the nanofiltration model

Pore diameter is an essential initial parameter for nanofiltration predictive models. The highly ordered crystal structure of MOFs allows this parameter to be obtained from single-crystal X-ray data. However, the rotational dynamics of benzene rings in MOF and the random orientation of amino groups in the lattice makes the aperture diameter reading less precise.^{12,13} Therefore, three estimates [loose, tight, and average (mid)] were obtained for each MOF. Tight estimates were obtained as the inscribed circle of the centers of the nitrogen atoms facing the center of a pore. Loose estimates were obtained as the inscribed circle of the centers of the middle two carbon atoms in the linker molecules. The diameter of the mid estimate was obtained as the average of the tight and loose estimates. Similarly, the PoreBlazer v4.0 tool can be used to estimate the aperture size from structural data. Single-crystal X-ray structures of UiO-66-NH₂ (ID: 1507786), UiO-67-NH₂ (ID: 1026990), and UiO-68-NH₂ (ID: 1847052) were obtained from the Cambridge Structural Database (CCDC).⁸

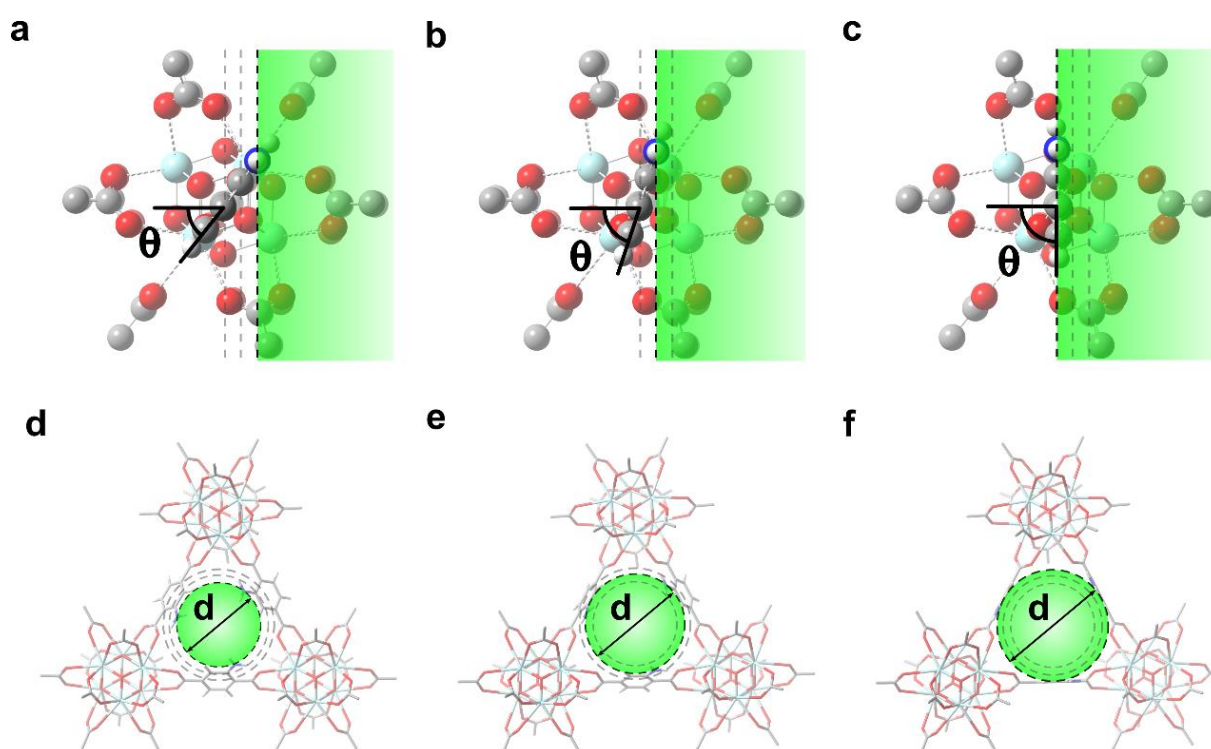


Fig. S56. Rotation of the linker phenylene group affecting the aperture diameter. The angle between the plane of the aperture and phenylene ring (θ) corresponding to the (a) tight, (b) mid, and (c) loose estimates are shown. The angle affects the diameter of the inscribed circle, as shown in panels (d)–(f). Different estimates were used in the predictive model of nanofiltration to explore the effects of the linkers' rotational dynamics on the filtration performance through the MOF pores.

BET analysis also provides an estimate of the pore diameter of MOF. Because the conditions of N₂ sorption tests are very different from those of the organic solvent nanofiltration (OSN) experiments in terms of temperature, pressure, and solvation, the pore size results are not directly transferable between the two. Nevertheless, the mean pore diameter obtained from BET analysis was similar to that from XRD, confirming that it can provide reasonably accurate estimates if no other data are available. An advantage of this estimation is that it can also provide information about the pore distribution; therefore, it can be used not only for isoporous models but also for distribution-weighted predictions. The distribution was fitted using the “fit” function of MATLAB and a log-normal

distribution model. In isoporous prediction, only the mean pore size was used and the standard deviation was disregarded. Because the PNIPAM attachment to the surface is not expected to change the internal pore size of the MOF particles, the same pore diameters were used for the unmodified and PNIPAM-containing membranes.

Table S12. Different pore size estimates (i.e., tight, mid, and loose) based on the single-crystal X-ray structure (XRD te., XRD me., and XRD le., respectively), PoreBlazer v4.0 method, estimation from BET analysis of UiO-66-NH₂ and UiO-66-PNIPAM in isoporous (BET N and BET P) and distribution-weighted (BET N dw. and BET P dw.) versions.

| Estimation | M66 ^{P/N} | | M67 ^{P/N} | | M66 ^{P/N} | |
|------------|---------------------------|------------------|---------------------------|------------------|---------------------------|------------------|
| | (Mean) Pore diameter (nm) | Std. Dev. (nm) | (Mean) Pore diameter (nm) | Std. Dev. (nm) | (Mean) Pore diameter (nm) | Std. Dev. (nm) |
| XRD te. | 0.572 | n/a ^a | 0.634 | n/a ^a | 0.947 | n/a ^a |
| XRD me. | 0.710 | n/a ^a | 0.864 | n/a ^a | 1.141 | n/a ^a |
| XRD le. | 0.848 | n/a ^a | 1.094 | n/a ^a | 1.335 | n/a ^a |
| Poreblazer | 0.382 | n/a ^a | 0.549 | n/a ^a | 0.970 | n/a ^a |
| BET N | 0.908 | n/a ^a | 0.967 | n/a ^a | 1.256 | n/a ^a |
| BET P | 1.036 | n/a ^a | 0.940 | n/a ^a | 1.179 | n/a ^a |
| BET N dw. | 0.908 | 0.034 | 0.967 | 0.086 | 1.256 | 0.165 |
| BET P dw. | 1.036 | 0.156 | 0.940 | 0.115 | 1.179 | 0.123 |

^aNot applicable because isoporosity was assumed.

22. Organic solvent nanofiltration experiments and results

A crossflow membrane filtration apparatus equipped with two flat-sheet-membrane cells, a back-pressure regulator, a high-pressure pump, and a microannular gear pump was used for OSN. To minimize concentration polarization, the crossflow rate in the retentate loop was kept at $100 \text{ L}\cdot\text{h}^{-1}$. The effective membrane area in each cell was 52.8 cm^2 . To tighten the pores of the PBI matrix, the membranes were partially dried at $23 \pm 1^\circ\text{C}$ over 6 h. The membranes were conditioned in acetone at 30 bar for 24 h before solvent-flux (Equation (S35)) and solute-rejection (Equation (S36)) measurements. The feed concentration of each solute was 100 ppm. The reported results are the average values of two independently prepared membranes.

$$J = \frac{V}{A t} \quad (\text{S35})$$

where J is flux, V is the permeate volume collected in time t , and A is membrane area.

$$R (\%) = \frac{C_f - C_p}{C_f} \cdot 100\% \quad (\text{S36})$$

where R is rejection, C_f is feed side concentration, and C_p is permeate concentration.

Flux data were obtained for pure acetone. Rejection data were obtained after changing the feed to the marker solution and conditioning. The markers used for obtaining the rejection data are summarized in Table S15.

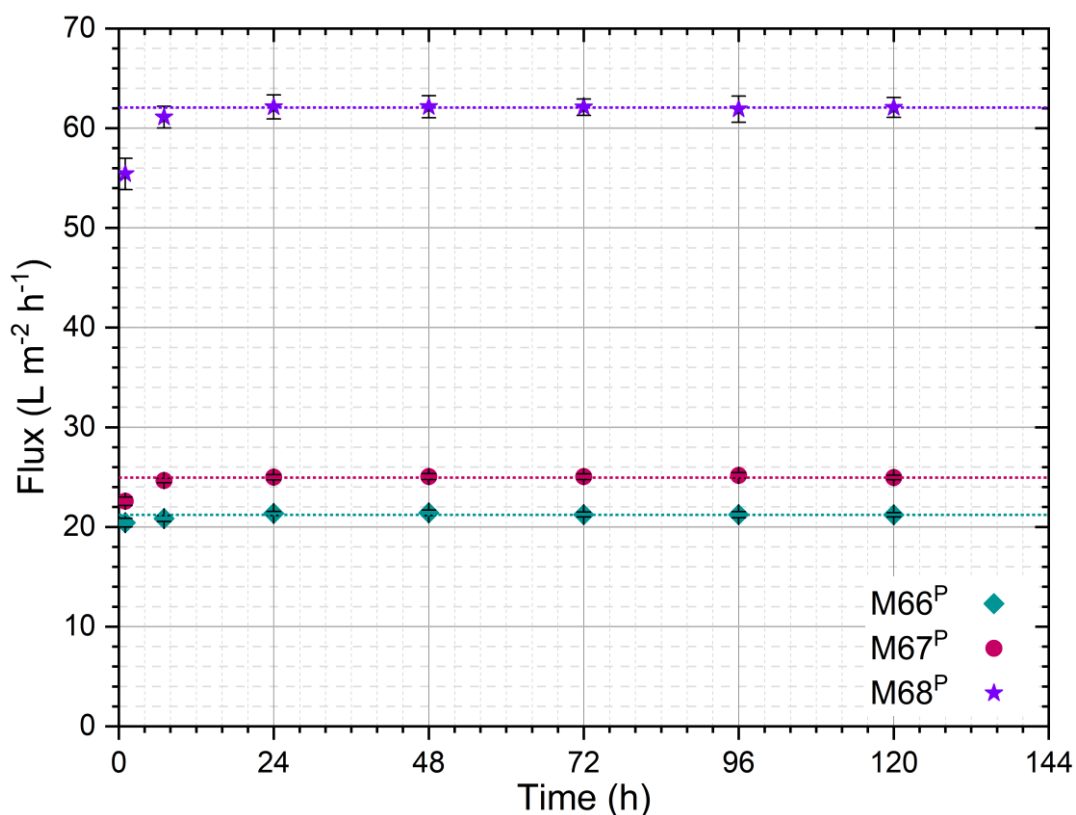


Fig. S57. Experimental flux change during 120 h of OSN operation for M66^P, M67^P, and M68^P membranes. The flux reaches a steady state after 24 h of filtration, which is maintained throughout the remainder of the experiment. The dotted lines indicate the steady flux as measured after 120 h.

Table S13. Change in experimental acetone flux (and permeance) during 120 h of OSN operation for M66^P, M67^P, and M68^P membranes at 30 bar and 20°C. (Numerical data for Fig. S57)

| Membrane | Time (h) | Flux (L·m ⁻² ·h ⁻¹) | Flux Std. Dev. (L·m ⁻² ·h ⁻¹) | Permeance (L·m ⁻² ·h ⁻¹ ·bar ⁻¹) | Permeance Std. Dev. (L·m ⁻² ·h ⁻¹ ·bar ⁻¹) |
|------------------|----------|--|--|--|--|
| M66 ^P | 1 | 20.43 | 0.43 | 0.68 | 0.01 |
| | 7 | 20.85 | 0.29 | 0.69 | 0.01 |
| | 24 | 21.35 | 0.20 | 0.71 | 0.01 |
| | 48 | 21.41 | 0.28 | 0.71 | 0.01 |
| | 72 | 21.24 | 0.25 | 0.71 | 0.01 |
| | 96 | 21.23 | 0.31 | 0.71 | 0.01 |
| | 120 | 21.22 | 0.21 | 0.71 | 0.01 |
| M67 ^P | 1 | 22.58 | 0.43 | 0.75 | 0.01 |
| | 7 | 24.66 | 0.22 | 0.82 | 0.01 |
| | 24 | 24.98 | 0.27 | 0.83 | 0.01 |
| | 48 | 25.05 | 0.29 | 0.84 | 0.01 |
| | 72 | 25.04 | 0.29 | 0.83 | 0.01 |
| | 96 | 25.17 | 0.28 | 0.84 | 0.01 |
| | 120 | 24.96 | 0.23 | 0.83 | 0.01 |
| M68 ^P | 1 | 55.41 | 1.56 | 1.85 | 0.05 |
| | 7 | 61.11 | 1.09 | 2.04 | 0.04 |
| | 24 | 62.14 | 1.21 | 2.07 | 0.04 |
| | 48 | 62.16 | 1.10 | 2.07 | 0.04 |
| | 72 | 62.11 | 0.82 | 2.07 | 0.03 |
| | 96 | 61.91 | 1.32 | 2.06 | 0.04 |
| | 120 | 62.08 | 1.00 | 2.07 | 0.03 |

Table S14. Experimental acetone flux (and permeance) after 24 h of OSN operation for M66^N, M67^N, and M68^N membranes at 30 bar and 20°C.

| Membrane | Time (h) | Flux (L·m ⁻² ·h ⁻¹) | Flux Std. Dev. (L·m ⁻² ·h ⁻¹) | Permeance (L·m ⁻² ·h ⁻¹ ·bar ⁻¹) | Permeance Std. Dev. (L·m ⁻² ·h ⁻¹ ·bar ⁻¹) |
|------------------|----------|--|--|--|--|
| M66 ^N | 24 | 927.0 | 91.9 | 30.90 | 3.06 |
| M67 ^N | 24 | 1059.4 | 62.5 | 35.31 | 2.08 |
| M68 ^N | 24 | 995.6 | 144.5 | 33.19 | 4.82 |

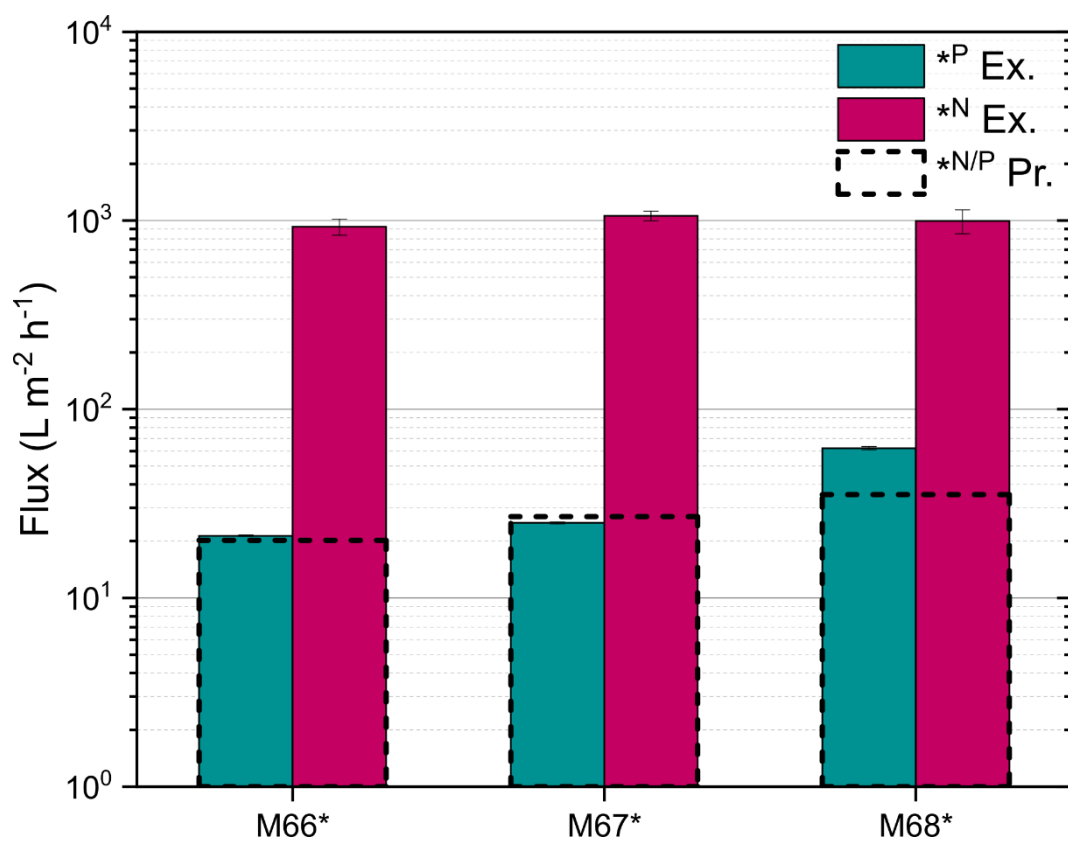


Fig. S58. Experimental acetone flux values for M66^N, M67^N, M68^N, M66^P, M67^P, and M68^P membranes compared with model predictions at 30 bar and 20°C.

Table S15. List of marker solutes used for testing the OSN performance of membranes and for constructing experimental MWCO curves.

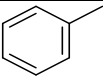
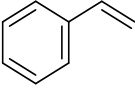
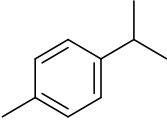
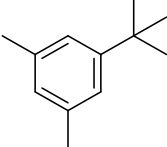
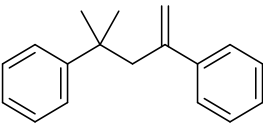
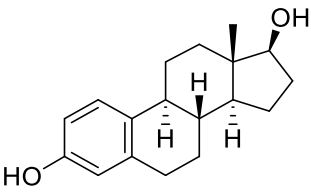
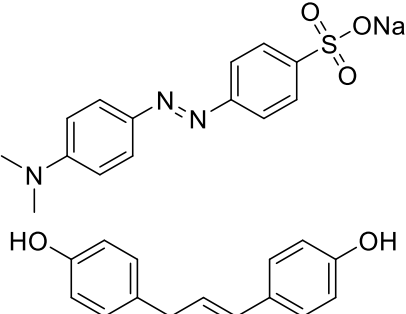
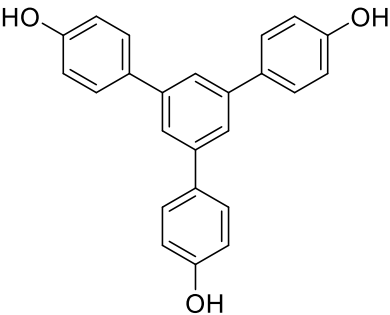
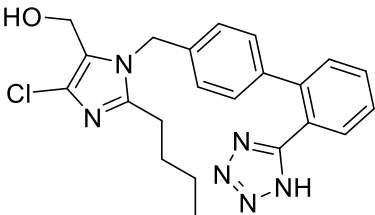
| Name [CAS] | Structure | Molecular weight (g·mol ⁻¹) |
|--|---|--|
| Toluene [108-88-3] |  | 92.14 |
| Styrene [100-42-5] |  | 104.15 |
| p-Cymene [99-87-6] |  | 134.22 |
| 1-tert-Butyl-3,5-dimethylbenzene [98-19-1] |  | 162.27 |
| Styrene dimer [6362-80-7] |  | 236.35 |
| Estradiol [50-28-2] |  | 272.38 |
| Methyl orange [547-58-0] |  | 327.33 |
| 1,3,5-Tris(4-hydroxyphenyl)benzene [15797-52-1] |  | 354.40 |
| Losartan [114798-26-4] |  | 422.92 |

Table S16. Experimental rejection values of the M66^N, M67^N, and M68^N membranes for the marker series (see Table S15) measured in crossflow OSN experiments at 30 bar and 20°C. The MWCO values of all membranes were well above the studied molecular weight (MW) range, as shown by low rejections (<20%).

| Membrane [MWCO (g·mol ⁻¹)] | Marker MW (g·mol ⁻¹) | Rejection (%) | Rej. Std. Dev. (%) |
|---|-------------------------------------|------------------|-----------------------|
| M66 ^N | 92.14 | 2.14 | 1.28 |
| | 104.15 | 3.15 | 2.40 |
| | 134.22 | 5.35 | 2.50 |
| | 162.27 | 7.38 | 2.08 |
| | 236.35 | 9.15 | 3.27 |
| | 272.38 | 9.88 | 2.34 |
| | 327.33 | 14.53 | 3.20 |
| | 354.40 | 15.90 | 1.48 |
| | 422.92 | 17.79 | 2.19 |
| M67 ^N | 92.14 | 3.34 | 1.97 |
| | 104.15 | 3.98 | 1.61 |
| | 134.22 | 5.10 | 2.69 |
| | 162.27 | 7.02 | 2.42 |
| | 236.35 | 9.25 | 1.88 |
| | 272.38 | 13.39 | 1.89 |
| | 327.33 | 16.25 | 1.57 |
| | 354.40 | 18.22 | 1.77 |
| | 422.92 | 18.70 | 2.33 |
| M68 ^N | 92.14 | 2.55 | 1.54 |
| | 104.15 | 3.94 | 2.52 |
| | 134.22 | 5.05 | 1.54 |
| | 162.27 | 6.54 | 2.31 |
| | 236.35 | 8.30 | 1.46 |
| | 272.38 | 9.89 | 2.30 |
| | 327.33 | 11.11 | 2.32 |
| | 354.40 | 12.45 | 2.62 |
| | 422.92 | 16.02 | 3.76 |

Table S17. Experimental rejection values of M66^P, M67^P, and M68^P membranes for the marker series (see Table S15) measured in crossflow OSN experiments at 30 bar and 20°C. The MWCO value was obtained via interpolation between adjacent datapoints.

| Membrane [MWCO (g·mol ⁻¹)] | Marker MW (g·mol ⁻¹) | Rejection (%) | Rej. Std. Dev. (%) |
|---|-------------------------------------|------------------|-----------------------|
| M66 ^P [160 ± 1] | 92.14 | 49.86 | 1.36 |
| | 104.15 | 60.35 | 1.67 |
| | 134.22 | 68.28 | 2.63 |
| | 162.27 | 91.91 | 1.01 |
| | 236.35 | 96.69 | 2.00 |
| | 272.38 | 100.00 | 0.00 |
| | 327.33 | 100.00 | 0.00 |
| | 354.40 | 100.00 | 0.00 |
| | 422.92 | 100.00 | 0.00 |
| M67 ^P [211 ± 32] | 92.14 | 36.25 | 2.36 |
| | 104.15 | 44.59 | 2.05 |
| | 134.22 | 66.22 | 1.37 |
| | 162.27 | 86.16 | 2.30 |
| | 236.35 | 92.00 | 2.59 |
| | 272.38 | 96.46 | 1.57 |
| | 327.33 | 100.00 | 0.00 |
| | 354.40 | 100.00 | 0.00 |
| | 422.92 | 100.00 | 0.00 |
| M68 ^P [290 ± 10] | 92.14 | 22.69 | 1.89 |
| | 104.15 | 28.40 | 1.75 |
| | 134.22 | 48.90 | 2.10 |
| | 162.27 | 62.67 | 2.24 |
| | 236.35 | 78.70 | 2.75 |
| | 272.38 | 85.94 | 2.77 |
| | 327.33 | 98.37 | 1.56 |
| | 354.40 | 100.00 | 0.00 |
| | 422.92 | 100.00 | 0.00 |

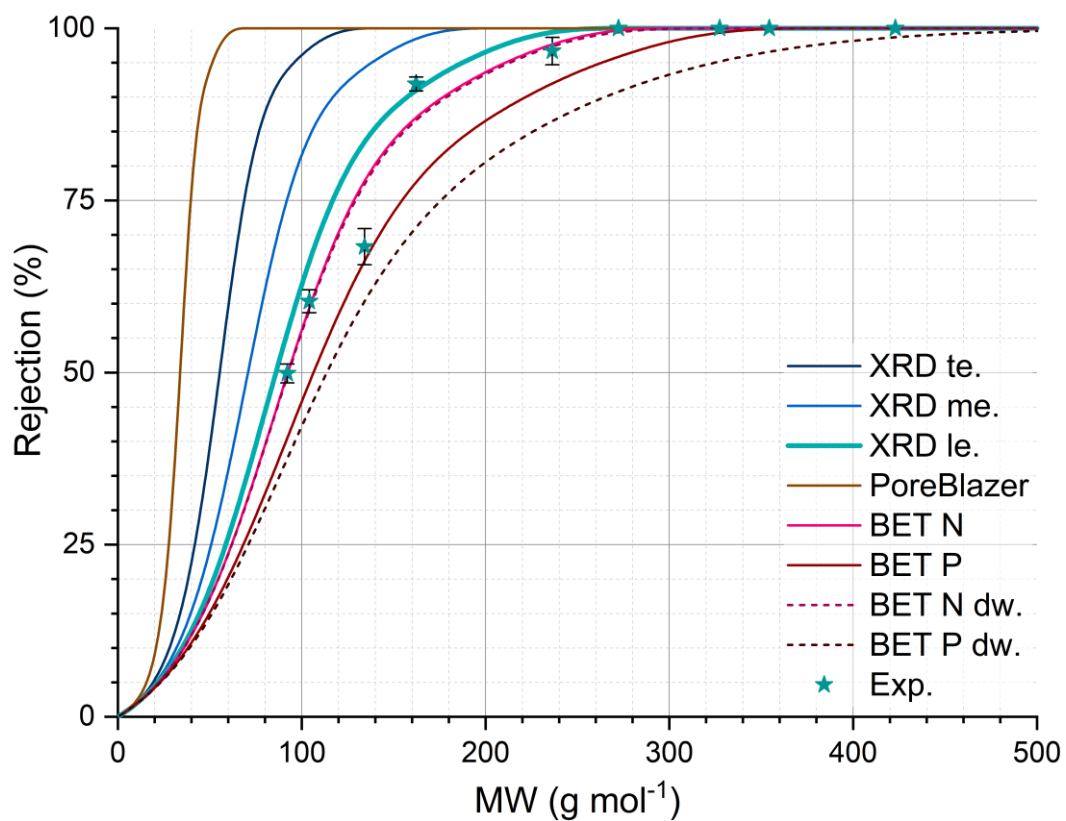


Fig. S59. MWCO curve predictions for M66^P using different pore size estimation methods (Table S12), i.e., tight, mid, and loose estimates based on the single-crystal X-ray structure (XRD te., XRD me., and XRD le.), PoreBlazer v4.0 method, estimation from the BET analysis of UiO-66-NH₂ and UiO-66-PNIPAM in isoporous (BET N and BET P) and distribution-weighted (BET N dw. and BET P dw.) scenarios, and their comparison with experimental rejections (Ex.). (Expanded version of Fig. 4a)

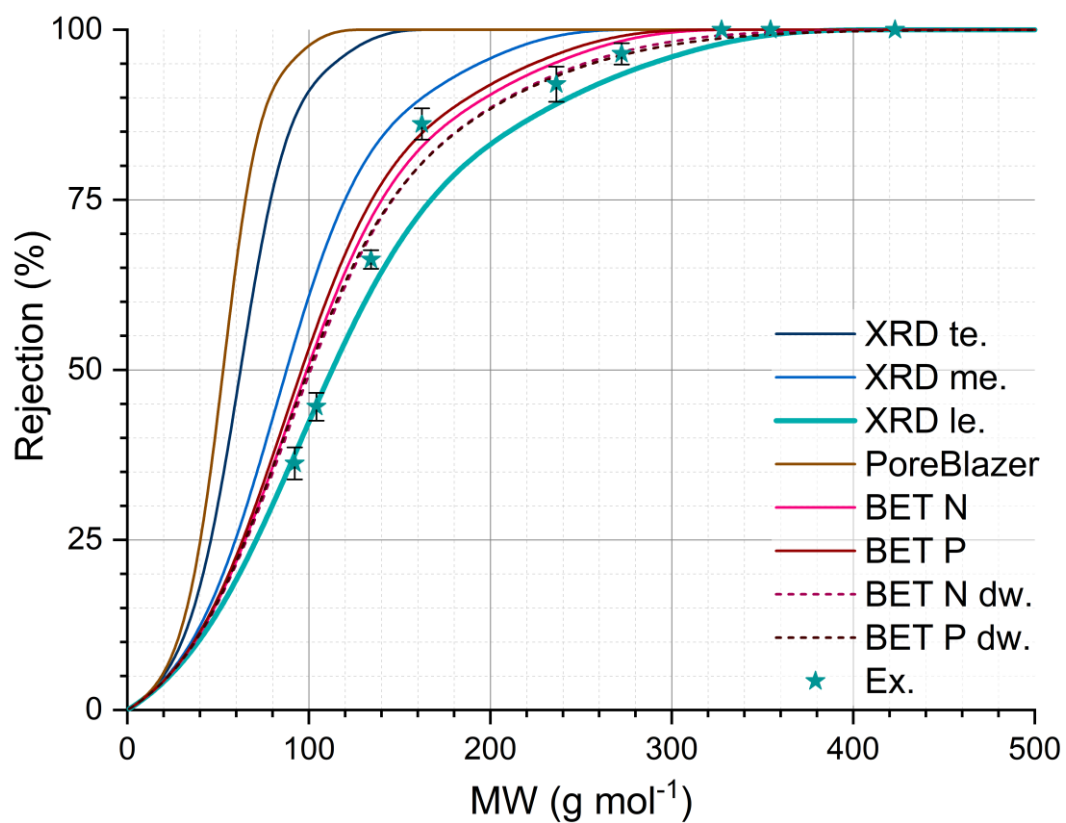


Fig. S60. MWCO curve predictions for M67^P using different pore size estimation methods (Table S12), i.e., tight, mid, and loose estimate based on the single-crystal X-ray structure (XRD te., XRD me., XRD le.), PoreBlazer v4.0 method, estimation from the BET analysis of UiO-66-NH₂ and UiO-66-PNIPAM in isoporous (BET N and BET P) and distribution-weighted (BET N dw. and BET P dw.) scenarios, and their comparison with experimental rejections (Ex.).

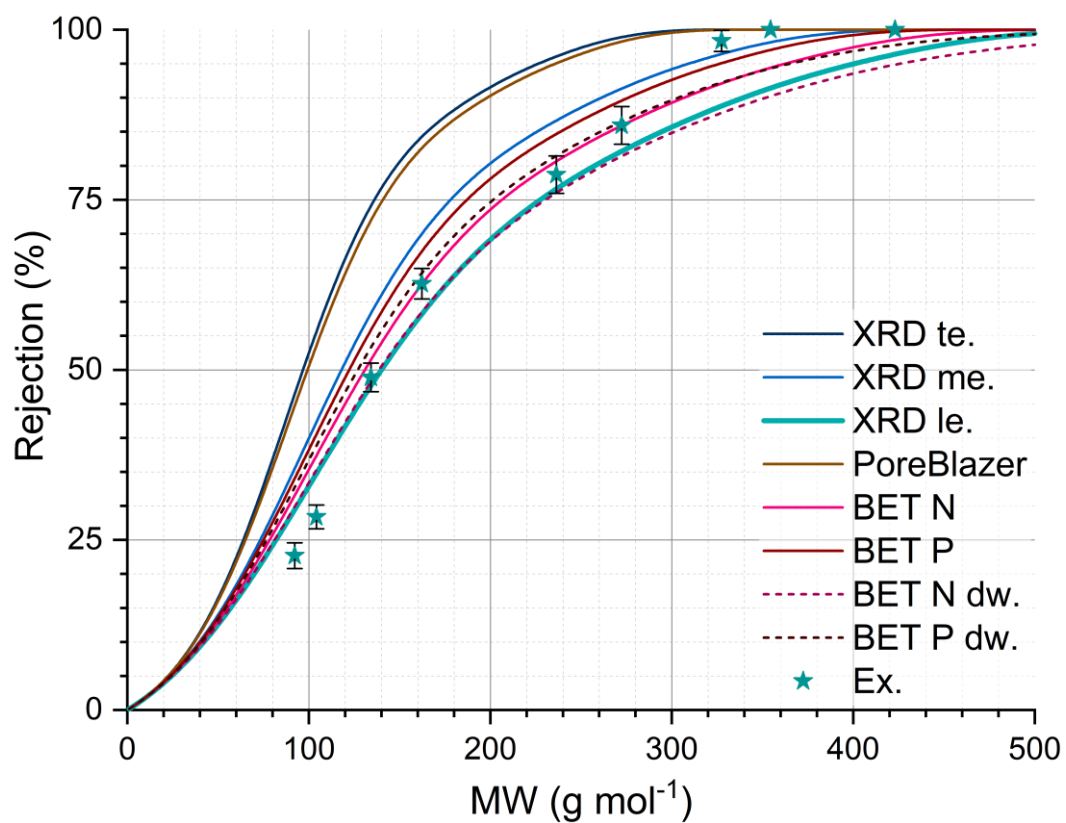


Fig. S61. MWCO curve predictions for M68^P using different pore size estimation methods (Table S12), i.e., tight, mid, and loose estimate based on the single-crystal X-ray structure (XRD te., XRD me., XRD le.), PoreBlazer v4.0 method, estimation from the BET analysis of UiO-66-NH₂ and UiO-66-PNIPAM in isoporous (BET N and BET P) and distribution-weighted (BET N dw. and BET P dw.) scenarios, and their comparison with experimental rejections (Ex.).

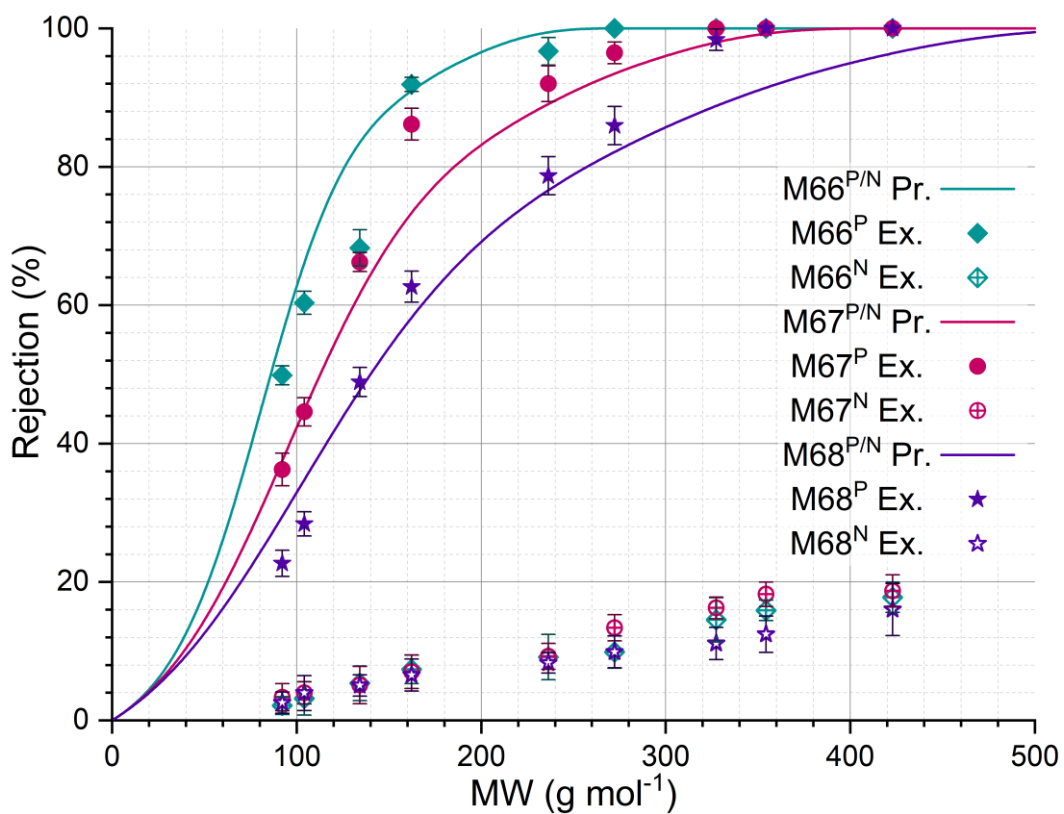


Fig. S62. Predicted (Pr.) MWCO curves from the XRD le. estimation and experimental (Ex.) rejection data of various membranes for the marker series shown in Table S15 at 30 bar and 20°C. (Expanded version of Fig. 4b)

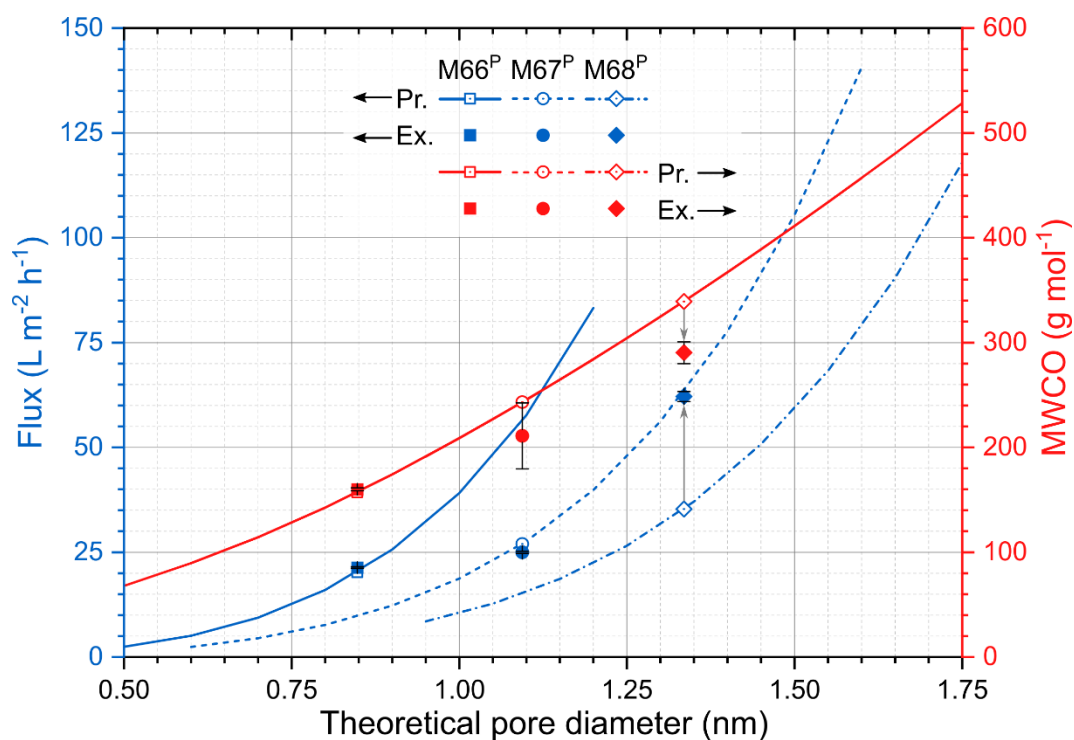


Fig. S63. Predicted (Pr.) and experimental (Ex.) effect of pore size on the membrane performance. (Expanded version of Fig. 4c)

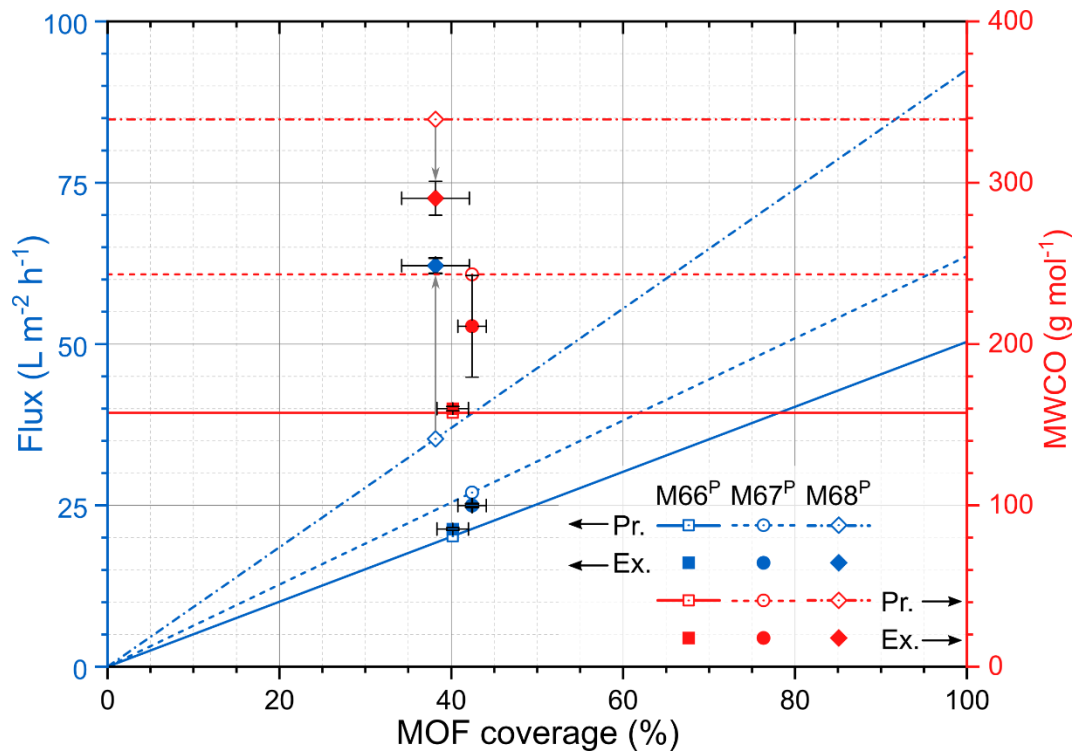


Fig. S64. Predicted (Pr.) and experimental (Ex.) effect of MOF coverage on the membrane performance. (Expanded version of Fig. 4d)

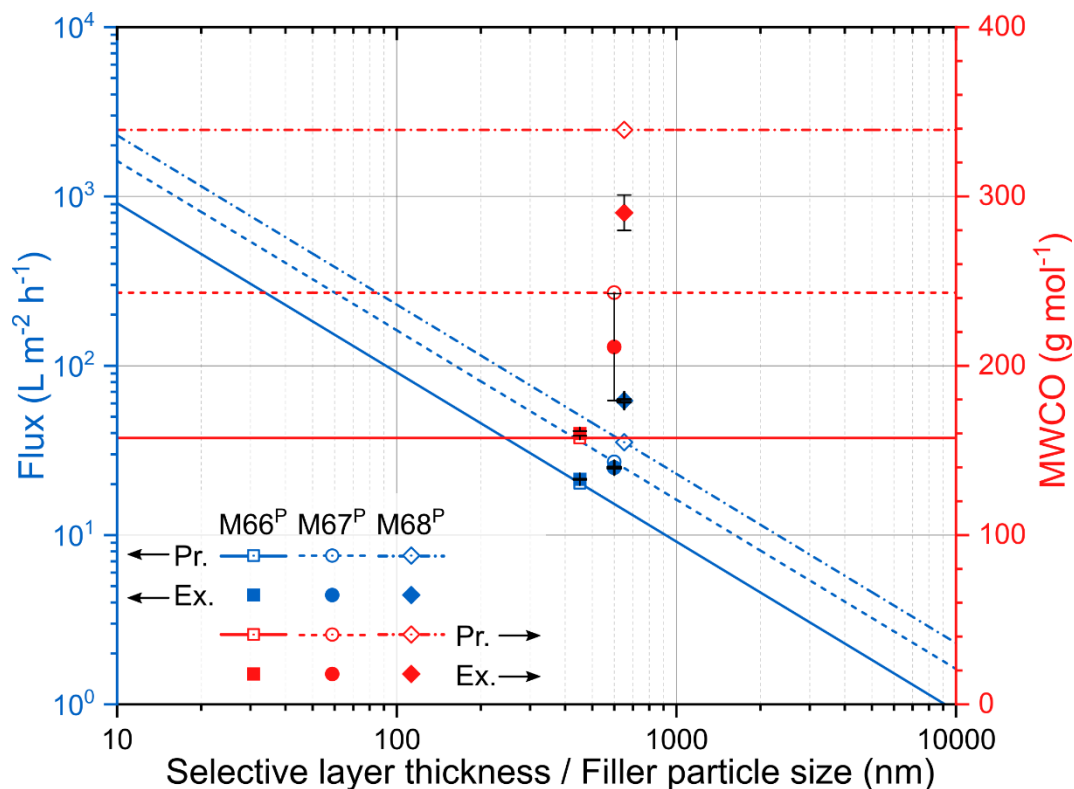


Fig. S65. Predicted (Pr.) and experimental (Ex.) effect of the selective layer thickness (approximated using the experimental filler particle size data) on the membrane performance. (Expanded version of Fig. 4e)

Table S18. Experimental flux (and permeance) after 24 h of OSN operation for the M66^P membranes at 30 bar at various temperatures.

| Temperature (°C) | Acetone Viscosity ^a (mPa s) | Flux (L m ⁻² h ⁻¹) | Flux Std. Dev. (L m ⁻² h ⁻¹) | Permeance (L m ⁻² h ⁻¹ bar ⁻¹) | Permeance Std. Dev. (L m ⁻² h ⁻¹ bar ⁻¹) |
|------------------|--|---|---|--|--|
| 10 | 35.5 | 18.37 | 0.43 | 0.61 | 0.01 |
| 20 | 32.3 | 21.35 | 0.20 | 0.71 | 0.01 |
| 30 | 29.5 | 24.29 | 0.53 | 0.81 | 0.02 |
| 40 | 27.2 | 26.40 | 0.72 | 0.88 | 0.02 |

^aBased on the Vogel equation²³

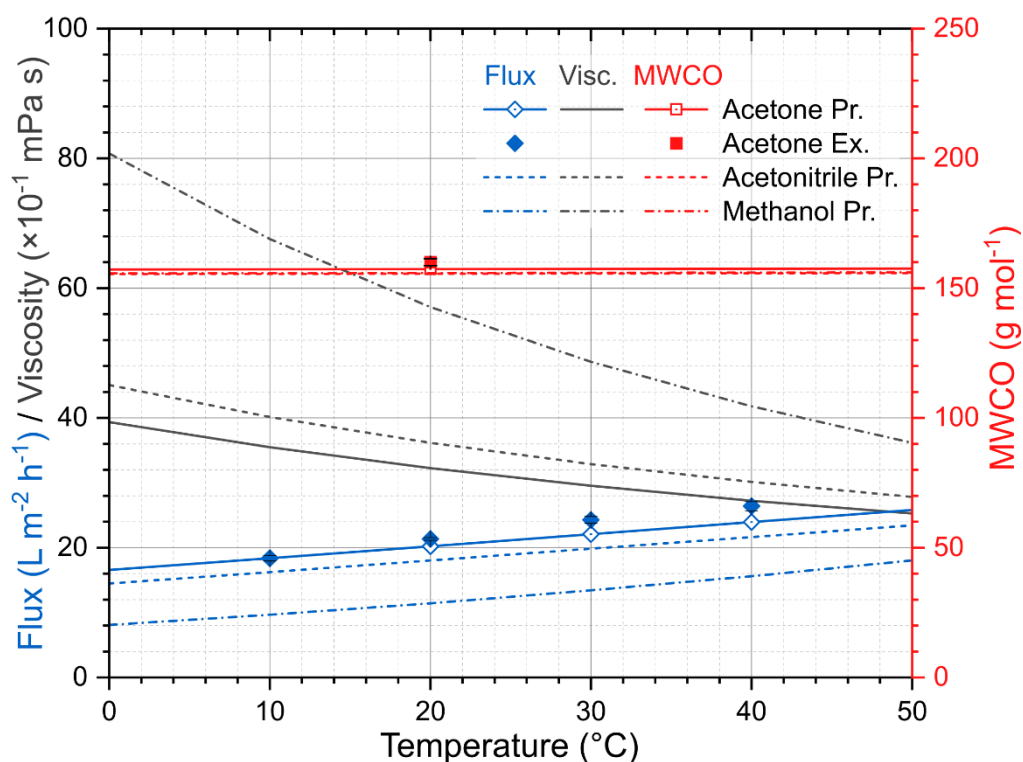


Fig. S66. Predicted (Pr.) and experimental (Ex.) effect of temperature on the M66^P membrane performance in acetone, acetonitrile, and methanol. (Expanded version of Fig. 4f)

Table S19. Experimental flux (and permeance) after 24 h of OSN operation for the M66^P membranes at 20°C at various transmembrane pressures (TMP).

| TMP (bar) | Flux (L m ⁻² h ⁻¹) | Flux Std. Dev. (L m ⁻² h ⁻¹) | Permeance (L m ⁻² h ⁻¹ bar ⁻¹) | Permeance Std. Dev. (L m ⁻² h ⁻¹ bar ⁻¹) |
|-----------|---|---|--|--|
| 10 | 8.10 | 0.26 | 0.81 | 0.03 |
| 20 | 14.28 | 0.44 | 0.71 | 0.02 |
| 30 | 21.35 | 0.20 | 0.71 | 0.01 |
| 40 | 28.38 | 1.60 | 0.71 | 0.04 |

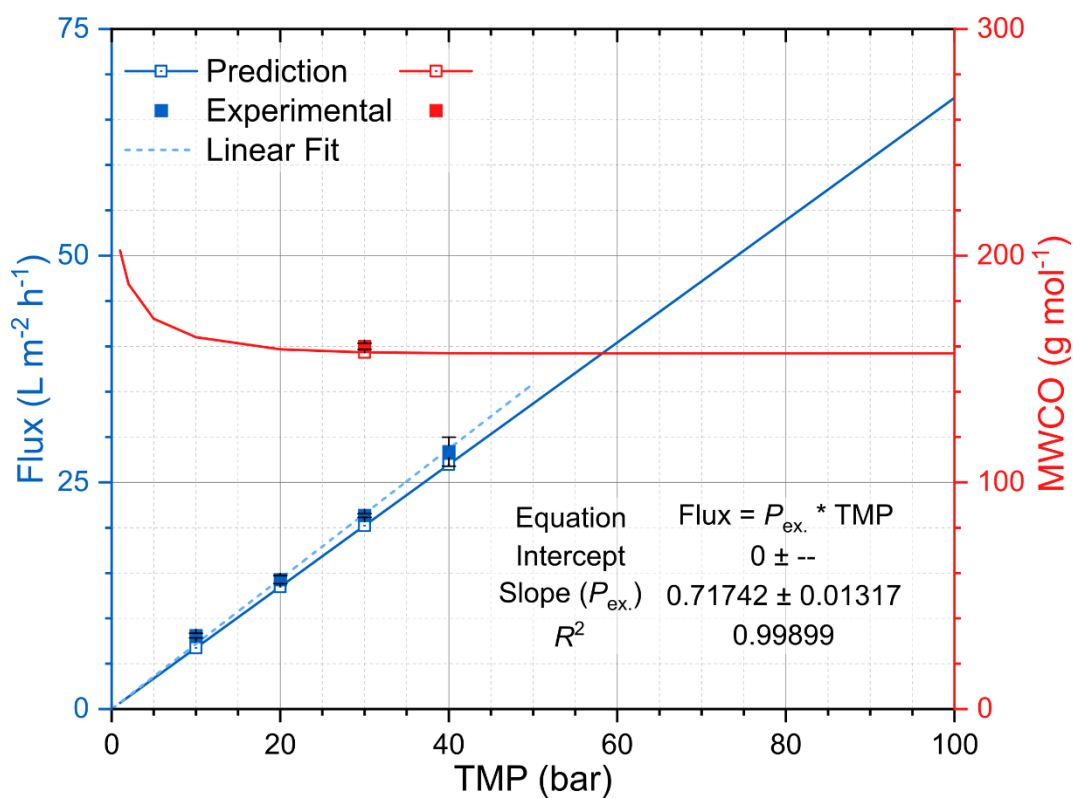


Fig. S67. Predicted (Pr.) and experimental (Ex.) effect of the transmembrane pressure (TMP) on the M66^P membrane performance. (Expanded version of Fig. 4g)

Table S20. Fitted log-normal distribution parameters of the M66^P, M67^P, and M68^P membranes.

| Membrane | Fitted log-normal distribution parameters | |
|------------------|---|------------------------------|
| | Mean pore diameter (nm) | Pore diameter std. dev. (nm) |
| M66 ^P | 0.911 | 0.055 |
| M67 ^P | 1.029 | 0.006 |
| M68 ^P | 1.270 | 0.005 |

23. Literature overview

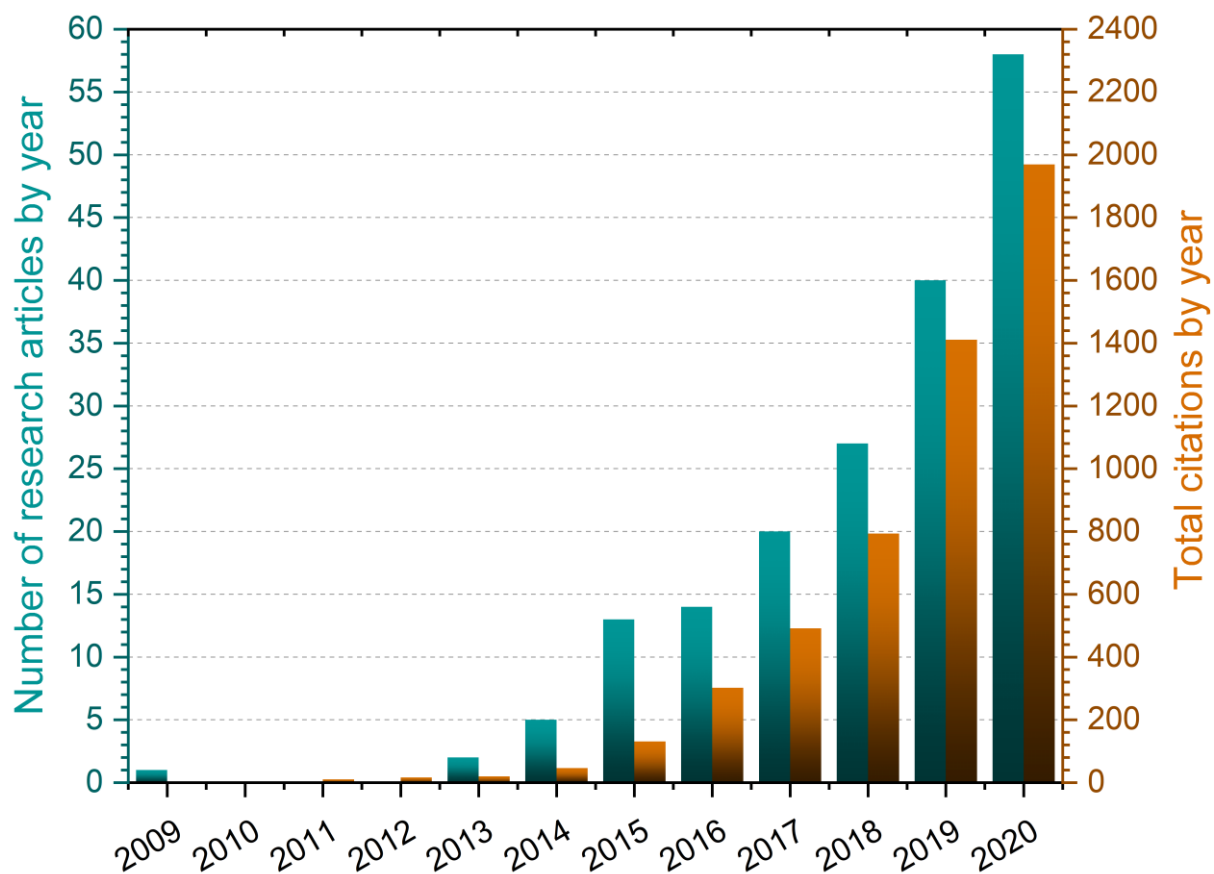


Fig. S68. Growing interest in MOF composite nanofiltration membranes. Number of research articles and total citations by year are obtained by searching the keywords “metal–organic framework, nanofiltration” on the Web of Science scientific search engine. The search was performed on January 19, 2021.

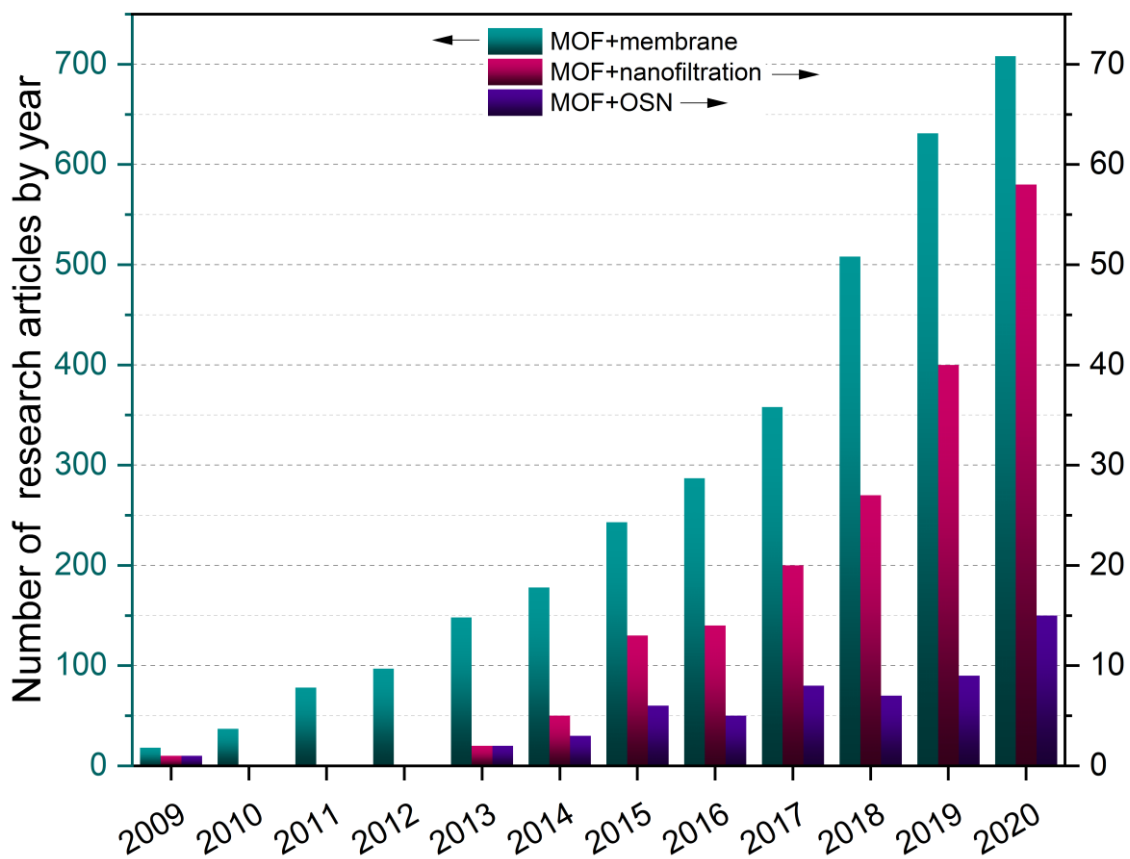


Fig. S69. Interest in MOF composite membranes in general and for nanofiltration and OSN in particular, as indicated by the number of research articles. The data were obtained by searching the keywords “metal–organic framework, membrane,” “metal–organic framework, nanofiltration,” and “metal–organic framework, organic solvent nanofiltration” on the Web of Science scientific search engine. The search was performed on January 19, 2021.

Table S21. Comparison of OSN membranes from UiO-type MOFs reported in the literature

| MOF | Polymer | Solvent | Permeance (L m ⁻² h ⁻¹ bar ⁻¹) | MWCO (g mol ⁻¹) | Ref. |
|--|---|------------|---|--------------------------------|-----------|
| UiO-66 | Polyamide thin-film composite | Methanol | 11 | <452 | 24 |
| UiO-66-N=CH-C ₉ H ₁₉ | Polyamide thin-film composite | Methanol | 2.9 | <269 | 25 |
| UiO-66-NH ₂ | Pristine MOF on carbon cloth | Methanol | 0.3 | <318 | 26 |
| UiO-66-NH ₂ | Matrimid | 2-Propanol | 1.2 | 828 | 27 |
| UiO-66-NH ₂ | MOF film grown on crosslinked Matrimid | Ethanol | 0.88 | <974 | 28 |
| UiO-66-sodium-polymethacrylate | Polypyrrole on hydrolysed poly(acrylnitrile) | Ethanol | 53.9 | <408 | 29 |
| UiO-66-NH ₂ | Polyester thin-film composite on polydopamine treated polyimide | Ethanol | 24.8 | 408 | 30 |
| UiO-66-NH ₂ | Polyamide thin-film composite | Methanol | 14 | <974 | 31 |
| UiO-66-NH ₂ | Crosslinked Matrimid | 2-Propanol | 1.28 | <442 | 32 |
| UiO-66-PNIPAM | | | 0.71 | 160 | |
| UiO-67-PNIPAM | Polybenzimidazole | Acetone | 0.83 | 211 | This work |
| UiO-68-PNIPAM | | | 2.07 | 290 | |

24. References

- 1 Z. Xu, G. Zhao, L. Ullah, M. Wang, A. Wang, Y. Zhang and S. Zhang, *RSC Adv.*, 2018, **8**, 10009–10016.
- 2 K. Vellingiri, A. Deep, K.-H. Kim, D. W. Boukhvalov, P. Kumar and Q. Yao, *Sensors Actuators B Chem.*, 2017, **241**, 938–948.
- 3 X. Zhang, Y. Zhang, T. Wang, Z. Fan and G. Zhang, *RSC Adv.*, 2019, **9**, 24802–24810.
- 4 Y. Cao, H. Zhang, F. Song, T. Huang, J. Ji, Q. Zhong, W. Chu and Q. Xu, *Mater.*, 2018, **11**.
- 5 A. Pankajakshan, M. Sinha, A. A. Ojha and S. Mandal, *ACS Omega*, 2018, **3**, 7832–7839.
- 6 L. Chen, H. Chen, R. Luque and Y. Li, *Chem. Sci.*, 2014, **5**, 3708–3714.
- 7 R. Thür, N. Van Velthoven, S. Sloodmaekers, J. Didden, R. Verbeke, S. Smolders, M. Dickmann, W. Egger, D. De Vos and I. F. J. Vankelecom, *J. Membr. Sci.*, 2019, **576**, 78–87.
- 8 C. R. Groom, I. J. Bruno, M. P. Lightfoot and S. C. Ward, *Acta Crystallogr. Sect. B*, 2016, **72**, 171–179.
- 9 H. Vogel and C. S. Marvel, *J. Polym. Sci.*, 1961, **50**, 511–539.
- 10 M. J. Frisch, G. W. Trucks, H. B. Schlegel, G. E. Scuseria, M. A. Robb, J. R. Cheeseman, G. Scalmani, V. Barone, G. A. Petersson, H. Nakatsuji, X. Li, M. Caricato, A. Marenich, J. Bloino, B. G. Janesko, R. Gomperts, B. Mennucci, H. P. Hratchian, J. V. Ort and D. J. Fox, 2016.
- 11 W. R. Bowen and J. S. Welfoot, *Chem. Eng. Sci.*, 2002, **57**, 1121–1137.
- 12 A. Gonzalez-Nelson, F.-X. Coudert and A. M. van der Veen, *Nanomaterials*, 2019, **9**.
- 13 D. I. Kolokolov, A. G. Stepanov, V. Guillerm, C. Serre, B. Frick and H. Jobic, *J. Phys. Chem. C*, 2012, **116**, 12131–12136.
- 14 P. Silva and A. G. Livingston, *J. Membr. Sci.*, 2006, **280**, 889–898.
- 15 J. L. C. Santos, P. de Beukelaar, I. F. J. Vankelecom, S. Velizarov and J. G. Crespo, *Sep. Purif. Technol.*, 2006, **50**, 122–131.
- 16 W. Schotte, *Chem. Eng. J.*, 1992, **48**, 167–172.
- 17 C. R. Wilke and P. Chang, *AIChE J.*, 1955, **1**, 264–270.
- 18 K. Miyabe and R. Isogai, *J. Chromatogr. A*, 2011, **1218**, 6639–6645.
- 19 W. R. Bowen, A. W. Mohammad and N. Hilal, *J. Membr. Sci.*, 1997, **126**, 91–105.
- 20 S. Bandini and D. Vezzani, *Chem. Eng. Sci.*, 2003, **58**, 3303–3326.
- 21 W. R. Bowen and J. S. Welfoot, *Chem. Eng. Sci.*, 2002, **57**, 1393–1407.
- 22 A. Bondi, *J. Phys. Chem.*, 1964, **68**, 441–451.
- 23 H. Vogel, *Phys. Z.*, 1921, **22**, 645–646.
- 24 L. Paseta, M. Navarro, J. Coronas and C. Téllez, *J. Ind. Eng. Chem.*, 2019, **77**, 344–354.

- 25 X. Guo, D. Liu, T. Han, H. Huang, Q. Yang and C. Zhong, *AIChE J.*, 2017, **63**, 1303–1312.
- 26 Y. Cai, D. Shi, G. Liu, Y. Ying, Y. Cheng, Y. Wang, D. Chen, J. Lu and D. Zhao, *J. Membr. Sci.*, 2020, **615**, 118551.
- 27 Z. F. Gao, Y. Feng, D. Ma and T.-S. Chung, *J. Membr. Sci.*, 2019, **574**, 124–135.
- 28 D. Ma, G. Han, Z. F. Gao and S. B. Chen, *ACS Appl. Mater. Interfaces*, 2019, **11**, 45290–45300.
- 29 J. H. Huang, X. Q. Cheng, Y. Zhang, K. Wang, H. Liang, P. Wang, J. Ma and L. Shao, *Cell Reports Phys. Sci.*, 2020, **1**, 100034.
- 30 Y. Zhang, X. Cheng, X. Jiang, J. J. Urban, C. H. Lau, S. Liu and L. Shao, *Mater. Today*, 2020, **36**, 40–47.
- 31 X. Cheng, X. Jiang, Y. Zhang, C. H. Lau, Z. Xie, D. Ng, S. J. D. Smith, M. R. Hill and L. Shao, *ACS Appl. Mater. Interfaces*, 2017, **9**, 38877–38886.
- 32 Z. F. Gao, A. Naderi, W. Wei and T.-S. Chung, *J. Membr. Sci.*, 2020, **616**, 118582.